

INVESTIGATION ON THE  
MICROSTRUCTURE DEVELOPMENT AND  
CORROSION PERFORMANCE OF FRICTION  
STIR WELDED DISSIMILAR AZ31/AZ91  
MAGNESIUM ALLOYS



NURUL SHUHADA BINTI HAJI MOHAMED

اونيورسيتي مليسيا قهغ

UNIVERSITI MALAYSIA PAHANG

MASTER OF SCIENCE

UNIVERSITI MALAYSIA PAHANG

UNIVERSITI MALAYSIA PAHANG

**DECLARATION OF THESIS AND COPYRIGHT**

Author's Full Name : NURUL SHUHADA BINTI HJ. MOHAMED

Date of Birth : 26 SEPTEMBER 1993

Title : INVESTIGATION ON THE MICROSTRUCTURE  
DEVELOPMENT AND CORROSION PERFORMANCE OF  
FRICION STIR WELDED DISSIMILAR AZ31/AZ91  
MAGNESIUM ALLOYS

Academic Session : SEMESTER I 2020 / 2021

I declare that this thesis is classified as:

- CONFIDENTIAL (Contains confidential information under the Official Secret Act 1997)\*
- RESTRICTED (Contains restricted information as specified by the organization where research was done)\*
- OPEN ACCESS I agree that my thesis to be published as online open access (Full Text)

I acknowledge that Universiti Malaysia Pahang reserves the following rights:

1. The Thesis is the Property of Universiti Malaysia Pahang
2. The Library of Universiti Malaysia Pahang has the right to make copies of the thesis for the purpose of research only.
3. The Library has the right to make copies of the thesis for academic exchange.

Certified by:

\_\_\_\_\_  
(Student's Signature)

\_\_\_\_\_  
(Supervisor's Signature)

930926-02-5254

Ts .Dr. Juliawati Binti Alias

\_\_\_\_\_  
New IC/Passport Number

\_\_\_\_\_  
Name of Supervisor

Date:

Date:

NOTE : \* If the thesis is CONFIDENTIAL or RESTRICTED, please attach a thesis declaration letter.

## SUPERVISOR'S DECLARATION

We hereby declare that We have checked this thesis and in our opinion, this thesis is adequate in terms of scope and quality for the award of the degree Master of Science.

---

(Supervisor's Signature)

Full Name : TS. DR. JULIAWATI BINTI ALIAS

Position : SENIOR LECTURER

Date :

---

(Co-supervisor's Signature)

Full Name : PROFESSOR DR. MAHADZIR BIN ISHAK

Position : Dean, Faculty of Mechanical & Automotive Engineering Technology

Date :

## STUDENT'S DECLARATION

I hereby declare that the work in this thesis is based on my original work except for quotations and citations which have been duly acknowledged. I also declare that it has not been previously or concurrently submitted for any other degree at Universiti Malaysia Pahang or any other institutions.

---

(Student's Signature)

Full Name : NURUL SHUHADA BINTI HAJI MOHAMED

ID Number : MMM17009

Date :

UMP

اونيورسيتي ملايسيا قهغ

UNIVERSITI MALAYSIA PAHANG

INVESTIGATION ON THE MICROSTRUCTURE DEVELOPMENT AND  
CORROSION PERFORMANCE OF FRICTION STIR WELDED DISSIMILAR  
AZ31/AZ91 MAGNESIUM ALLOYS

The logo of Universiti Malaysia Pahang (UMP) is a shield-shaped emblem. It features a central white diamond with a yellow diamond inside it, surrounded by a blue and green circular swirl. The shield is divided into four quadrants: top-left is teal, top-right is light blue, bottom-left is light blue, and bottom-right is teal. The letters 'UMP' are written in white across the bottom of the shield.

NURUL SHUHADA BINTI HAJI MOHAMED

Thesis submitted in fulfillment of the requirements  
for the award of the degree of  
Master of Science

اونيورسيتي مليسيا قهغ

UNIVERSITI MALAYSIA PAHANG

College of Engineering

UNIVERSITI MALAYSIA PAHANG

DECEMBER 2020

## ACKNOWLEDGEMENTS

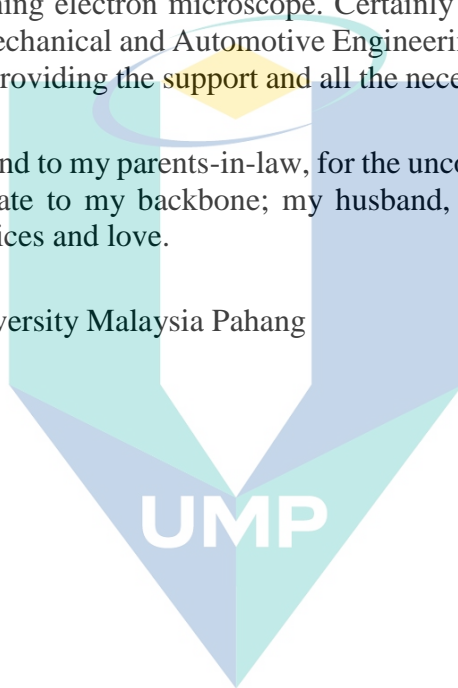
I would like to express my deepest gratitude to my supervisor, Dr. Juliawati Bt Alias who has guided and advised me throughout my research. With this kind guidance, support, patient and constant encouragement I have completed my research successfully.

I am thankful to Professor Dr. Mahadzir Bin Ishak@Muhamad as the great co-supervisor for his precious time, ideas, and knowledge during all phases of the research work.

A special thanks to the University Malaysia Pahang central lab for all the help and knowledge with scanning electron microscope. Certainly not to forget the Engineering College, Faculty of Mechanical and Automotive Engineering Technology and University Malaysia Pahang for providing the support and all the necessary equipment in this study.

Thanks to my family and to my parents-in-law, for the unconditional support all the time. I would like to dedicate to my backbone; my husband, Ibrahim Soaid for his strong encouragement, sacrifices and love.

Finally, thanks to University Malaysia Pahang



اونيورسيتي ملايسيا قهغ

UNIVERSITI MALAYSIA PAHANG

## ABSTRAK

Magnesium (Mg) dan aloinya adalah aloi yang menarik untuk aplikasi dalam industri automotif dan peranti elektronik kerana cirinya yang ringan. Aloinya Mg berpotensi sebagai aloi yang menyumbang kepada bahan mesra alam kerana pengurangan pelepasan gas karbon dioksida, ( $\text{CO}_2$ ) melalui penggunaan bahan ringan. Kimpalan pengadukan geseran (FSW) adalah kaedah penyambungan keadaan pepejal dapat menghasilkan penyempurnaan struktur mikro yang berkesan untuk kepingan nipis Mg. Semasa proses FSW, bahan melembut tanpa lebur, dan dengan mengekalkan suhu yang rendah, FSW dapat menghasilkan penyambungan yang berkualiti dengan tegasan baki yang rendah. Parameter FSW seperti kelajuan putaran alat dan kelajuan kimpalan memberi kesan yang bererti terhadap corak aliran bahan dan agihan suhu, sehingga mempengaruhi pengembangan struktur mikro bahan. Kadar degradasi atau kemusnahan aloi Mg yang cepat dalam kebanyakan persekitaran telah mengehadkan penggunaan aloi kerana kedudukan dalam daya elektromotif (EMF) dan rangkaian galvanik air laut. Mg dalam aplikasi automotif. Tujuan kajian ini adalah untuk mengkaji perkembangan struktur mikro aloi Mg yang dikimpal dengan kaedah FSW, dengan menonjolkan kesan kelajuan alat putaran pada struktur mikro dan untuk menilai prestasi karatan FSW Mg dengan menghubungkan perkembangan struktur mikro. Satu penyambungan aloi AZ31 dan AZ91 telah berjaya dikimpal oleh kaedah FSW dan penyambungan tanpa kecacatan berserta penghabluran semula struktur ira telah dicapai. Kelajuan alat putaran dan kelajuan kimpalan diubah semasa FSW dan struktur mikro telah dicirikan menggunakan mikroskop optik (OM) dan mikroskop pengimbasan elektron (SEM). Sifat karatan bagi setiap sampel dinilai menggunakan ujian evolusi hidrogen dan pengukuran elektrokimia melalui ujian keketuban dinamik upaya. Setiap kawasan yang dikimpal iaitu zon yang terjejas haba (HAZ), zon terjejas termomekanik (TMAZ), zon aduk (SZ) dan logam asas (BM) yang dibentuk oleh proses kimpalan menunjukkan penghabluran semula struktur ira dengan variasi saiz ira. Berdasarkan pemerhatian, struktur ira bimodal yang homogen berlaku dikebanyakan kawasan dan SZ menunjukkan kawasan dengan struktur ira yang paling halus. Peningkatan kelajuan alat putaran daripada 800 rpm sehingga 1,000 dan 1,200 rpm, tidak menunjukkan peningkatan saiz ira yang menonjol. Nilai kekerasan Vickers (HV) di SZ adalah 70 hingga 100 HV, disebabkan oleh struktur ira yang lebih kecil/halus terhasil daripada FSW, berbanding kawasan lain. Pengurangan kelajuan alat putaran daripada 1,200 kepada 800 rpm menyumbang kepada ketahanan rintangan karatan semasa ujian evolusi hydrogen ( $\text{H}_2$ ) di dalam 3.5 wt.% larutan natrium klorida (NaCl). Aloinya Mg yang dikimpal menunjukkan nilai upaya litar terbuka (OCP) dalam julat -1.624 V hingga -1.58 V. Lengkungan keketuban dinamik upaya menunjukkan ketahanan karatan meningkat dengan kelajuan kimpalan dan ia dibuktikan dengan nilai ketumpatan arus ( $i_{\text{corr}}$ ) yang rendah. Kesimpulannya, penghasilan ira yang homogen, saiz ira yang halus dan kehadiran butiran antara logam aluminium-mangan Al-Mn, boleh menyebabkan perubahan ketara kepada setiap kadar karatan dan kelakuan elektrokimia yang diubah, dan seterusnya menyumbang kepada nilai prestasi karatan keseluruhan sampel Mg yang dikimpal. Kajian ini disarankan sebagai penyelesaian kaedah penyambungan yang betul dan kadar karatan pada aloi Mg yang tidak sama.

## ABSTRACT

Magnesium (Mg) and its alloys are attractive alloys for automotive industries and electronic devices due to their lightweight properties. Based on the potential of Mg alloys as parts and components for weight reduction, it could contribute to eco-friendly materials due to the reduction of carbon dioxide (CO<sub>2</sub>) emission by the usage of the lightweight materials. Friction stir welding (FSW) is a solid-state joining method that can result in an effective microstructure refinement useful for thin Mg sheets. During FSW, the material is softened without melting and by maintaining low temperature, good quality joints can be produced with significant low residual stresses. The parameters of FSW, such as tool rotational speed and welding speed exert a significant effect on the material flow pattern and temperature distribution, thereby influencing the microstructural development of a material. The rapid degradation rate of Mg alloys in most environments has seriously limited their growth in automotive applications due to the position in the electromotive force (EMF) and galvanic series in seawater. The aims of this study are to investigate the microstructure development of friction stir welded Mg alloys by highlighting the effect of various tool rotational speeds on the microstructure of Mg alloys and also to evaluate the corrosion performance of friction stir welded Mg alloys by correlating to the microstructure development. The joining of dissimilar AZ31 and AZ91 Mg alloys was successfully conducted by FSW and defect-free joints with recrystallized grain structure were achieved. Tool rotational speed and welding speed were varied during FSW, and the microstructures of joint samples were characterized by optical microscopy (OM) and scanning electron microscopy (SEM). The corrosion behaviour of each sample was evaluated by hydrogen evolution test and electrochemical measurement by potentiodynamic polarization test. Each region of the welded sample, namely the heat-affected zone (HAZ), the thermomechanical heat-affected zone (TMAZ), the stir zone (SZ), and the base metal (BM) formed by the welding process represented a clear grain size variation. Based on the observation, homogeneous grain structure occurred at most of the regions, and the SZ was determined as the region with the most grain refinement compared to other regions. Increasing the tool rotational speed from 800 to 1,000 and 1,200 rpm showed no significant changes on grain size. The Vickers hardness values at the SZ are 70 to 100 HV due to recrystallized small grain structure produced by FSW. The reduction of rotational speed from 1,200 to 800 rpm contributed to the variation of corrosion resistance during hydrogen evolution test in 3.5 wt. % of sodium chloride (NaCl) solution. The welded Mg alloys exhibited open circuit potential (OCP) values in the range of -1.624 to -1.58 V. The potentiodynamic polarization curve indicated the increase of corrosion rate with the decrease of welding speed from 1,200 to 800 rpm as evidenced by the current density ( $i_{\text{corr}}$ ) values. In conclusion, by considering the homogeneous grain structure, grain refinement, and presence of aluminum-manganese (Al-Mn) intermetallic, the corrosion rate and electrochemical behavior changed in different regions, which contributed to the overall corrosion performance of the welded Mg samples. This study is recommended as a solution on proper joining technique and corrosion performance of dissimilar Mg alloys.



## TABLE OF CONTENT

**DECLARATION**

**TITLE PAGE**

**ACKNOWLEDGEMENTS** **ii**

**ABSTRAK** **iii**

**ABSTRACT** **iv**

**TABLE OF CONTENT** **v**

**LIST OF TABLES** **ix**

**LIST OF FIGURES** **x**

**LIST OF SYMBOLS** **xiii**

**LIST OF ABBREVIATIONS** **xv**

**CHAPTER 1 INTRODUCTION** **1**

1.1 Research Background 1

1.2 Problem Statement 4

1.3 Research Objectives 5

1.4 Research Scopes 5

**CHAPTER 2 LITERATURE REVIEW** **7**

2.1 Introduction 7

2.2 Structure and Properties of Magnesium Alloys 7

2.3 Magnesium Alloy 8

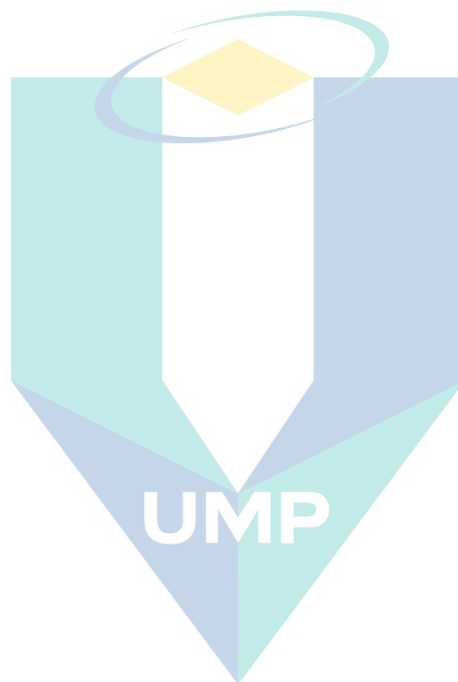
2.4 Main Constituent Phase in AZ31 and AZ91 Mg Alloys 10

2.5 Friction Stir Welding 11

2.6	General Microstructural Evolution in Mg Alloys during FSW	13
2.7	Deformation of Mg	15
2.7.1	Twinning	15
2.7.2	Dynamic Recrystallization	17
2.8	Corrosion of Mg alloy	18
2.9	Microstructural Effect on Corrosion	19
2.10	Micro-galvanic Effect of Alloying Elements	19
2.11	Common Type of Corrosion in Mg Alloys	21
2.11.1	Pitting Corrosion in Mg Alloys	21
2.11.2	Filiform-like Corrosion	23
2.12	Electrochemical Measurement	25
2.12.1	Weight Loss and Hydrogen Evolution Test	27
2.13	Summary	30
<b>CHAPTER 3 METHODOLOGY</b>		<b>31</b>
3.1	Introduction	31
3.2	Research Flow	31
3.3	Material Composition	32
3.3.1	Sample Preparation for Experiment	33
3.4	Friction Stir Welding (FSW) Process	34
3.4.1	Experiment Setup	35
3.5	Microstructure Characterization	36
3.5.1	Sample Preparation	36
3.5.2	Characterization Using Optical and Scanning Electron Microscope (SEM)	36
3.6	Hardness Test	37

3.7	Corrosion Test	38
3.7.1	Hydrogen Evolution Test	38
3.7.2	Electrochemical Measurement by Potentiodynamic Polarization	41
3.8	Summary	43
<b>CHAPTER 4 RESULTS AND DISCUSSION</b>		<b>44</b>
4.1	Introduction	44
4.2	Microstructure Development of FSW AZ31/AZ91 Alloys	44
4.2.1	Microstructure of FSW Sample Using Variation Rotational Speed	47
4.2.1.1	Rotational Speed of 1,200 rpm	47
4.2.1.2	Rotational Speed of 1,000 rpm	49
4.2.1.3	Rotational Speed of 800 rpm	52
4.2.2	Intermetallic Particles Distribution	54
4.2.3	Microhardness	58
4.3	Corrosion Performance of Welded AZ31/AZ91 Alloys	60
4.3.1	Corrosion Behaviour During Hydrogen Evolution Measurement	60
4.3.2	Corrosion Morphology After Corrosion Product Removal	66
4.4	Electrochemical Characteristic of Welded AZ31/AZ91 Alloys	68
4.4.1	Open Circuit Potential (OCP)	69
4.4.2	Potentiodynamic Polarization	72
4.5	Summary	77
<b>CHAPTER 5 CONCLUSION AND RECOMMENDATION</b>		<b>78</b>
5.1	Introduction	78
5.2	Microstructure Development of FSW Mg Alloys	78
5.3	Corrosion Performance of Welded Mg Alloy	79

5.4	Electrochemical Characteristic of Welded Mg Alloy	79
5.5	Recommendation for Future Work	80
	<b>REFERENCES</b>	<b>81</b>
	<b>APPENDIX A PUBLICATIONS</b>	<b>88</b>
	<b>APPENDIX B CORROSION RATE</b>	<b>89</b>

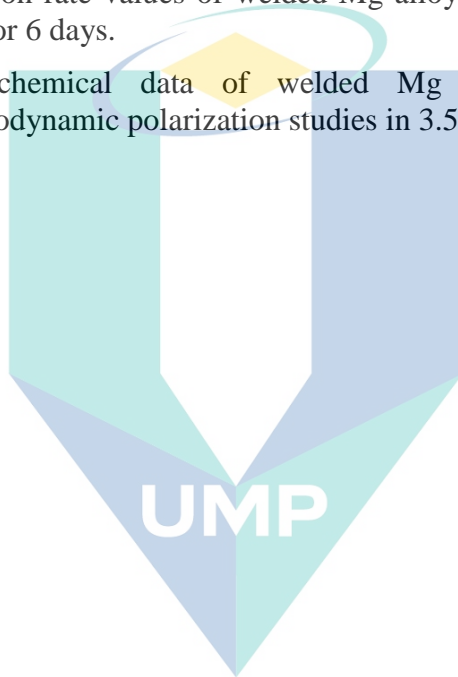


اونيورسيتي ملايسيا قهغ

UNIVERSITI MALAYSIA PAHANG

## LIST OF TABLES

Table 2.1	Nominal composition of AZ31 and AZ91 Mg alloys.	8
Table 2.2	Main constituent phases in AZ31 and AZ91.	11
Table 2.3	Advantages of friction stir welding.	12
Table 3.1	Elemental composition of Mg alloy (wt.%).	33
Table 3.2	Welding sample arrangement.	35
Table 3.3	Potentiodynamic polarization test parameter setup.	43
Table 4.1	Corrosion rate values of welded Mg alloys immersed in 3.5 wt.% NaCl for 6 days.	65
Table 4.2	Electrochemical data of welded Mg alloys obtained from potentiodynamic polarization studies in 3.5 wt.% NaCl solution.	76



اونيورسيتي مليسيا قهغ

UNIVERSITI MALAYSIA PAHANG

## LIST OF FIGURES

Figure 1.1	Weight reduction of automotive components.	2
Figure 1.2	U.S magnesium market size by application.	2
Figure 2.1	Hexagonal closed-packed (HCP) crystal structure of Mg.	8
Figure 2.2	Mg-Al binary phase diagram.	9
Figure 2.3	Mg-Zn binary phase diagram.	9
Figure 2.4	a) Microstructure of as-cast AZ31, b) microstructure of as-cast AZ91 Mg alloys.	10
Figure 2.5	Schematic illustration of the FSW process of Mg alloys.	12
Figure 2.6	Macrostructure cross section of friction stir welding showing the welded region.	14
Figure 2.7	AZ31B-H24 typical optical micrograph: (a) base metal (BM), (b) Heat affected zone (HAZ), (c) thermomechanical heat affected zone (TMAZ), (d) stir zone (SZ).	14
Figure 2.8	Microstructure of lenticular twins formed on the Mg alloy .	16
Figure 2.9	Electron backscatter diffraction (EBSD) maps of the stir zone (SZ).	17
Figure 2.10	Microstructure of the: (a) BM, (b) recrystallized grains after dynamic recrystallization occurred.	18
Figure 2.11	Microstructure of AZ80 Mg alloy.	20
Figure 2.12	SEM micrographs of corrosion morphology on the surfaces of different AZ91 samples: (a) as-cast sample, (b) FSPed sample, (c) magnified image of FSPed sample.	21
Figure 2.13	Schematic diagram of pitting corrosion in Mg immerse in NaCl solution.	22
Figure 2.14	Pitting corrosion occurred on the surface of AZ31.	22
Figure 2.15	Pitting corrosion occurred at AlMn particles.	23
Figure 2.16	Filiform-like corrosion of AZ91.	24
Figure 2.17	In-situ imaging of filiform corrosion of dissimilar AZ31/AZ91 FSW joint.	25
Figure 2.18	Polarization curves of AZ91D weld and its base materials in 3.5% NaCl solutions.	26
Figure 2.19	Polarization curve of the BM and FSW samples.	27
Figure 2.20	Corrosion rates of fine-grained (FG) and coarse-grained (CG) specimens convert from the (a) weight loss and (b) hydrogen evolution.	28
Figure 2.21	Mg dissolution of AZ91 samples, (a) Hydrogen evolution rate (b) weight loss rate after 1 week of immersion.	29

Figure 2.22	Corrosion rate of the specimens in different regions evaluated after 7 days of immersion in 3.5 wt.% NaCl solution.	29
Figure 3.1	Research work flow chart.	32
Figure 3.2	Schematic arrangement of welded sheet with cutting plan for microstructure, hardness, and corrosion samples.	33
Figure 3.3	FSW milling machine.	34
Figure 3.4	Backing and clamping plate.	34
Figure 3.5	Tool design and dimension.	35
Figure 3.6	SEM principle and its function	37
Figure 3.7	Schematic diagram of sample for hydrogen evolution test.	39
Figure 3.8	(a) Schematic diagram of hydrogen evolution test, (b) Experiment setup for hydrogen evolution test.	40
Figure 3.9	(a) Welded sample for electrochemical test (b) experiment setup for electrochemical test.	42
Figure 4.1	Weld surface morphology.	45
Figure 4.2	Microstructure of (BM); (a) AZ31, (b) AZ91 taken by optical microscopy.	46
Figure 4.3	Macrographs of FSW AZ31/AZ91 joint viewed at the cross section of sample 1,200 rotational speed.	47
Figure 4.4	Micrographs of FSW AZ31/AZ91 joint viewed at the cross section of sample 1,200 rpm x 80 mm/min. (a) HAZ of RS, (b) HAZ of AS, (c) SZ, (d) TMAZ of AS, (e) TMAZ of RS.	49
Figure 4.5	Macrograph of FSW AZ31/AZ91 joint viewed at the cross section at 1,000 rpm rotational speed.	50
Figure 4.6	Micrographs of FSW AZ31/AZ91 joint viewed at the cross section of sample 1,000 rpm x 80 mm/min. (a) HAZ of RS, (b) HAZ of AS, (c) SZ, (d) TMAZ of AS, (e) TMAZ of RS	51
Figure 4.7	Macrograph of FSW AZ31/AZ91 joint viewed at the cross section at 800 rpm rotational speed.	52
Figure 4.8	Micrographs of FSW AZ31/AZ91 joint viewed at the cross section of sample 800 rpm x 60 mm/min. (a) HAZ of RS, (b) HAZ of AS, (c) SZ, (d) TMAZ of RS, (e) TMAZ of AS.	53
Figure 4.9	SEM micrograph of SZ region with EDX mapping analysis on the $\alpha$ -Mg matrix and the particles.	55
Figure 4.10	EDX spectrum of SZ mapping.	55
Figure 4.11	SEM micrograph of HAZ region with EDX mapping analysis	56
Figure 4.12	EDX spectrum of HAZ mapping.	57
Figure 4.13	SEM micrograph of TMAZ region with EDX point analysis on the particles.	57
Figure 4.14	EDX point spectrum of the particle found at TMAZ.	57

Figure 4.15	Hardness distribution of welded Mg alloy using rotational speed of: (a) 1,200 rpm, (b) 1,000 rpm, and (c) 800 rpm.	59
Figure 4.16	Hydrogen evolution rate of welded Mg alloy over 6 days immersion at 1,200 rpm rotational speed.	60
Figure 4.17	Hydrogen evolution rate of welded Mg alloy over 6 days immersion at 1,000 rpm rotational speed.	61
Figure 4.18	Hydrogen evolution rate of welded Mg alloy over 6 days immersion at 800 rpm rotational speed.	62
Figure 4.19	In-situ images of welded samples immersed in 3.5 wt.% NaCl during hydrogen evolution test for over 6 days.	64
Figure 4.20	Optical image of corroded sample during hydrogen evolution test.	66
Figure 4.21	SEM micrograph of corroded samples after corrosion product cleaning on of AZ31.	67
Figure 4.22	SEM micrograph of corroded samples after corrosion product cleaning on of AZ91.	67
Figure 4.23	SEM micrograph of corroded samples after corrosion product cleaning at welded zone.	68
Figure 4.24	SEM micrograph of sample showing crack after corrosion product cleaned immersed for hydrogen evolution experiment.	68
Figure 4.25	Open circuit potential (OCP) vs time curves for 800 rpm rotational speed.	70
Figure 4.26	Optical image of welded alloy during OCP for 5 minute.	70
Figure 4.27	Open circuit potential (OCP) vs time curves for 1,000 rpm rotational speed.	71
Figure 4.28	Open circuit potential (OCP) vs time curves for 1,200 rpm rotational speed.	72
Figure 4.29	Potentiodynamic polarization curve of the welded alloys using 1,200 rotational speed with the surface appearance during anodic polarization.	73
Figure 4.30	Potentiodynamic polarization curve of the welded alloys under 1,000 rpm.	74
Figure 4.31	Potentiodynamic polarization curve of the welded alloys using rotational speed 800 rpm.	75



## LIST OF SYMBOLS

%	Percentage
°C	Celsius
μm	Micrometer
<i>a</i>	Short edge length
A	Area
Ag	Silver
Al	Aluminum
Au	Gold
AZ	Aluminum Zinc
Br <sup>-</sup>	Bromide Ion
C	Long edge length
Cl <sup>-</sup>	Chloride Ion
cm <sup>3</sup>	Centimeter Cubic
Co	Cobalt
CO <sub>2</sub>	Carbon Dioxide
CR	Penetration Rate
CrO <sub>3</sub>	Chromium trioxide
Cu	Copper
E <sub>corr</sub>	Corrosion Potential
EW	Equivalent Weight
F	Force
Fe	Iron
g	Gram
h	Hour
H13	Chromium Hot Work
H <sub>2</sub>	Hydrogen gas
H <sub>2</sub> O	Water
HV	Vickers Hardness
I <sup>-</sup>	Iodide ion
I <sub>corr</sub>	Corrosion Current Density
K	Constant Value

اونیورسیتی ملیسیا فہم  
UNIVERSITI MALAYSIA PAHANG

KCl	Potassium Chloride
kg	Kilogram
kN	Kilo Newton
mg	Milligram
Mg	Magnesium
Mg(OH) <sub>2</sub>	Magnesium Hydroxide
Mg <sup>2+</sup>	Magnesium ion
MgCl <sub>2</sub>	Magnesium Chloride
min	Minute
ml	Milliliter
mm	Millimeter
mm <sup>2</sup>	Millimeter square
Mn	Manganese
Mol	Molarity
MP	Mega Pixel
mV/s	Mili Volt per second
NaCl	Sodium Chloride
Ni	Nickel
O <sub>2</sub>	Oxygen gas
OH	Hydroxyl
OH <sup>-</sup>	Hydroxyl ion
Pb	Lead
pH	Power of hydrogen
P <sub>H</sub>	Hydrogen Evolution Rate
P <sub>w</sub>	Weight Loss
s	Second
SiC	Silicon carbide
Sn	Tin
V	Voltage
Wt	Weight
y	Year
Zn	Zinc
$\rho$	Material Density



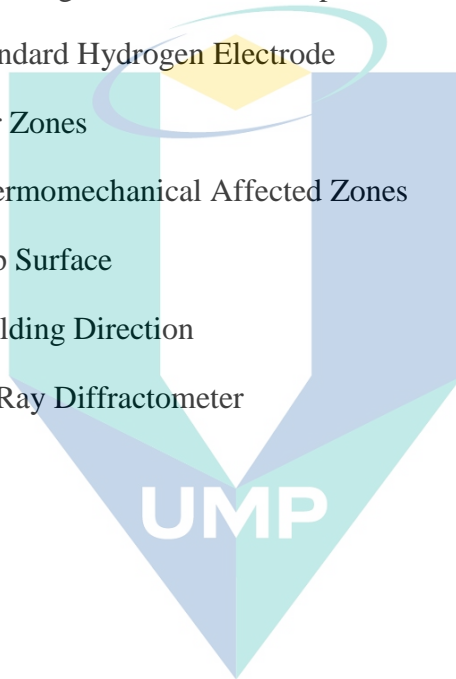
اونیورسیتی ملیسیا فہم

UNIVERSITI MALAYSIA PAHANG

## LIST OF ABBREVIATIONS

AM	Aluminum Manganese
As	Advancing Side
ASTM	American Society for Testing and Materials
AZ	Aluminum Zinc
BCC	Body Centered Cubic
BM	Base metal
CG	Coarse Grain
Cs	Cross-section Surface
DRX	Dynamic Recrystallization
EBSD	Electron Backscatter Diffraction
EDX	Energy Dispersive X-Ray Spectroscopy
EMF	Electromotive Force
FG	Fine Grain
FSP	Friction Stir Process
FSW	Friction Stir Welding
HAZ	Heat Affected Zone
HCP	Hexagonal Closed Packed
IMC	Intermetallic Compound
IPF	Inverse Pool Figure
ND	Normal Direction
NDE	Negative Different Effect
NZ	Nugget Zone
OCP	Open Circuit Potential
OM	Optical Microscope

OPS	Oxide Particle Suspension
RD	Rolling Direction
RPM	Rotational Speed
Rs	Retreating Side
RSM	Response Surface Method
SCE	Saturated Calomel Electrode
SEM	Scanning Electron Microscope
SHE	Standard Hydrogen Electrode
SZ	Stir Zones
TMAZ	Thermomechanical Affected Zones
Ts	Top Surface
WD	Welding Direction
XRD	X-Ray Diffractometer



اونيورسيتي ملايسيا قهغ

UNIVERSITI MALAYSIA PAHANG

# CHAPTER 1

## INTRODUCTION

### 1.1 Research Background

Magnesium (Mg) and its alloys are the lightest structural and engineering metals, and also attractive alloys for automotive industries and electronic device applications. Due to their lightweight properties, the potential of Mg alloys as parts and components for weight reduction could contribute to the reduction of carbon dioxide (CO<sub>2</sub>) emission (Salih et al., 2019). Examples of automotive parts made from Mg alloys are seat frames, support frames, steering wheels, and engine bodies, as shown in Figure 1.1. With the density of 1.75 g/cm<sup>3</sup>, Mg alloys are beneficial to promote market size growth as analyzed in Figure 1.2 from 2016 to 2027. The desire for lightweight reduction has created the needs to develop materials that provide a good combination of strength and ductility, and simultaneously has good corrosion resistant. Automotive manufacturers such as Volkswagen used 22 kg of Mg in its Beetle model whereas Porsche manufactured their Mg engines in 1928 (Kulekci, 2015).

Based on previous research (Dhanapal et al., 2012; Ghali et al., 2013; Prasad et al., 2016; Zhao et al., 2019), the formability of Mg alloys seems to be high at high temperature, owing to their hexagonal close-packed (HCP) crystal structure. At the temperature more than 400 °C, non-basal slip dislocations are activated, especially the pyramidal and prismatic slips located at the chassis plane, thus making Mg alloys easily formable. Hot deformation at temperatures above 400 °C is extensively used to produce wrought Mg products, such as sheet metals or extruded bars and tubes. With the increasing demand of Mg alloys in automotive and aerospace sectors, together with the welding of Mg alloys that are still facing many challenges, the necessity of a reliable joining method remains vital to enhance Mg applications.

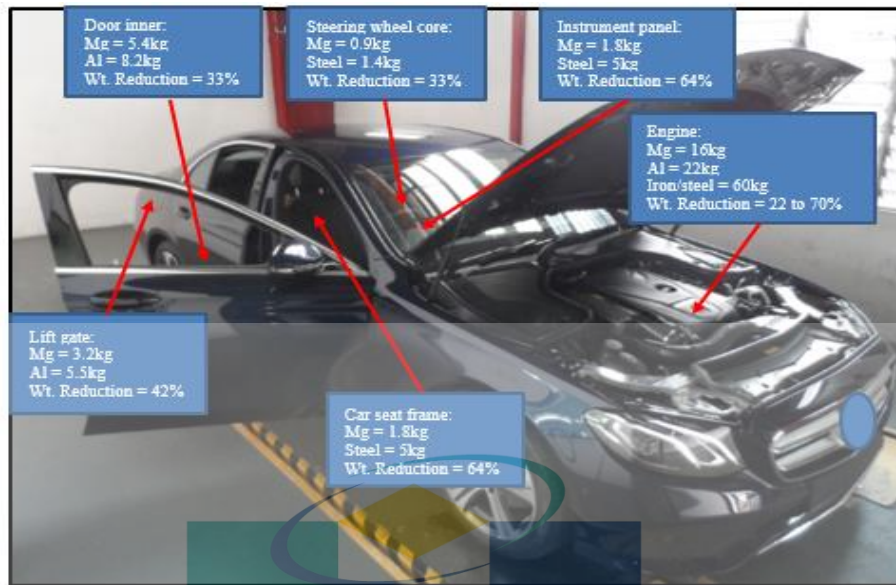


Figure 1.1 Weight reduction of automotive components.

Source: Kulekci, (2015)

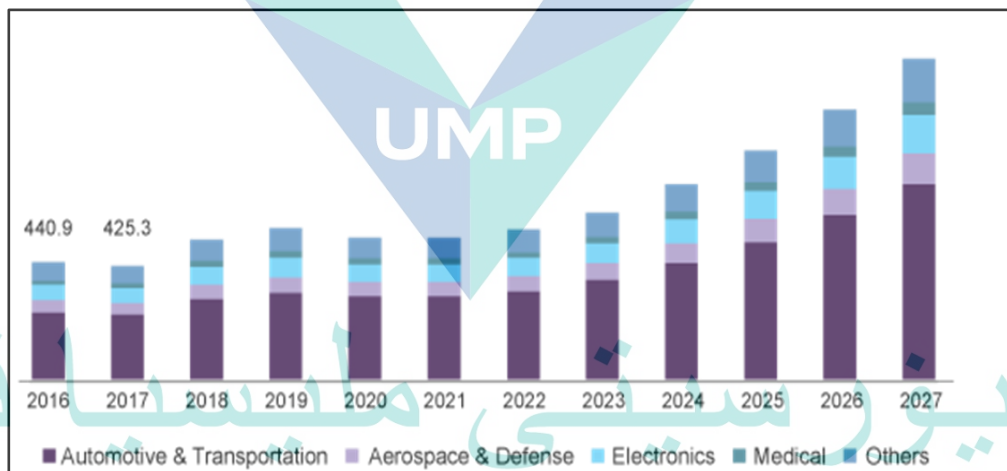


Figure 1.2 U.S magnesium market size by application.

Source: *Magnesium Alloys Market Size, Share & Trends Analysis Report By Application (Automotive & Transportation, Aerospace & Defense, Electronics), By Region (MEA, North America, APAC), And Segment Forecasts, (2020 - 2027), n.d.,(2020).*

Welding of Mg alloys is mainly applied in repairing structures due to the presence of many defects, such as oxide films of Mg, cracks, and cavities (Lehner et al., 1999; Thomas et al., 2016). Porosity, oxide layer, and brittle intermetallic compounds are easily formed when using conventional welding techniques to join Mg alloys due to the high

chemical activity by the heat input. Conventional welding techniques introduce large heat-affected zones (HAZ) (Mohammadi et al., 2015), porosity (Mishra & Ma, 2005), evaporative loss of alloying elements, and high residual stresses (Pan et al., 2016). Friction stir welding (FSW) is one of the alternative joining techniques that could overcome the mentioned limitations. This approach is a solid-state joining process without melting the material that could create pore-free joints, avoid thermal gradients, and the microstructural changes are not complex compared to conventional joining methods (Mishra & Ma, 2005; Yuan et al., 2011).

Research in the FSW of Mg alloys has created effective microstructural homogenization and refinement as a result of the recovery and recrystallization phenomena (James, 2012; Woo et al., 2006). During welding with some deformation occurrence, slip dislocation increases and some precipitates might be dissolved, and this encourages a homogeneous grain structure (Tuz et al., 2017; Woo et al., 2008). The FSW technique involves simple material movement and almost no or less plastic deformation. Welding parameters such as tool rotational speed and welding speed exert significant effects on the material flow pattern and temperature distribution, which consequently affect the microstructural evolution of materials.

On the other hand, Mg alloys have a low standard electrode potential that can be actively degraded in an aggressive environment (Wang et al., 2016). The degradation of Mg alloys could generate excessive hydrogen ( $H_2$ ) gas evolution around a weak or anodic point, resulting in localized attack and formation of non-protective corrosion product due to Mg hydroxide ( $Mg(OH)_2$ ) enrichment surrounding the surface (Zeng et al., 2009). The resistance to moisture and corrosive species in Mg alloys is evidenced by the formation of protective Mg oxide passive film on the surface (Ghali et al., 2013; Taltavull et al., 2014), and also the presence of cathodic second-phase particles that could act as a corrosion barrier (Gao et al., 2017). In this case, the type of alloying addition and second-phase particle distribution play significant roles in affecting corrosion resistance.

The variation of microstructure development within the weldment region, the base metal, and the affected region is expected to induce susceptibility to localized corrosion due to the electrochemical response of Mg alloys in the environment during service. Thus, the combination effect of excessive  $H_2$  gas evolution, non-protective corrosion product formation, and microstructure tendency could significantly contribute to the corrosion

performance of welded Mg alloys. At the current state, the research focusing on the effect of FSW on the corrosion behavior of Mg alloys needs further justification within this study. Thus, in this study, dissimilar AZ31 and AZ91 Mg alloys are joined by FSW with varied tool rotational speed and welding speed. AZ91 Mg alloy contribute to 90 % share as the commercial Mg casting used in automobiles (Jaiganesh et al., 2017), while AZ31 reveals good combination of mechanical properties and extrude-ability among the others wrought Mg alloys (Luo & Sachdev, 2016). The microstructure development of the welded samples was characterized using optical microscopy (OM) and scanning electron microscopy (SEM). The compositional analysis of intermetallic presence was further performed by energy dispersive X-ray spectroscopy (EDX). Hardness measurement using Vickers microhardness test was carried out to examine the hardness profile of each region. Next, the evaluation of corrosion performance was performed based on H<sub>2</sub> evolution test and electrochemical measurement by conducting potentiodynamic polarization test. It is expected that the possible joining process has better material modification and hence, good corrosion performance can be suggested.

## 1.2 Problem Statement

Research of lightweight materials has increased vastly, especially those focusing on the applicability of Mg alloys as structural materials and automotive components. Mg alloys could save a considerable amount of vehicle mass, thus promoting energy-efficient transportation. By applying Mg alloys for vehicle weight reduction, the fuel economy could be improved and CO<sub>2</sub> emission could be reduced. Mg alloys can be produced using conventional fusion welding but this method causes a large coefficient of expansion of the alloys and significant changes in microstructure resulting from melting and solidification process. The approach also leads to large deformation/distortion of the welded metals. The FSW method is an alternative approach to these weaknesses as metals can be joined by applying a wide variety of process parameters without the need for high heat input.

Despite having some good properties, the limitation of Mg alloys in many applications is due to their rapid degradation rate in most environments, especially in chloride solutions. During welding, the heat input from the process can lead to microstructure variation, which can also affect corrosion performance. Thus, a careful characterization based on the FSW parameters of tool rotational speed and welding speed



can be used to justify the effect of FSW on the microstructure development and corrosion performance. Therefore, the present study concerned the effect of FSW on the microstructure development and corrosion performance of dissimilar AZ31/AZ91 Mg alloys.

### 1.3 Research Objectives

The main objective of this research are:

- a) To investigate the microstructure development of dissimilar friction stir welded AZ31/AZ91 Mg alloys.
- b) To evaluate the corrosion performance of friction stir welded Mg alloys by correlating to the microstructure development.

### 1.4 Research Scopes

The scopes of this research include:

- a) The materials used for dissimilar joining are AZ31 and AZ91 Mg alloy sheets with 3 mm thickness.
- b) The FSW of Mg alloys was conducted using a vertical conventional milling machine with a fixed shoulder diameter and a pin diameter.
- c) Two main FSW parameters involved are tool rotational speed and welding speed.
- d) Microstructure characterization was conducted using OM and SEM. Meanwhile, compositional analysis of intermetallic particles was determined using EDX.
- e) Corrosion evaluation was conducted using H<sub>2</sub> evolution test and electrochemical test by potentiodynamic polarization measurement.

## 1.5 Organization of the Thesis

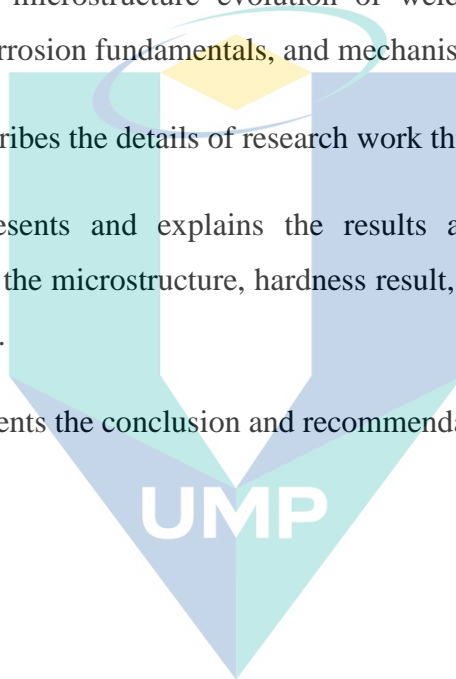
Chapter 1 explains the introduction of Mg alloys used in automotive applications for vehicle weight reduction. The chapter also includes the background of the study, problem statements, research objectives, and research scopes.

Chapter 2 discusses literature findings on Mg alloys and systems, FSW approach, previous research on microstructure evolution of welded Mg alloys, properties of materials involved, corrosion fundamentals, and mechanisms.

Chapter 3 describes the details of research work throughout this study.

Chapter 4 presents and explains the results and data collected from the experiment, including the microstructure, hardness result, and corrosion evaluation data of the welded samples.

Chapter 5 presents the conclusion and recommendations for future work.



اونيورسيتي مليسيا قهغ

UNIVERSITI MALAYSIA PAHANG

## CHAPTER 2

### LITERATURE REVIEW

#### 2.1 Introduction

Research on welded magnesium (Mg) and its alloys has been extensively conducted over the past few years. The development toward massive applications of Mg alloys is the main focus in this chapter, mainly due to the significant contribution in cost reduction, fuel economy, and eco-friendly material that increases the demand in automotive industry.

#### 2.2 Structure and Properties of Magnesium Alloys

To date, the lightest structural and engineering metals are dominated by Mg alloys and Mg-based composites, which offer advantages in automotive and aerospace industries (Kumar et al., 2015). To obtain good mechanical properties of lightweight metallic alloys, pure Mg, which is an alkaline earth metal, is generally alloyed with other elements, such as aluminum (Al), zinc (Zn), and manganese (Mn), as this alkaline earth metal alone does not have the required strength and stiffness for many engineering applications (Afrin et al., 2007). Mg has a hexagonal close-packed (HCP) structure as shown in Figure 2.1, with planes and directions in crystal lattice parameters of  $a = 0.320$  nm,  $c = 0.520$  nm, and  $c/a$  ratio = 1:624. Mg alloy with the designation of AZ31 is an alloy with a nominal composition of 3 wt. % of Al and 1 wt. % of Zn. The nominal compositions of AZ31 and AZ91 alloys are outlined in Table 2.1, in accordance to standard specification for magnesium alloys sheet and plate (ASTM B90/B90M-13, 2013).

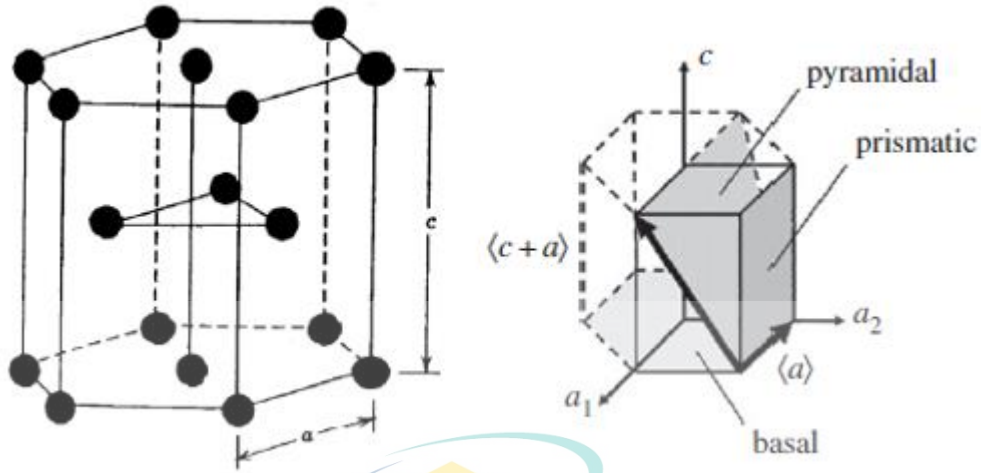


Figure 2.1 Hexagonal closed-packed (HCP) crystal structure of Mg.

Source: Hazell et al., (2014)

Table 2.1 Nominal composition of AZ31 and AZ91 Mg alloys.

Alloy	Composition (wt. %)			
	Al	Zn	Mn	Mg
AZ31	3	1	0.2	95.8
AZ91	8.67	0.85	0.03	90.45

Source: ASTM B90/B90M-13, (2013)

### 2.3 Magnesium Alloy

Magnesium is one of the lightest and most important nonferrous metals on earth, and used as structural material. The applications of Mg alloys for engineering and structural metals are still limited. Additional alloying element is helpful to maximize strength (Zhang, 2010), ductility (Myśliwiec & Sliwa, 2018), workability (Mansoor & Ghosh, 2012), and castability (Kumar & Kailas, 2008). The dominant alloying elements in AZ series are Al and Zn. In order to understand the phase formation theory of the alloys, the binary diagrams of Mg-Al (Figure 2.2) and Mg-Zn (Figure 2.3) are presented.

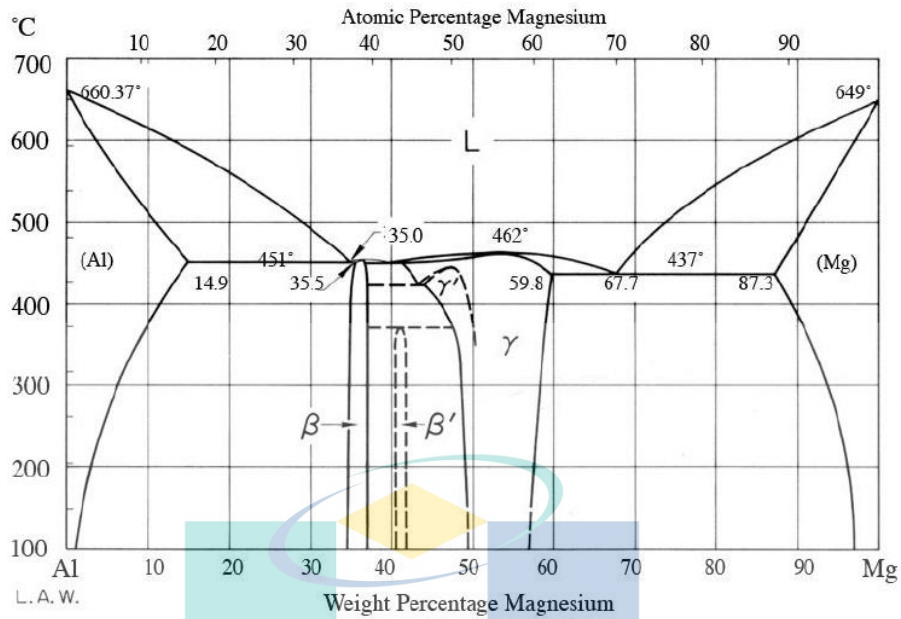


Figure 2.2 Mg-Al binary phase diagram.

Source: James, (2012)

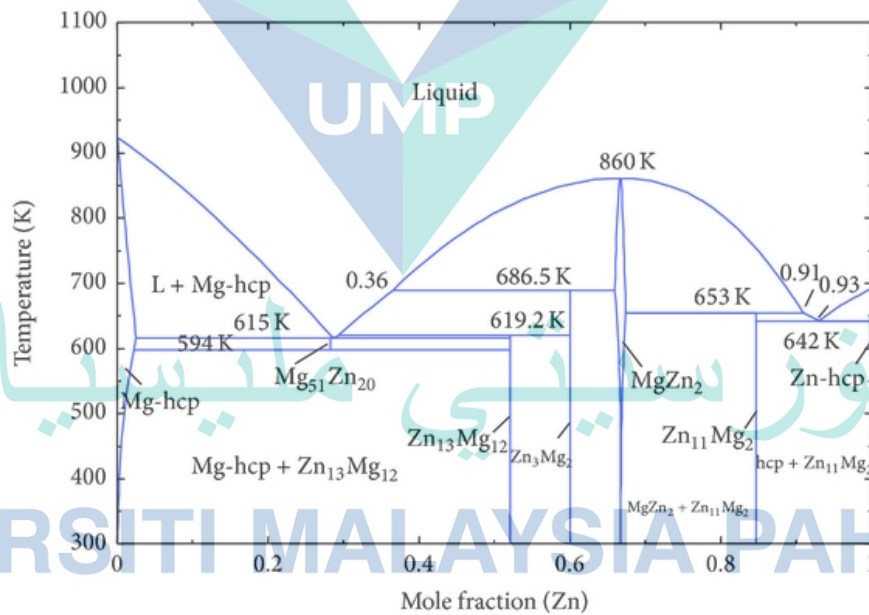


Figure 2.3 Mg-Zn binary phase diagram.

Source: Mezbahul-islam et al., (2014)

In addition, the binary phase diagrams explained that intermetallic compounds (IMCs), such as  $\beta$ - $Mg_{17}Al_{12}$  and  $Mg_2Al_3$  are the compounds that have been alloyed to

other elements, such as Al and Zn. By referring to the Mg-Al phase diagram, the IMC could be formed in the weld after solidifying process (Liu et al., 2014). Friction stir welding (FSW) affects the microstructure of AZ31 and AZ91 Mg alloys as the compounds of  $Mg_{17}Al_{12}$  and  $Mg_2Zn_{11}$  are present at the weldment area (Rouhi, Mostafapour, Ashjari, et al., 2016).

Mg has been alloyed with various elements, such as Al, Zn, Mn, and others to overcome the weakness of insufficient strength if Mg exists in pure form (Kumar et al., 2015). Mg alloys are designated based on one or two prefix letters that show the principal alloying elements. Two or three numerals show the percentage of the principal alloying elements and a letter with an alphabet (except for I and O) indicates standardized alloys. In addition, the symbol of temper of each metal follows the system in Al alloys, for example AZ91C-T6.

#### 2.4 Main Constituent Phase in AZ31 and AZ91 Mg Alloys

The typical microstructure of common Mg alloys is presented in Figure 2.4 and the main constituents in AZ31 and AZ91 alloys are listed in Table 2.2. The primary phase is alpha ( $\alpha$ ), a solid solution of Mg with minor compositions of Al and Zn. The alpha size depends on the casting/cooling condition with an average size of 100  $\mu m$ . The beta and gamma phases are formed during cooling when casting the alloy. To further increase the strength of the alloy, it is usually rolled or extruded after casting with varying degrees of reduction ratio of rolling process to reduce plastic deformation (James, 2012).

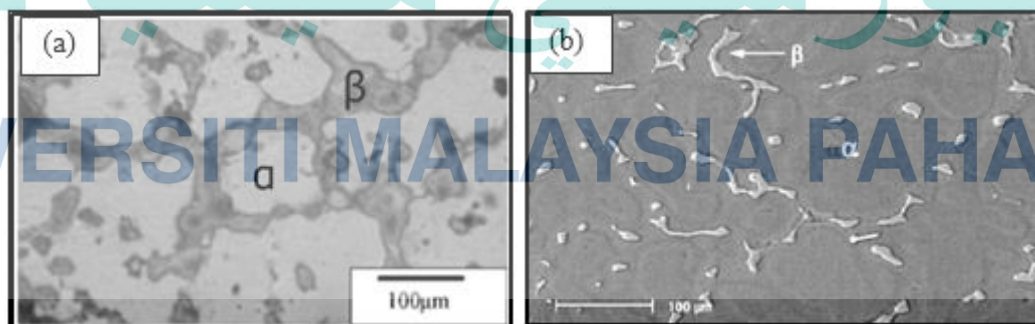


Figure 2.4 a) Microstructure of as-cast AZ31, b) microstructure of as-cast AZ91 Mg alloys.

Source: James, (2012)

Table 2.2 Main constituent phases in AZ31 and AZ91.

Phase	Nominal Composition
Alpha	Mg
Beta	Mg <sub>2</sub> Al <sub>3</sub>
Gamma	Mg <sub>17</sub> Al <sub>12</sub>

Source: Singh et al., (2016)

The microstructure of Mg alloys mainly consists of a matrix of  $\alpha$ -Mg grains and the second-phase particles consist of Mg<sub>17</sub>Al<sub>12</sub>, which exists in continuously high and low fraction and is finely divided. Mg<sub>17</sub>Al<sub>12</sub> phase would act as a barrier to stop corrosion propagation when it is continuous and has high population densities, where in low population densities and finely divided, Mg<sub>17</sub>Al<sub>12</sub> phase will serve as a galvanic cathode to accelerate corrosion (Zhao et al., 2019).

The introduction of Mn to Mg alloys is beneficial for lowering the effect of iron (Fe) impurity content in order to produce good corrosion resistance of Mg-Al alloys (Gandel et al., 2011). The formation of Al<sub>8</sub>Mn<sub>5</sub> IMC improves corrosion resistance by removing elemental Fe particles from Mg alloys. These particles are known to be cathodic to the matrix and could enhance the corrosion attack on the matrix. Mg has a corrosion potential lower than the second-phase particles, as each particle is formed by the reaction of Mg with a less-reactive metal (Cui et al., 2018).

## 2.5 Friction Stir Welding

Friction stir welding (FSW) is basically a solid-state joint technique (Singh et al., 2016) capable of joining alloys without melting and thus eliminating problems related to solidification (Figure 2.5). Amongst all traditional welding techniques, FSW is an energy proficient and versatile method of joining metals, alloys, and composites. As FSW does not require any filler material, the metallurgical problems associated with the method can also be eliminated and good quality weld can be obtained. FSW offers many advantages as listed in Table 2.3. A rotating tool is pressed against the surface of two abutting or

overlapping materials or plates, where the rotating tool moves in the same direction of the transverse direction known as the advancing side (AS), whereas the opposite rotation of the transverse direction is known as the retreating side (RS).

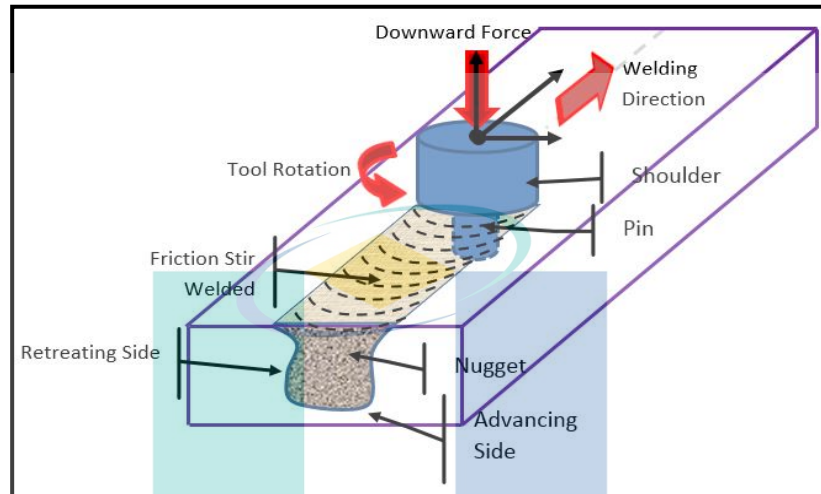


Figure 2.5 Schematic illustration of the FSW process of Mg alloys.

Source: Dhanapal et al., (2012)

Table 2.3 Advantages of friction stir welding.

Area	Benefits
Metallurgical	<ul style="list-style-type: none"> <li>• Fine microstructure</li> <li>• Absence of cracking</li> <li>• Solid phase process</li> <li>• No loss of alloying element</li> <li>• Good dimensional stability and repeatability</li> </ul>
Environment	<ul style="list-style-type: none"> <li>• Eliminate grinding waste</li> <li>• No filler required</li> </ul>
Safety	<ul style="list-style-type: none"> <li>• No shielding gas required</li> <li>• No welding arc or fumes</li> <li>• No UV radiation</li> </ul>
Mechanical characteristic	<ul style="list-style-type: none"> <li>• No spatter</li> <li>• High weld strength and toughness</li> <li>• Weld resists fatigue stress</li> <li>• Minimal distortion of the joined parts</li> </ul>

Source: Singh et al., (2016)

Two types of speed need to be considered in FSW: tool rotational speed and welding speed, which is also known as feed rate. These two parameters are important and



must be chosen wisely to ensure a successful and efficient welding cycle. Tool rotational speed affects frictional heat in producing a good weld joint. Frictional speed increases with increasing tool rotational speed, thus producing intense stirring and mixing of materials. Studies conducted on FSW of AZ31B observed that the quality of the welded region is highly affected by tool rotational speed and feed rate. (Afrin et al., 2007) discovered that the optimum parameter to achieve a good weld is 1,000 rpm. (Rouhi, Mostafapour, & Ashjari, 2016) found that the rotational speed of 1,250 rpm and feed rate of 40 mm/min produced a defect-free joint concerning AZ91 Mg alloy.

In general, it can be said that for the relationship of tool rotational speed and feed rate, increasing the rotational speed or decreasing the feed rate will result in a hotter weld. In order to produce a defect-free joint, it is necessary that the material surrounding the pin and tool is hot enough to enable the plastic flow required. (Wang et al., 2017) revealed a good mechanical performance of the FSW joint produced by moderate tool rotational speed of 1,200 rpm and feed rate of 120 mm/min. A study conducted by (Prasad et al., 2016) using tool rotational speed of 900 to 1,400 rpm revealed increased tensile strength with increasing rotational speed.

## 2.6 General Microstructural Evolution in Mg Alloys during FSW

Performing FSW on a material introduces a high degree of plastic deformation and heat into the system, which could change the grain structure. Three zones are produced during FSW, namely the stir zone (SZ), the thermomechanical heat-affected zone (TMAZ), and the heat-affected zone (HAZ), as shown in Figure 2.6.



Figure 2.6 Macrostructure cross section of friction stir welding showing the welded region.

Source: Salih et al., (2019)

The base metal (BM) beyond the welded area is unaffected by plastic deformation in Figure 2.7(a). The HAZ in Figure 2.7(b) is the area of the weld that has not undergone any plastic deformation, whereas the TMAZ in Figure 2.7(c) and the SZ in Figure 2.7(d) have a similar microstructure; however, the TMAZ is exposed to heat and deforms less than the SZ, which produced a recrystallized grain structure (Jaiganesh et al., 2017).

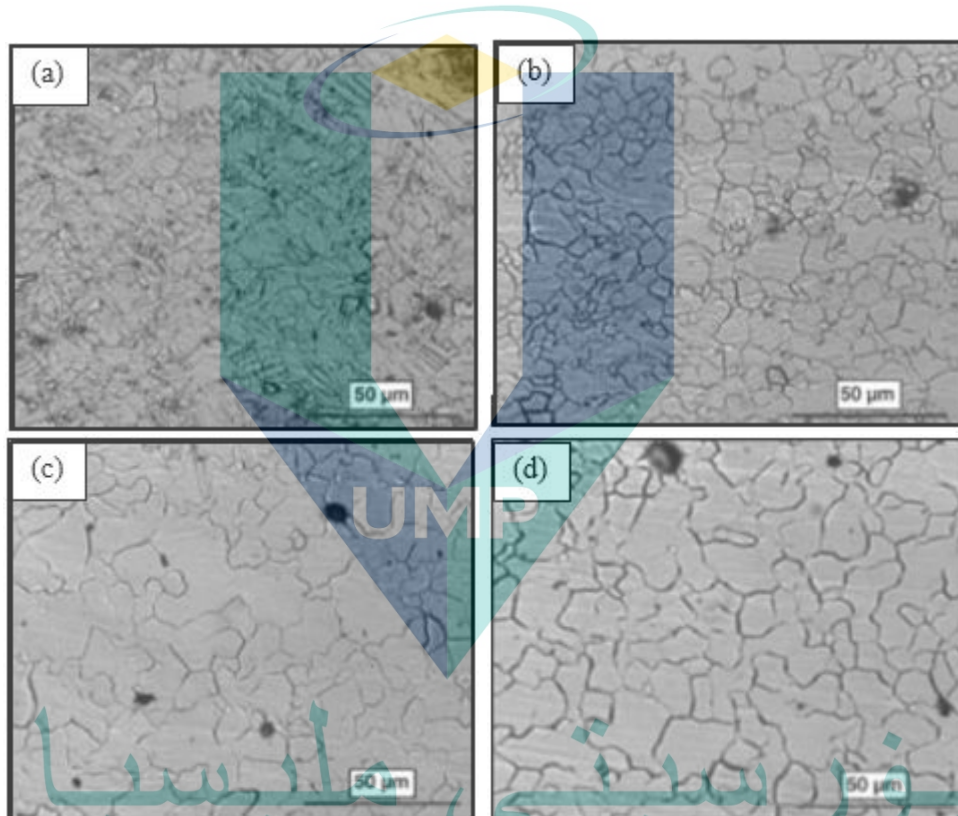


Figure 2.7 AZ31B-H24 typical optical micrograph: (a) base metal (BM), (b) Heat affected zone (HAZ), (c) thermomechanical heat affected zone (TMAZ), (d) stir zone (SZ).

Source: Jaiganesh et al., (2017)

The overall microstructure depends on important parameters, such as tool rotational speed, feed rate, shoulder diameter, and characteristics of materials being joined (Rai et al., 2011; Sharma & Singh, 2013; Xie et al., 2008). In FSW, the SZ is characterized by a fine, equiaxed fully recrystallized grain structure. Grains in this region are found to be plastically deformed and reduced in grain size (Pagar & Wable, 2016).

Various shapes of the SZ are usually observed after FSW, depending on the amount of heat experienced during welding and the type of joint. Two common shapes of the SZ are elliptical- and basin-shaped zones. The latter is usually formed due to the tilt angle and tool rotational direction or very high heat rate near the top surface.

Adjacent to the SZ is the region called the TMAZ where the BM grains are found to have undergone some deformation. This zone usually experiences a lesser degree of heat and deformation compared to the SZ and thus, partial or full recrystallization may take place at this region (Xie et al., 2008). The microstructure in this region is highly deformed and elongated due to the insufficient plastic deformation during FSW and thermal exposure (Jayaraj et al., 2017).

Adjacent to the TMAZ and further from the weld line is the HAZ. This zone is characterized by the fact that it undergoes a thermal cycle but does not experience any plastic deformation (Gharavi et al., 2015). The grain structure in this region is basically similar to the BM. However, the HAZ region is heated during joining, which produces some grain growth and dissolution of second-phase particles. The mechanical properties of FSW Mg alloys show that most failures of tensile test occurred in the HAZ region. The processing of AZ31 shows that the HAZ of FSW AZ31 has the lowest microhardness value. The HAZ experiences deformation, which leads to grain refinement or increase of dislocation density (Salih et al., 2019).

## 2.7 Deformation of Mg

### 2.7.1 Twinning

Twinning causes a change of microstructure, which is important for the deformation of Mg. The phenomenon occurs when a metal crystal lattice has a symmetrical orientation with the untwinned lattice due to shear stress (Zhang et al., 2013), as shown in Figure 2.8. Twin boundaries are a special type of grain boundary, where there is a specific mirror lattice symmetry. An atom on one side of the boundary is located in the mirror image position to those atom on the other side. The region of materials between these boundaries is known as a twin. Twins are produced from atomic displacement that is produced from mechanical shear force. Mechanical twins are typically observed in body-centered cubic (BCC) alloys and HCP.

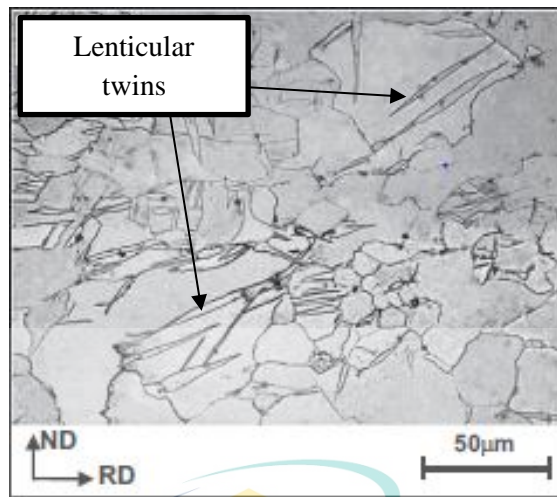


Figure 2.8 Microstructure of lenticular twins formed on the Mg alloy .  
 Source : Zhang et al., (2013)

The twins correspond to a region with relatively straight and parallel sides and different visual contrast than untwinned regions of the grain structure. Grain size is an important factor in twinning deformation because smaller grain size is less encouraging for twin nucleation compared to larger grain size (Wang et al., 2010). Liu et al., (2018) found that the microstructure that significantly refined after FSW is the SZ with an average grain size of 7.8  $\mu\text{m}$ . They found a lot of extension twin boundaries in the SZ as indicated by the red lines in the electron backscatter diffraction (EBSD) maps that represent  $\{10\text{-}12\}$  extension twin boundaries in Figure 2.9(a), and the inverse pole figure (IPF) maps are shown in Figure 2.9(b). The grains in red are suggested as the matrix of twinned grains. The volume fraction of twins is 53.6% in the SZ.

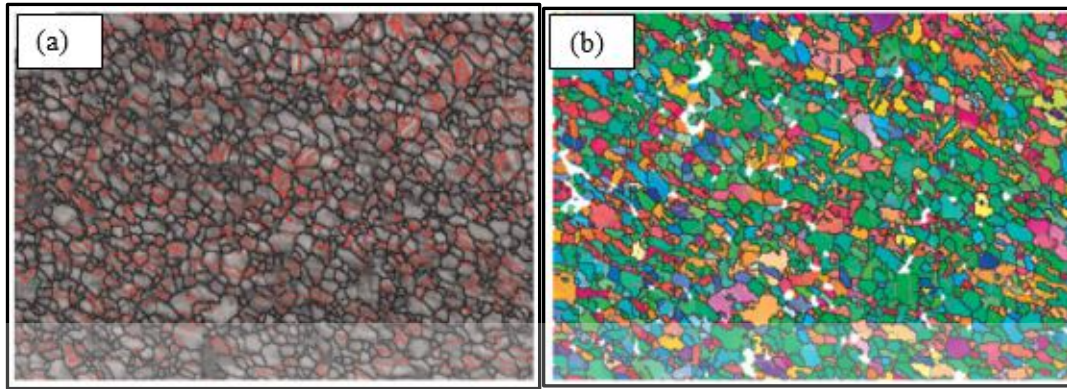


Figure 2.9 Electron backscatter diffraction (EBSD) maps of the stir zone (SZ).  
Source: Liu et al., (2018)

### 2.7.2 Dynamic Recrystallization

Recrystallization is the formation of new and equiaxed grains in a deformed material. The stored energy of deformation drives the formation and migration of a high-angle grain boundary. The recrystallization of Mg alloys is not complementary by obviously changing the crystallographic texture. Luna et al., (2018) reported that the heat input during FSW generates dynamic recrystallization (DRX), thus causing nucleation and refined grains.

Myśliwiec & Sliwa, (2018) found that grain size increased with increasing heat input because Mg alloys experienced DRX compared to Al alloys, which reflected that the recrystallization temperature of Mg alloys is about 523 K and lower than the recrystallization temperature of Al alloys. (Cottam et al., 2008) stated that the texture of DRX grains of Mg alloys followed the parent's grains closely, indicating the texture is dominated by deformation rather than nucleation or growth. Temperature and slip system activity induced the activity of DRX by reducing twinning deformation and increasing the activity of a non-basal slip system.

Shahnam et al., (2019) reported the occurrence of DRX during FSW of AZ31 alloy, which could be observed at the SZ. The SZ located under the tool pin underwent full DRX, resulting in ultra-fine grains with an average grain size of  $950 \pm 45$  nm as

shown in Figure 2.10(a) as compared to the BM that consisted of a single-phase coarse grain structure with an average grain size of  $75 \pm 6 \mu\text{m}$  as presented in Figure 2.10(b).

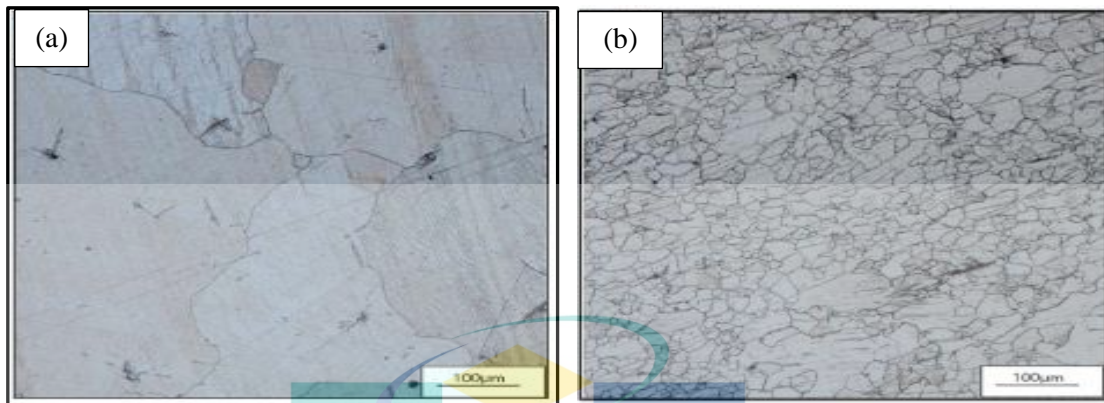
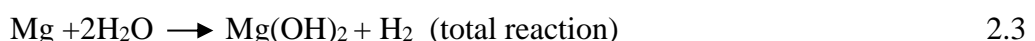
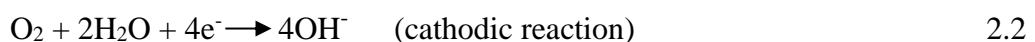


Figure 2.10 Microstructure of the: (a) BM, (b) recrystallized grains after dynamic recrystallization occurred.

Source: Shahnam et al., (2019)

## 2.8 Corrosion of Mg alloy

Mg offers a combination of good castability, lightweight, and mechanical properties without most electrochemical active species that would cause the metal to corrode in many environments. Any corrosion phenomenon requires (a) generation of electrons (i.e., anodic reaction), (b) consumption of electrons (i.e., cathodic reaction), and (c) a medium for electron transport (i.e., electrolyte). For Mg in an aqueous medium, electron generation occurs predominantly with metal dissolution reaction, which is given by Equation 2.1. Hydrogen evolution is the predominant cathodic reaction as given by Equation 2.2 for consumption of electrons. These reactions resulted in the formation of Mg hydroxide ( $\text{Mg}(\text{OH})_2$ ) as given by Equation 2.3, which dissolves and comes into equilibrium with an aqueous medium at pH around 11 (Song et al., 2017).



Corrosion can be confirmed visually using a scanning electron microscope following immersion test in an aggressive environment. The dissolution of Mg in an aqueous solution occurs by the reduction of water to produce  $\text{Mg}(\text{OH})_2$  and hydrogen

(H<sub>2</sub>) gas. The Mg(OH)<sub>2</sub> corrosion product film is crystalline in nature, which can act as an electrical insulator. In addition, the production of Mg(OH)<sub>2</sub> corresponds to insoluble Mg<sup>2+</sup>, as Mg<sup>2+</sup> that is left in the metal lattice cannot be tallied in the electrolyte but instead is combined into a surface film (Thomas et al., 2015).

## 2.9 Microstructural Effect on Corrosion

FSW has a noticeable effect on the microstructure of the weld area and the process alters the grain size, precipitate distribution, twins, and dislocation density (Adamowski & Szkodo, 2007). Therefore, it is very important to understand the effect of these factors on the corrosion of welded Mg alloys.

Grain size contributes a large effect on the corrosion resistance of Mg alloys. Small grain size reduces the corrosion rates as compared to the samples with larger grain size in the same corrosive environment (Song & Xu, 2013). They proposed that the grain boundary of AZ31 Mg alloys acts as a retarder to the development of corrosion and thus, alloys with finer grains and additional grain boundaries are found to promote good corrosion resistance.

## 2.10 Micro-galvanic Effect of Alloying Elements

Galvanic corrosion takes place when dissimilar metals are placed in contact in a corrosive solution and potential difference produces electrons that flow between them. A less active metal will act as a cathodic metal with high positive potential, whereas an active metal will be corroded and act as an anode. Mg and its alloys have the lowest standard potential of -2.37 V<sub>SHE</sub>, which are usually highly susceptible to galvanic corrosion when coupled with other dissimilar metals (Thomas et al., 2015).

The existence of alloying elements such as iron (Fe), nickel (Ni), copper (Cu), and cobalt (Co) and a large amount of impurities in Mg alloys give significant disadvantages to corrosion resistance due to galvanic effect (Liu et al., 2018). The standard electromotive force (EMF) series and open circuit potential (OCP) can be used to predict the degree of galvanic corrosion. The free potential of Mg alloys is -1.67 V/SHE when exposed to an aqueous environment (Savguira et al., 2018).

The formation of a second phase such as impurities and alloying elements significantly affects corrosion resistance by serving as an effective cathode during corrosion (Liu et al., 2018). Microgalvanic corrosion occurs when the microstructure, including the presence of phases, acts as an anode and a cathode. This can happen because the Mg matrix has lower OCP than the surrounding second phases and also intermetallic compounds with a higher value of OCP. Thus, the matrix will be anodic and preferentially corroded (Dejia et al., 2017).

Mg with high Al content, for instance AZ80, is considered to be more resistant to corrosion due to the presence of  $\beta$ -phase ( $Mg_{17}Al_{12}$ ) that is cathodic than the matrix. There are three main phases in AZ80 alloy, namely substitutional solid solution in Mg ( $\alpha$  phase) and two intermetallic phases,  $\beta$ -phase ( $Mg_{17}Al_{12}$ ) that presents in a eutectic phase ( $\alpha + \beta$ ), and an intermetallic phase containing Mn, Fe, and Al at minor levels as shown in Figure 2.11 (Savguira et al., 2018).

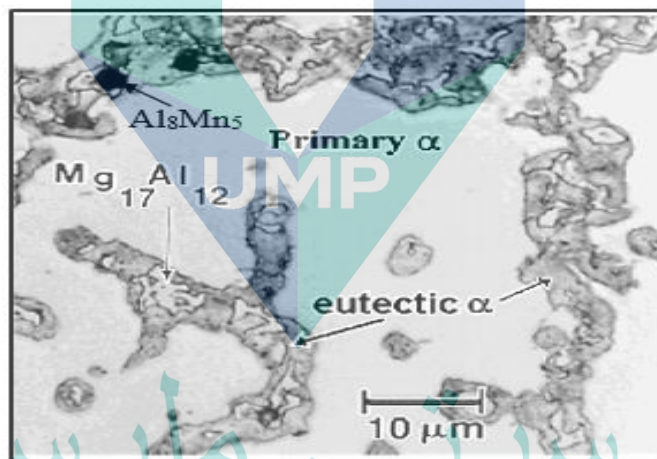


Figure 2.11 Microstructure of AZ80 Mg alloy.

source: Savguira et al., (2018)

According to the study conducted by (Liu et al., 2018), the samples of friction stir process (FSP) of AZ91 alloy revealed uniform corrosion attack identified by some shallow and widespread holes, whereas as-cast samples experienced more severe corrosion attack. The corrosion initiated in the  $\alpha$ -Mg matrix is due to galvanic effect for both samples. The initial location is at the edge of the  $\beta$ -phase due to the microgalvanic corrosion between the  $\alpha$ -Mg/ $\beta$ -phase galvanic couple in Figure 2.12. Figure 2.12(c) is a magnified image of Figure 2.12(b).



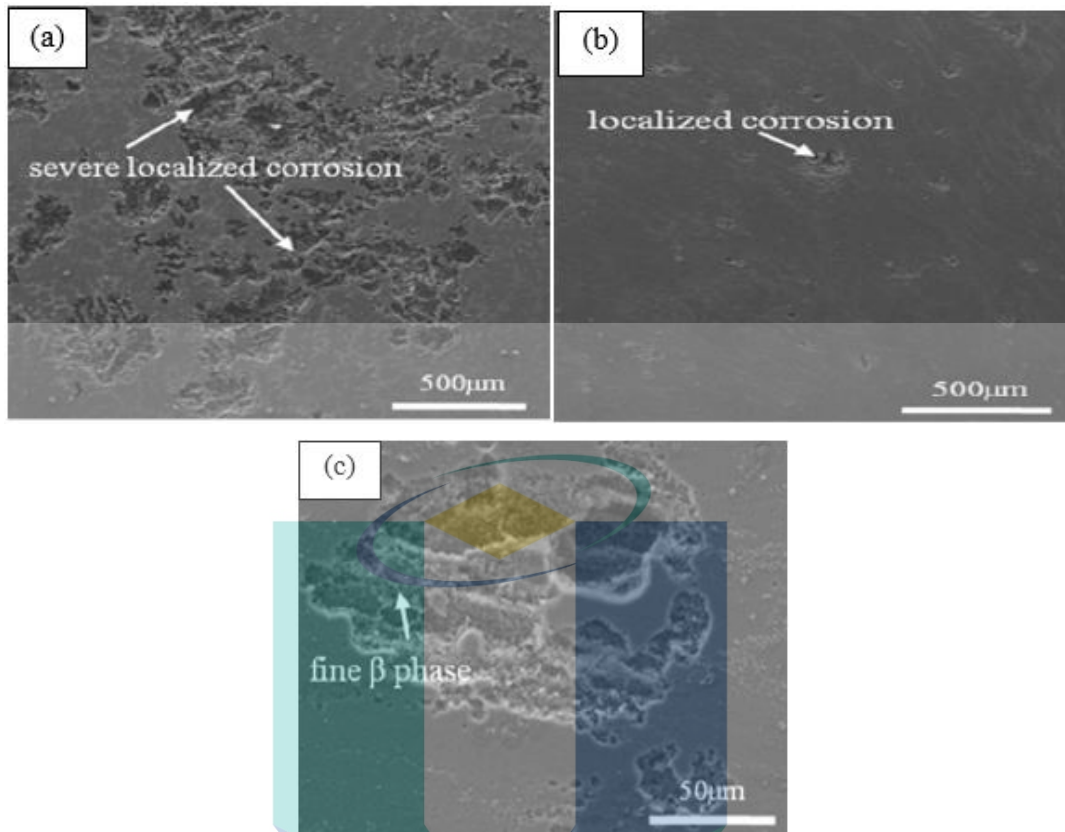


Figure 2.12 SEM micrographs of corrosion morphology on the surfaces of different AZ91 samples: (a) as-cast sample, (b) FSPed sample, (c) magnified image of FSPed sample.

Source: Liu et al., (2018)

## 2.11 Common Type of Corrosion in Mg Alloys

### 2.11.1 Pitting Corrosion in Mg Alloys

One of the localized attack on Mg and its alloys is known as pitting corrosion. Pits are produced by corrosion at certain areas on a metal surface as shown in Figure 2.13 (Gui et al., 2019). Pitting corrosion is a localized corrosion of a metal surface confined to a point or small area (Ghali et al., 2013). A small area at Mg alloys will oxidize to release electrons ( $e^-$ ) and form metal ions ( $Mg^{2+}$ ) and simultaneously generate excessive  $H_2$  gas at the surrounding. Then, the electrons travel to the surface of the metal and react with oxygen ( $O_2$ ) and water ( $H_2O$ ) to produce hydroxide ions ( $OH^-$ ).  $Mg^{2+}$  and  $OH^-$  will then react to form  $Mg(OH)_2$ . Pitting is an initiator for other corrosion effects, such as crevice, erosion, filiform corrosion, and others. Pitting is found on passive metals and alloys, such as Al and Mg alloys when the ultra-thin passive film known as the oxide film is chemically or mechanically damaged (Song et al., 2017).

Initiation, propagation, termination, and reinitiation are the stages of pit formation during corrosion (Hu et al., 2014). Factors influencing pitting corrosion are chemical composition, grain size, heat treatment condition, morphology, and distribution of the second phase (Atrens et al., 2013; Cao et al., 2016; Zeng et al., 2009). The resulting pits can become wide and shallow or narrow and deep, which can rapidly go through the wall thickness of a metal. Figure 2.14 presents pitting corrosion on the surface of AZ31 Mg alloy.

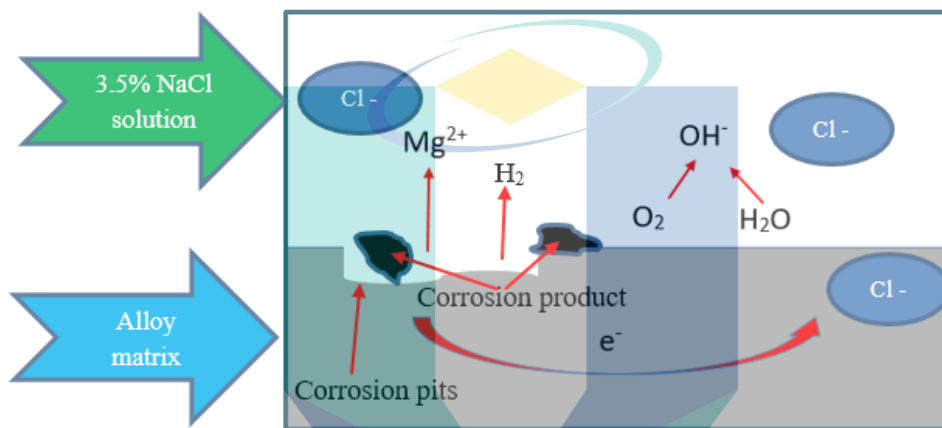


Figure 2.13 Schematic diagram of pitting corrosion in Mg immerse in NaCl solution.  
Source: Gui et al., (2019)

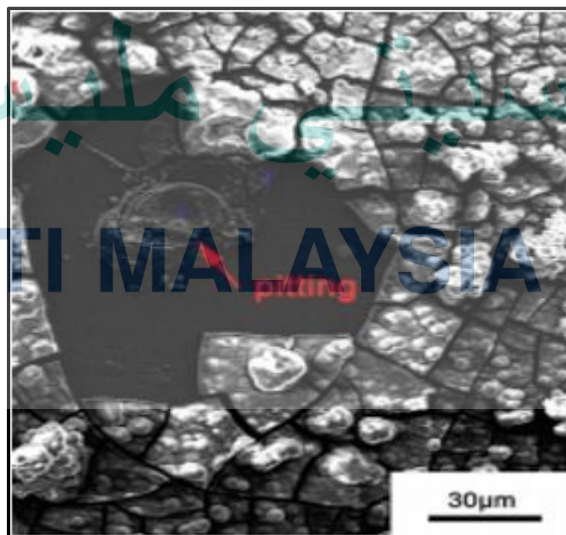


Figure 2.14 Pitting corrosion occurred on the surface of AZ31.  
Source: Cui et al., (2014)

Pitting is dangerous because it can lead to failure of the structure with a comparatively low overall loss of metal. The most possible environment for pitting corrosion to occur is in the marine environment because  $\text{Cl}^-$ ,  $\text{Br}^-$ , and  $\text{I}^-$  ions are in abundant and this will promote the pitting corrosion of the metal because the metal is in intermittent or permanent contact with the aqueous media (Atrens et al., 2013).

The microstructure constituents of Mg alloys are usually characterized by the  $\alpha$ -Mg matrix and the intermetallic phase or second-phase particles, such as  $\beta$ - $\text{Mg}_{17}\text{Al}_{12}$  and  $\text{Al}_8\text{Mn}_5$  particles. Corrosion preferentially occurs around the second phase due to the higher potential difference between the second phase and the matrix. Song et al., (2017) revealed that the pitting corrosion of Mg alloys is associated with the microstructure, especially the second phase. An extruded Mg alloy AM50 was immersed in a natural 3.5 wt. % sodium chloride (NaCl) solution and corrosion pits occurred at the surrounding of Al-Mn particles as presented in Figure 2.15 (Zeng et al., 2009).

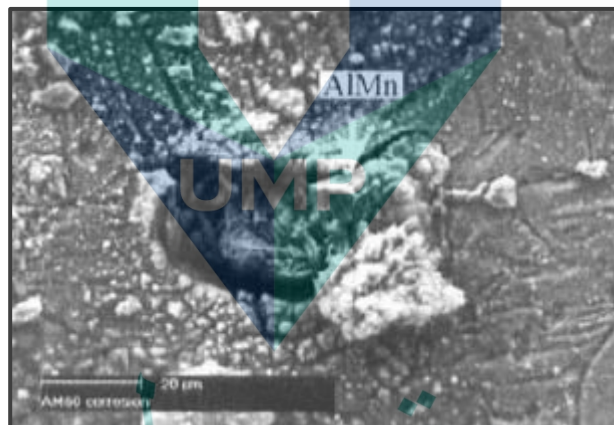


Figure 2.15 Pitting corrosion occurred at AlMn particles.

Source: Zeng et al., (2009)

### 2.11.2 Filiform-like Corrosion

An active corrosion cell moving across the metal surface results in filiform corrosion. The head represents the anode whereas the tail represents the cathode. This type of corrosion takes place under coating and an anodized layer. The filament starts as corrosion pits from any weak point on the surface, for instance mechanical scratches, cutting edge or flaws in the film, as shown in Figure 2.16.

According to (Zeng et al., 2009), pitting corrosion followed by filiform corrosion occurred at the welded area of AM50 Mg alloy. The corrosion morphology is influenced by the  $\beta$ -phase in the microstructure. On the other hand (Cao et al., 2006) found that the pits started from Mn-contained particles where the  $\alpha$ -Mg matrix was attacked and the corrosion propagated away from high Al areas. Schmutz et al., (2003) revealed that the earlier stage of corrosion of AZ91 alloy started with pitting corrosion and propagated as filiform-like corrosion. The filiform of Mg is driven by the difference of oxygen concentration between the head and the tail.

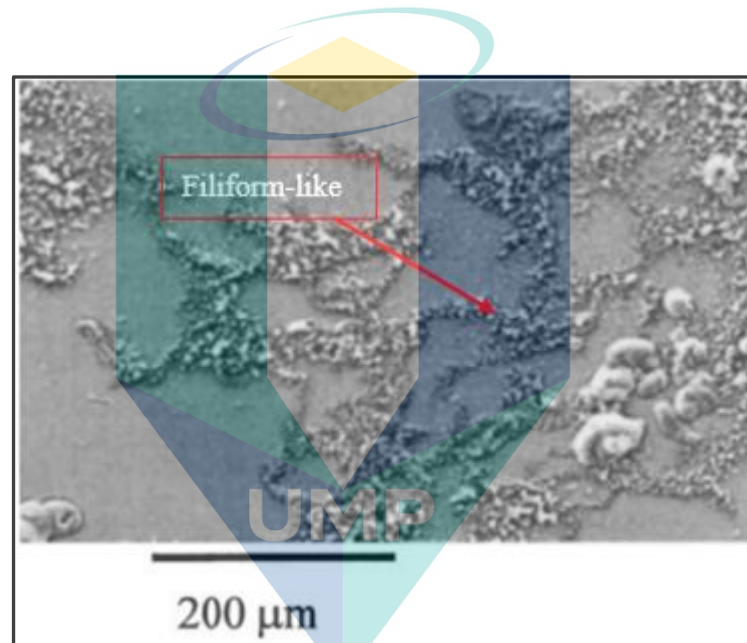


Figure 2.16 Filiform-like corrosion of AZ91.

Source: Schmutz et al., (2003)

Savguira et al., (2018) revealed that the corrosion mechanism of dissimilar AZ31/AZ80 FSW joint started with the formation of pitting corrosion and propagated to become filiform-like corrosion after 3 h of immersion time. The corrosion attack spread after 6 h of immersion time and covered most of the AZ31 area as shown in Figure 2.17, which is due to the microgalvanic coupling between the active  $\alpha$ -Mg matrix in AZ31 alloy and the noble Al-rich intermetallic particles in AZ80 alloy.

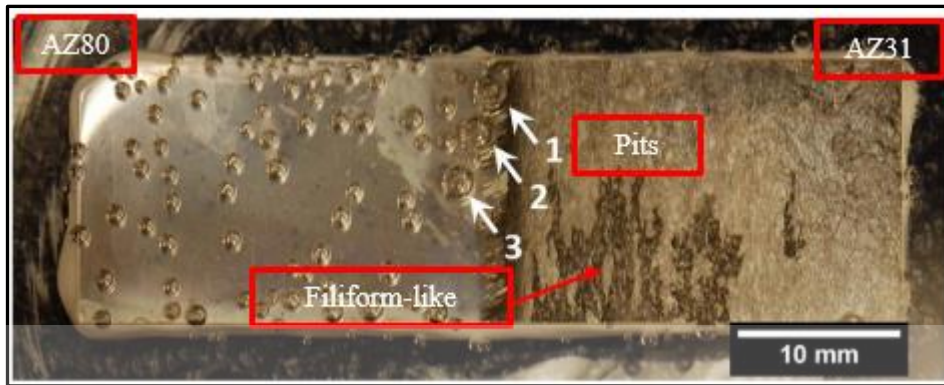


Figure 2.17 In-situ imaging of filiform corrosion of dissimilar AZ31/AZ91 FSW joint.

Source: Savguira et al., (2018)

## 2.12 Electrochemical Measurement

Potentiodynamic polarization test is a technique where the potential of an electrode is varied at a selected rate by applying current through the electrolyte. This method provides useful information regarding the corrosion mechanism and corrosion rate in a designated environment. The polarization technique involves changing the potential of the working electrode and measuring the current produced as a function of time (Esmaily et al., 2016).

There are two types of polarization: anodic polarization and cathodic polarization. Anodic polarization refers to the change of an electrode potential in the positive direction due to the withdrawal of electrons. Meanwhile, cathodic polarization refers to the process of adding electrons on the surface of the working electrode that becomes more negative and causes electrode deposition. The instantaneous corrosion rate ( $i_{\text{corr}}$  and  $E_{\text{corr}}$ ) can be determined from the potentiodynamic polarization method. The dissolution of Mg alloys during anodic polarization involves the evolution of  $\text{H}_2$  that increases with the amount of anodic polarization and deposition of the corrosion product (Esmaily et al., 2016; Thomas et al., 2015).

According to (Zeng et al., 2006), the corrosion rate of the weld zone is half of the BM due to finer grain size as shown in Figure 2.18. High welding speed and fast cooling rate of the weld improve corrosion resistance due to fine grains and a solid solution with

higher Al content. On the other hand, (Jayaraj et al., 2017) revealed that FSW of dissimilar materials of Al and Mg alloys led to poor corrosion resistance at the SZ. The corrosion rate of FSW dissimilar joint of Al/Mg alloys is higher in an acidic medium than alkaline or neutral media. There is no passive film on the Mg alloy surface in the solution with pH less than or equal to 7 because  $Mg(OH)_2$  is unstable under such condition.

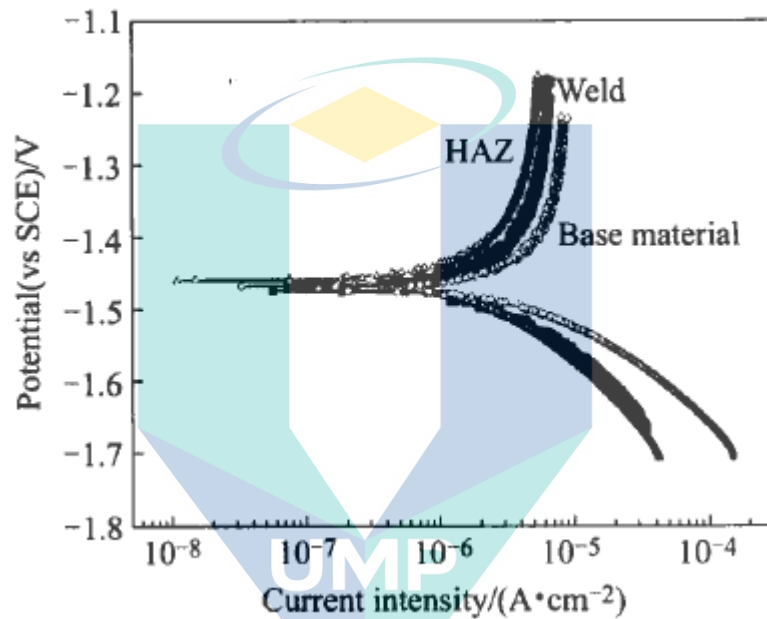


Figure 2.18 Polarization curves of AZ91D weld and its base materials in 3.5% NaCl solutions.

Source: Zeng et al., (2006)

Liu et al., (2019) revealed that the corrosion resistance of FSW samples is better than the base material. The corrosion potential of the material is  $2.734 \times 10^{-3} \text{ A/cm}^2$  and the corrosion potential for FSW is  $1.092 \times 10^{-3} \text{ A/cm}^2$  as presented in Figure 2.19. An improved corrosion rate of the FSW samples compared to the base material is due to the recrystallization of grain structure. The corrosion crack did not expand further into the depth after the grains are detached with fine grains while for coarser grains, the crack propagated further to form a large etch pit.

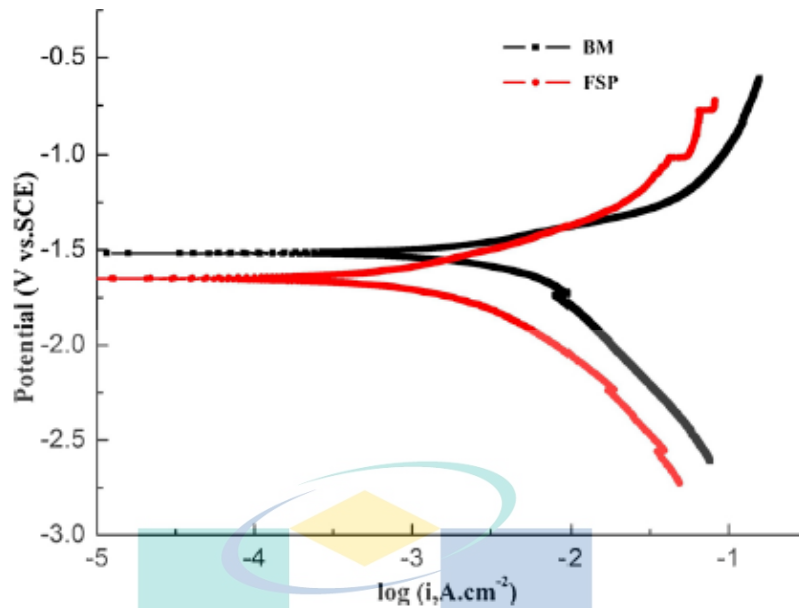


Figure 2.19 Polarization curve of the BM and FSW samples.  
Source: Liu et al., (2019)

### 2.12.1 Weight Loss and Hydrogen Evolution Test

Two non-electrochemical test methods commonly used in measuring the corrosion rate of Mg alloys are H<sub>2</sub> gas evolution and weight loss measurement (Thomas et al., 2015). Both methods are considered by most of the researchers as the standard benchmark. The weight loss measurement method is carried out using H<sub>2</sub> evolution test, in which the weight of the samples is measured in gram prior to the experiment and also after the exposure to the corrosive media for a period of time (Song et al., 2014).

Another method to determine the corrosion or degradation rate of Mg alloys is through H<sub>2</sub> evolution test. This method determines the electrochemical reaction for Mg alloys involving the evolution of one H<sub>2</sub> atom of Mg, which corresponds to the evolution of one mol of H<sub>2</sub> gas (22.41 g) is equal to 1 mol of Mg (24.13 g) dissolution. This volumetric method is simple and widely used by most researchers. The rate of H<sub>2</sub> evolution reaction increases with anodic polarization due to the negative difference effect (NDE) phenomenon (Thomas et al., 2015).

According to the investigation conducted by (Huang et al., 2018) on the FSW of AZ80, the corrosion rate obtained from weight loss ( $P_W$ ) and  $H_2$  evolution rate ( $P_H$ ) of fine grains (FG) and coarse grains (CG) decreased with the increase of immersion time. This indicated that the corrosion product formed reduced the corrosion rate with the extension of immersion time. From the graph in Figure 2.20, the samples of FG showed better corrosion resistance than the CG during the entire experiment.

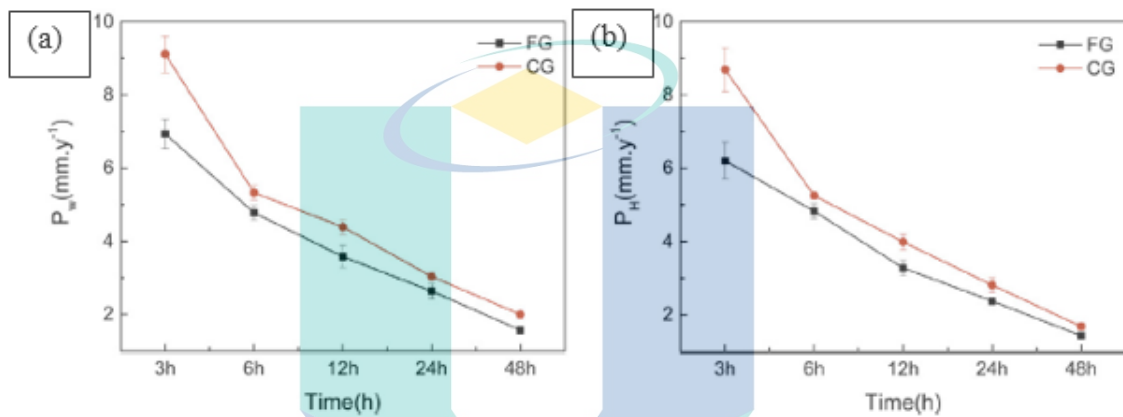


Figure 2.20 Corrosion rates of fine-grained (FG) and coarse-grained (CG) specimens convert from the (a) weight loss and (b) hydrogen evolution.

Source: Huang et al., (2018)

The research conducted by (Liu et al., 2018) on the FSP of AZ91 Mg alloy revealed that the FSP achieved a substantially lower  $H_2$  evolution volume on the top surface (TS) and the cross-section surface (CS) during the immersion test. Figure 2.21(a) shows that the  $H_2$  evolution rate of the as-cast sample increased rapidly with immersion time. The amount of  $H_2$  derived from the cathodic reaction is equivalent to the amount of Mg dissolution in the anodic reaction; thus, it is suggested that the as-cast sample showed a higher corrosion rate than the FSP samples. The mass loss measurement in Figure 2.21(b) indicated similar results to the  $H_2$  evolution rate where the as-cast sample showed the highest corrosion rate compared to the FSP samples.



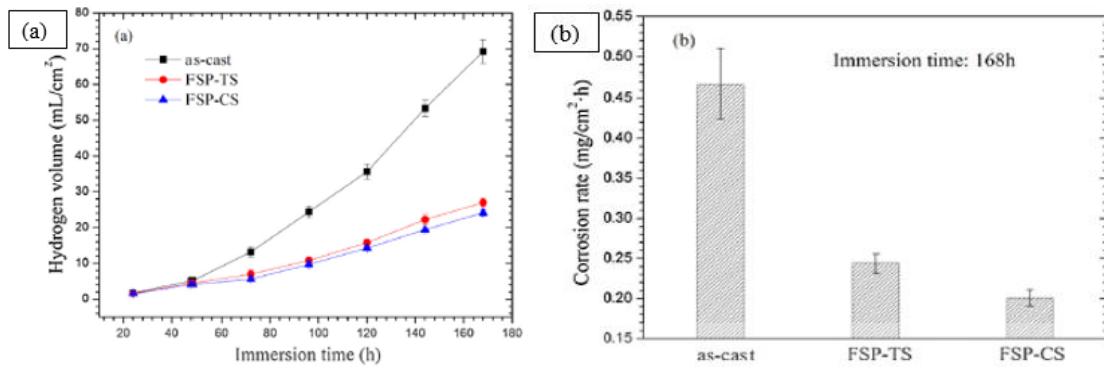


Figure 2.21 Mg dissolution of AZ91 samples, (a) Hydrogen evolution rate (b) weight loss rate after 1 week of immersion.

Source : Liu et al., (2018)

Yao et al., (2020) examined the corrosion behavior of different regions in the FSW of AZ31 alloy. The corrosion rate of the samples in different regions was calculated from the weight loss measurement method and presented in Figure 2.22. The graph showed that the TMAZ possessed the highest corrosion rate mainly due to the non-uniform microstructure and larger grain size. The result also showed that the HAZ possessed better corrosion resistance compared to others due to the presence of uniform grain structure.

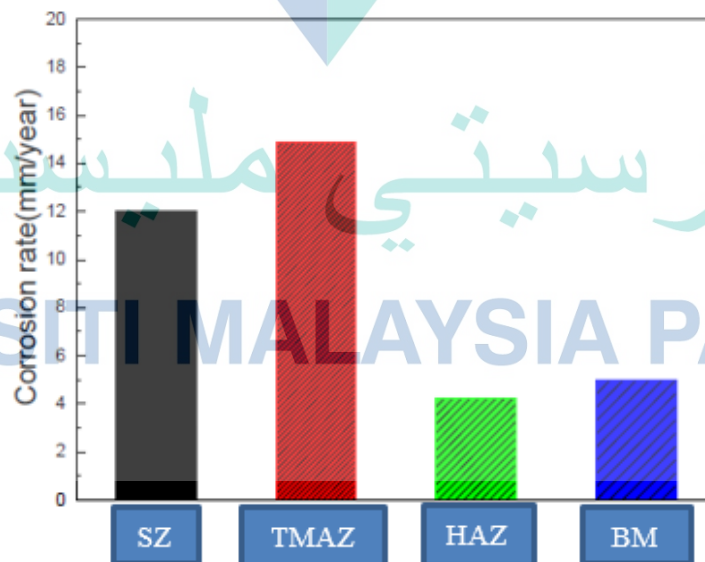


Figure 2.22 Corrosion rate of the specimens in different regions evaluated after 7 days of immersion in 3.5 wt.% NaCl solution.

Source: Yao et al., (2020)

### 2.13 Summary

Based on the literature, magnesium alloys have gained interest due to its low density and high strength to weight ratio which are promising for commercial application especially in automotive industries. Conventional welding technique obstruct the joining of magnesium alloys because of some defect produce during welding such as porosity, hot crack and high residual stress. FSW is a solid state joining method that can eliminate the welding defect associated with the conventional welding technique. FSW also introduce heat into the material system, which could change the microstructure due to the deformation mechanism of Mg alloys. There are several region produce during FSW, namely stir zone (SZ), thermomechanical heat affected zone (TMAZ) and heat affected zone (HAZ). The overall microstructure depends on the important parameters such as tool rotational speed and welding speed. However, poor corrosion resistance of magnesium alloys in corrosive environment has limited their growth in industries. The corrosion of magnesium occurs through dissolution of magnesium in aqueous environment with water producing magnesium hydroxide and hydrogen gas. Magnesium alloys degraded by localized corrosion attack. Pitting and filiform like corrosion are the most common corrosion forms. Few works have addressed the effect of microstructure in magnesium especially the influence of deformation during welding on corrosion performance since the dynamic recrystallization occurred. Despite significant improvement in their mechanical properties, to date the microstructure evolution during FSW was not systematically characterized and correlation to its corrosion performance still limited.

اونيورسيتي ملايسيا فاهغ

UNIVERSITI MALAYSIA PAHANG

## CHAPTER 3

### METHODOLOGY

#### 3.1 Introduction

This chapter presents detailed experimental methods applied to achieve the objectives. This section includes material preparation, details of experimental setup, sample preparation, microhardness test, macro- and microstructure characterization, corrosion test, and analysis including hydrogen ( $H_2$ ) evolution test and electrochemical measurement by potentiodynamic polarization test. The microstructure development was characterized by optical microscopy (OM) and scanning electron microscopy (SEM) equipped with energy dispersive X-ray spectroscopy (EDX) for compositional analysis. The evaluation of corrosion performance was further conducted for the friction stir welded alloys.

#### 3.2 Research Flow

In this research, friction stir welding (FSW) technique was applied to produce the joining of AZ31 and AZ91 Mg alloys. FSW is a relatively new solid-state technique, which is a possible method to join parts made of magnesium (Mg) alloys. Two main FSW parameters were applied during the process: tool rotational speed and welding speed. The metallography was carried out at the weldment cross-section to observe the microstructures of the welded samples. After that, corrosion test was conducted by performing  $H_2$  evolution test and electrochemical measurement by open circuit potential (OCP) measurement and potentiodynamic polarization test. Figure 3.1 shows the flow chart of the research.

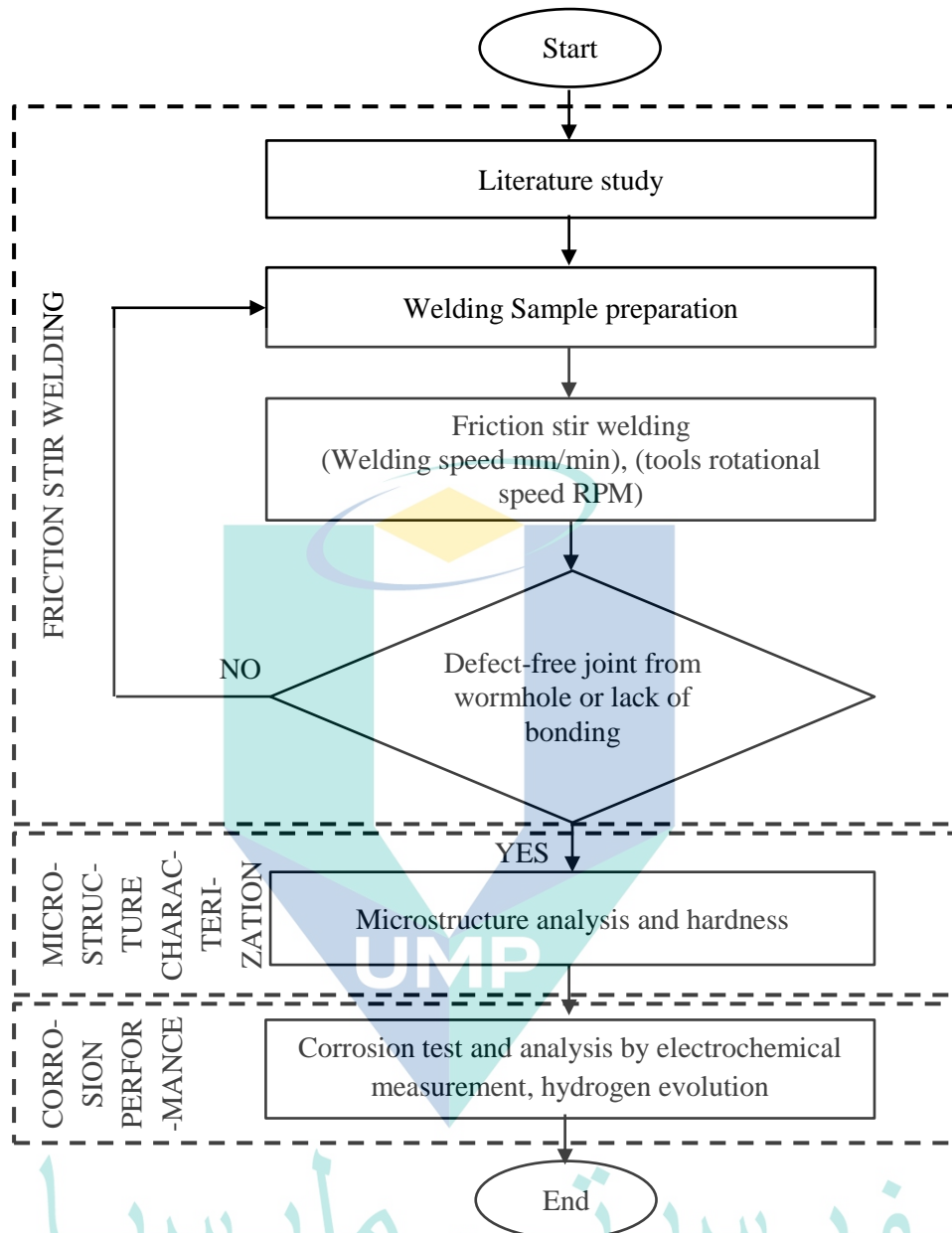


Figure 3.1 Research work flow chart.

### 3.3 Material Composition

Thin sheets of AZ31 and AZ91 Mg alloys were applied in this experiment as the base metal (BM). Prior to FSW, the elemental composition of the samples was determined using a spectrometer (Table 3.1).

Table 3.1 Elemental composition of Mg alloy (wt.%).

Composition	Al	Zn	Fe	Mn	Mg
AZ31	2.75	0.91	0.01	0.01	Balance
AZ91	8.67	0.85	0.02	0.03	Balance

### 3.3.1 Sample Preparation for Experiment

The sheets of AZ31 and AZ91 alloys with 3 mm thickness were used for this research work obtained from Yongquan metal and minerals. The samples were butt welded along the sheet. The schematic arrangement of the samples was prepared with the dimension shown in Figure 3.2. The required dimension for each welding specimen is 50 mm × 100 mm (width and length, respectively). The sample dimension was prepared according to the size of the welding jig.

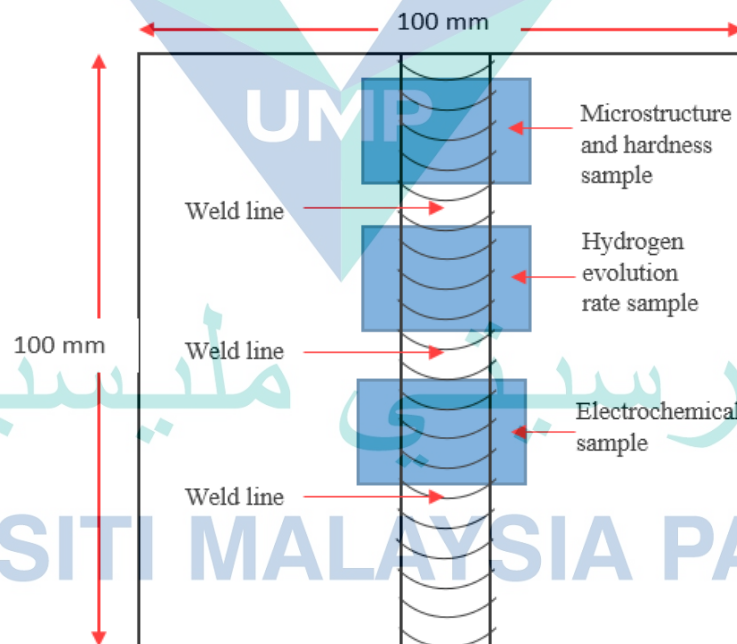


Figure 3.2 Schematic arrangement of welded sheet with cutting plan for microstructure, hardness, and corrosion samples.

### 3.4 Friction Stir Welding (FSW) Process

The FSW process was carried out using a universal milling machine as shown in Figure 3.3. Backing and clamping plates were used to support and hold the samples from slipping during tool pin penetration into the sample. Extra care was required to ensure the sample did not slip off and separated due to the large initial force. Figure 3.4 shows the backing and clamping plates for the FSW setup.

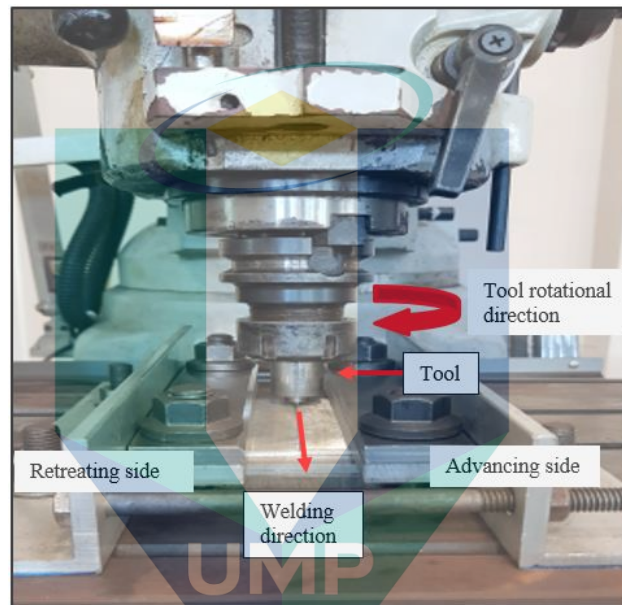


Figure 3.3 FSW milling machine.

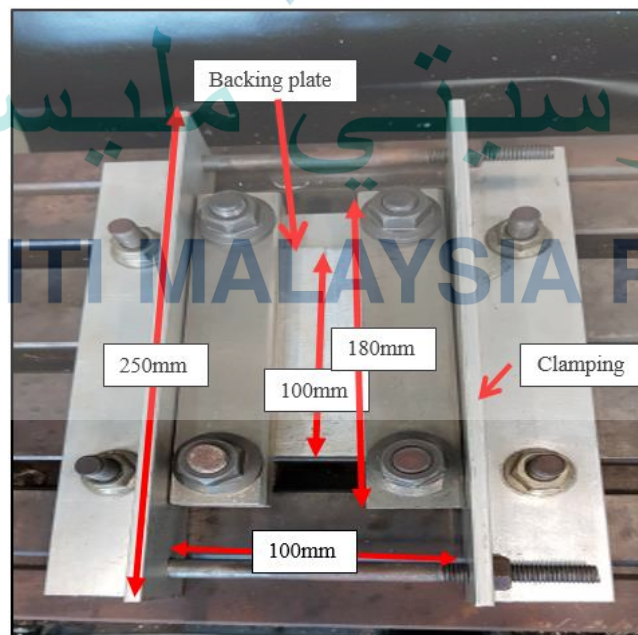


Figure 3.4 Backing and clamping plate.

Figure 3.5 presents the design of the tool used in FSW. The tool material used is chromium hot-work tool steels classified as group H13. This material is widely used in hot and cold work tooling application due to its excellent combination of high toughness and fatigue resistance. The use of a correct tool is important for controlling the material flow and governing the transverse rate during FSW (Singh et al., 2018).

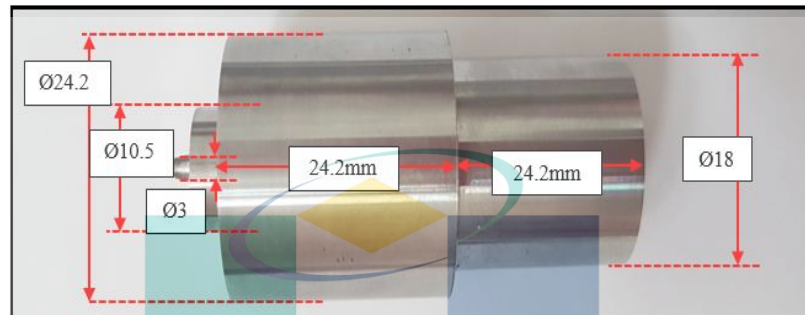


Figure 3.5 Tool design and dimension.

### 3.4.1 Experiment Setup

The parameters chosen in this experiment were tool rotational speed (rpm) and welding speed (mm/min). These two parameters are important for stirring and mixing the material with sufficient heat supply during welding. A good stirring and mixing condition is able to provide good penetration of welding with less defect. The range of parameters selected based on some preliminary experiment and previous studies is presented in Table 3.2.

Table 3.2 Welding sample arrangement.

Sample no	Welding speed (mm/min)	Tool rotational speed (rpm)
1	100	1,200
2	80	1,200
3	60	1,200
4	100	1,000
5	80	1,000
6	60	1,000
7	100	800
8	80	800
9	60	800

### **3.5 Microstructure Characterization**

#### **3.5.1 Sample Preparation**

The characterization of weld appearance is important to determine the properties of the material. The samples for microstructure characterization were prepared according to the standard guide for preparation of metallographic specimens (ASTM E3-11) (Standard, 2004b) , by sectioning the samples with an abrasive cutter and cold mounted in the epoxy resin. The microstructure region of interest was the cross-section of the welded sheet with the dimension of 1 cm × 0.3 cm (thickness). The samples were mechanically ground with 320, 400, 600, 800, 1,200, and 2,500 grit silicon carbide (SiC) papers, polished with 3, 1, and 0.5 μ diamond paste, and finished with oxide particle suspension (OPS). Next, the samples were cleaned with distilled water and ethanol and then quickly dried. Finally, the samples were etched using acetic-picral etchant solution for grain observation.

#### **3.5.2 Characterization Using Optical and Scanning Electron Microscope (SEM)**

The microstructure images of all the welded samples were observed using an Olympus optical microscope under the bright field mode. The images of the base metal (BM), the stir zone (SZ), the heat-affected zone (HAZ), and the thermomechanical heat-affected zone (TMAZ) were obtained using an optical microscope, and further analysis on grain size and intermetallic particles was performed using ImageJ software according to the standard test methods for determining average grains size (ASTM E-112) (Standard, 2004a).

In order to reveal the localized elemental composition, as well as grain and particle morphology, SEM and EDX were employed. The imaging and detection were subjected to the acceleration voltage of 10 kV and working distance of 10 mm. The EDX analysis was obtained by point spectrum and mapping. Figure 3.6 shows the schematic principle of SEM and its function.



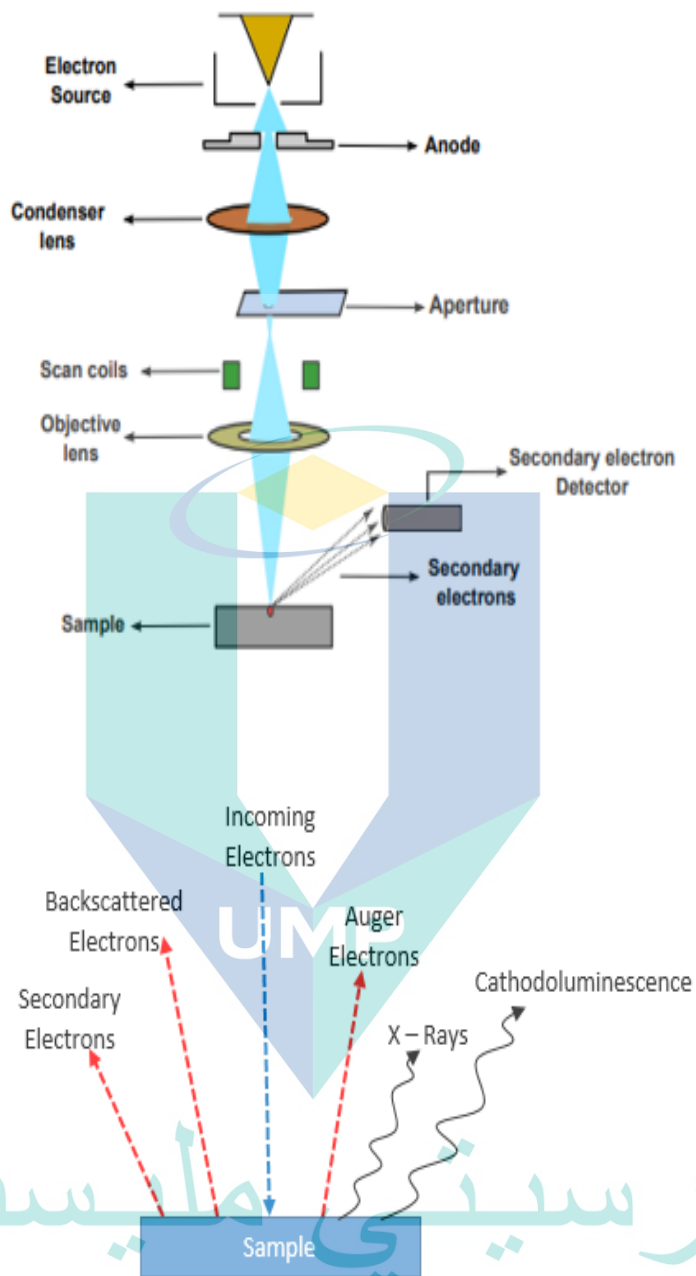


Figure 3.6 SEM principle and its function

### 3.6 Hardness Test

Hardness is a measure of the resistance of a metal to plastic deformation. The data of hardness profile for a welding sample are important for the joint strength. The hardness of a metal or alloy is measured by forcing an indenter into its surface. In this study, Vickers microhardness test was conducted by using a Vickers microhardness machine. The procedure of indentation followed standard test method for micro indentation hardness

of materials (ASTM E-384) (Bailey & Baldini, 2008) , which specifies a range of light loads using a diamond indenter with 500 kg of load (HV0.5).

The hardness value (HV) was determined by the formula  $F/A$ , where F is the force applied to the diamond in kilograms-force and A is the surface area ( $\text{mm}^2$ ) of the resulting indentation in  $\text{mm}^2$ . A constant load was used for a dwell time period of 10 s. The hardness test was conducted on the similar samples for microstructure characterization. Overall, 10 indentation points were measured across the BM (AZ31) – TMAZ – HAZ – Weldment – HAZ – TMAZ – BM (AZ91). The hardness profile of the samples was then analyzed and plotted in a graph.

### 3.7 Corrosion Test

#### 3.7.1 Hydrogen Evolution Test

Hydrogen evolution test is a common immersion test for Mg. The ‘strange’ cathodic reaction of Mg indicates that the degradation of Mg is correlated to the evolution of almost continuous  $\text{H}_2$  gas. This test aims to determine the corrosion or degradation rate of Mg samples within a specific duration. By conducting  $\text{H}_2$  evolution test, the evolution of one  $\text{H}_2$  gas molecule from one atom of Mg, which corresponds to the evolution of 1 mol of  $\text{H}_2$  gas (22.41 g), is also equal to 1 mol of Mg (24.31 g) dissolution. Thus, the corrosion rate of Mg by weight loss measurement is equal to the  $\text{H}_2$  gas evolution rate.

The samples for  $\text{H}_2$  evolution experiment were sectioned from the welded alloys by using an abrasive cutter in the material laboratory. Tissue papers were used to wrap the samples to avoid pressure marks on the sample surface during clamping and cutting.

The samples were sectioned to the dimension of  $1.5 \text{ cm} \times 2 \text{ cm}$  as shown in Figure 3.7.

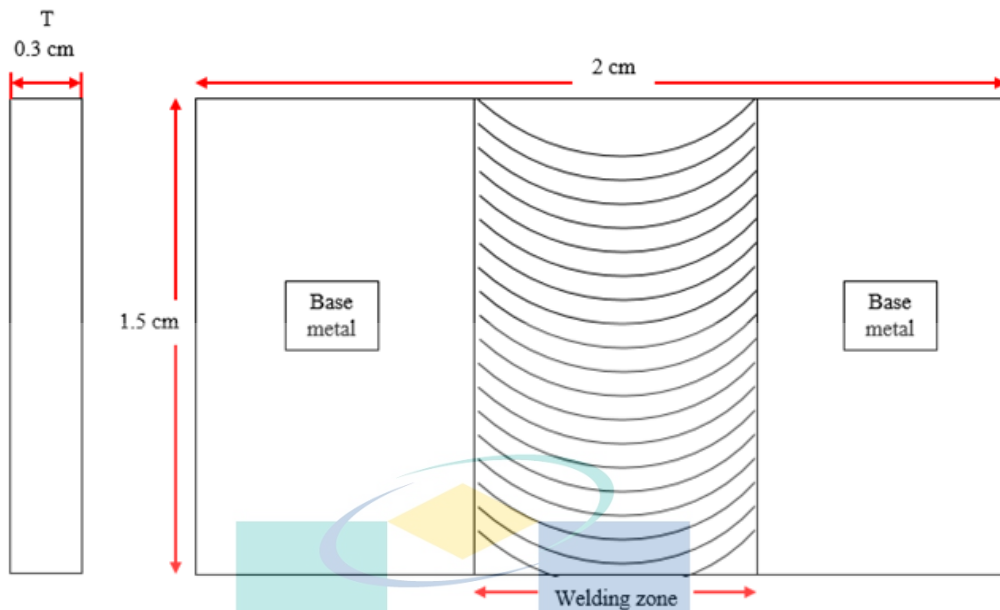


Figure 3.7 Schematic diagram of sample for hydrogen evolution test.

All the exposed sample surfaces were mechanically ground with 1,200 and 2,500 grit SiC papers to obtain a fine surface without deep scratch and contaminants. The total surface area of the samples was calculated and recorded. The samples were tied with a fishing rope and submerged in a glass beaker filled with 3.5 wt. % of sodium chloride (NaCl) aqueous solution following standard practice for laboratory immersion corrosion testing (ASTM G31-72) (Bailey & Baldini, 2008b). A burette was attached to a funnel, hung, and placed above the filled beaker as shown in Figure 3.8(a). The samples were immersed for 6 days (i.e., 144 h) at the range of solution temperature of 22 to 25 °C. The change of NaCl solution volume in the beaker within the duration is equivalent to H<sub>2</sub> gas evolution. The change of solution volume was recorded and the data were plotted in a graph. The observation was carried out using a USB microscope camera as shown in Figure 3.8(b).

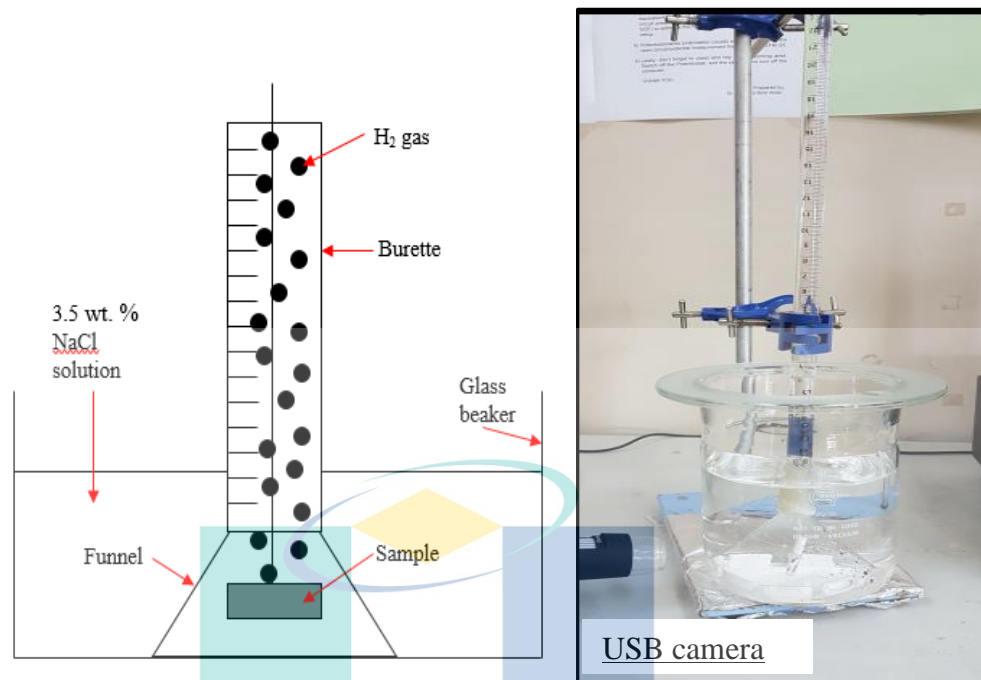


Figure 3.8 (a) Schematic diagram of hydrogen evolution test, (b) Experiment setup for hydrogen evolution test.

After exposure to 6 days, the samples were taken out and rinsed with distilled water and ethanol. The removal of corrosion product was then performed according to the standard practice for preparing, cleaning, and evaluating corrosion test specimens (ASTM G1-90, 2003). The samples were immersed in boiling chromium trioxide ( $\text{CrO}_3$ ) solution containing silver nitrate for about 5 minutes to remove the corrosion product. Further, the samples were rinsed with distilled water, ethanol, and dried. The corrosion morphology of corroded samples after corrosion product cleaning was then observed by using scanning electron microscope (SEM). The weight of the sample prior and after immersion were measured, in order to determine the weight loss (equation 3.1) and corrosion rate (equation 3.2) subsequently. The formula for corrosion rate measurement is displayed as follows;

$$w = w_o - w_1 \quad 3.1$$

Where,

$w$  = weight loss in grams,

$w_o$  = original weight prior test in gram;

$w_1$  = final weight after test in gram.

$$\text{Corrosion Rate (CR)} = \frac{K \times W}{A \times T \times D}$$

3.2

Where,

$K = 8.76 \times 10^4$  (Constant value)

$W$  = weight (g)

$A = [2(W \times L) + 2(W \times H) + 2(L \times H)]$  (cm<sup>2</sup>)

$T = 144$  hour

$D = 1.74$  g/cm<sup>3</sup>

### 3.7.2 Electrochemical Measurement by Potentiodynamic Polarization

Electrochemical measure is the method used to observe the corrosion behavior of a sample by applying current and measuring the potential different. Two electrochemical measurement methods were conducted: open circuit potential (OCP) and potentiodynamic polarization.

The exposure area was set to 1.5 cm × 2 cm and the sample was clamped to a crocodile clip and copper wire for electrical connection, as shown in Figure 3.9(a). Lacquer was used to cover the unwanted area including the crocodile clip. The electrochemical measurement was performed using a WonATech potentiostat equipped with three electrode cells, including a working electrode (i.e., the sample), a graphite rod as the counter electrode, and a saturated calomel electrode (SCE) containing potassium chloride (KCl) solution as the reference electrode, as shown in Figure 3.9(b). The measurements were conducted in a beaker filled with 3.5 wt. % of NaCl solution. Initially, OCP measurement was conducted for 300 s for each sample prior to the polarization test. The OCP value was recorded and plotted in a graph of corrosion potential versus time. The value of OCP indicates free or zero corrosion potential with no applied current during measurement.

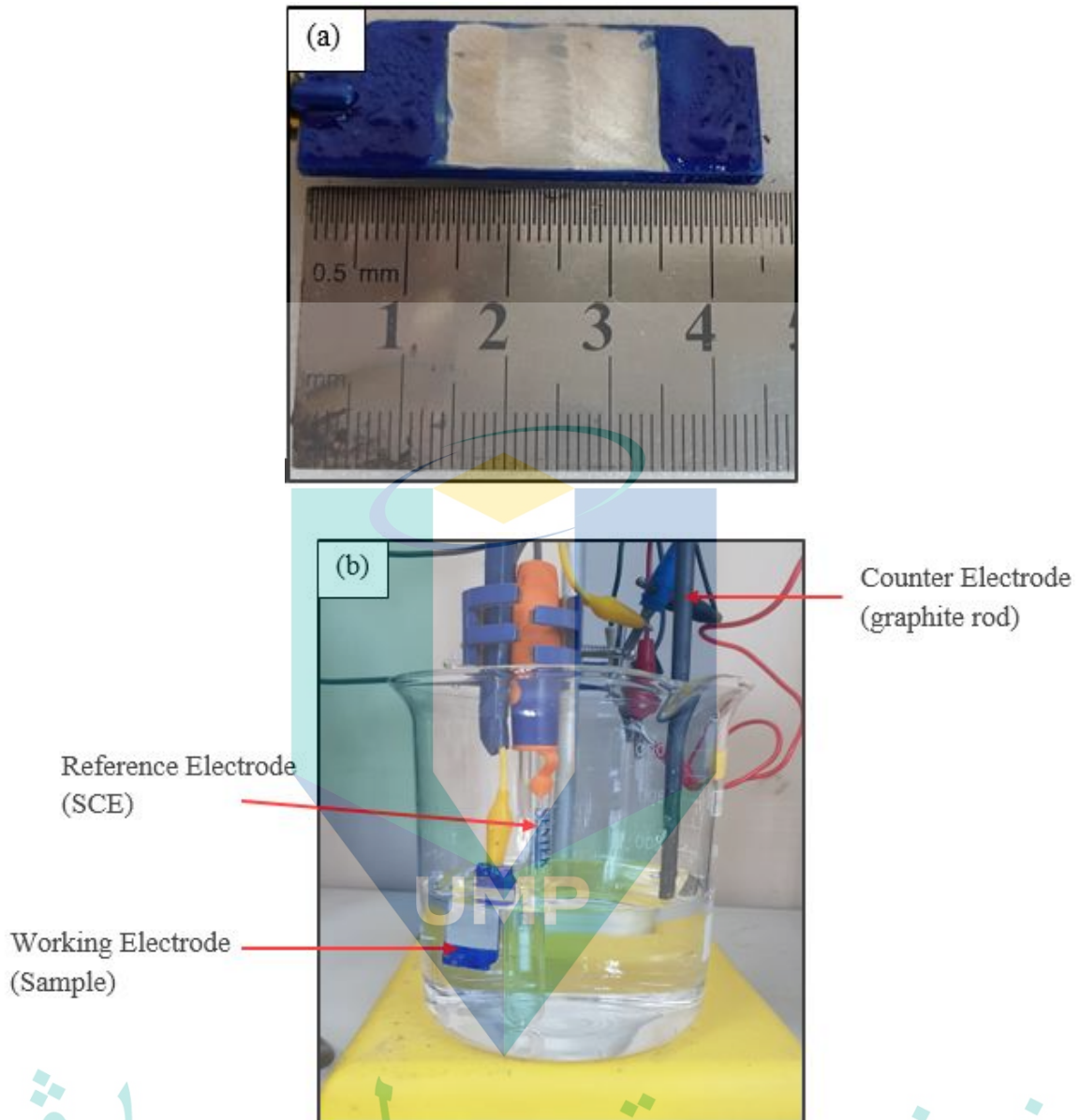


Figure 3.9 (a) Welded sample for electrochemical test (b) experiment setup for electrochemical test.

The relationship between the corrosion current density ( $i_{\text{corr}}$ ) and corrosion potential ( $E_{\text{corr}}$ ) at an electrode interface can be determined either by controlling the potential and measure the current or controlling the current and measure the potential. A potentiodynamic test is a qualitative technique to assess the behavior of metals, including active and passivation tendencies of metals. The passivation of a metal is developed when an oxide layer prevents corrosion growth. In some cases, the local area of a passive film breaks down the pitting corrosion that generally occurs on a small area of the metal.

The parameters for conducting potentiodynamic polarization test were set to the values listed in Table 3.3 based on the electromotive force (EMF). The  $E_{\text{corr}}$  and  $i_{\text{corr}}$  were evaluated from the intersection of anodic and cathodic branches of the curve. The data were recorded and a polarization curve was plotted.

Table 3.3 Potentiodynamic polarization test parameter setup.

Initial E (V)	Final E (V)	Scan rate (mV/s)	Sampling time (s)	Sample area (cm <sup>2</sup> )	Density (gm/cm <sup>3</sup> )
-1.8	1.00	5	1	3	1.75

### 3.8 Summary

The research framework, material preparation welding setup, micro-hardness test, macro- and microstructure characterization. The parameter used in this study are tool rotational speed (rpm) and welding speed (mm/min). The joining of AZ31/AZ91 was performed under rotational speed of 800, 1,000 and 1,200 rpm and welding speed of 60, 80, 100 mm/min. The microstructure development was characterized by optical microscopy (OM) and SEM, EDX for compositional analysis. The microstructure and micro-hardness test were performed across the BM (AZ31) - TMAZ- HAZ – weldment – HAZ – TMAZ – BM (AZ91). The corrosion behavior of the welded samples was evaluated using hydrogen (H<sub>2</sub>) evolution test and electrochemical measurement by open circuit potential (OCP) and potentiodynamic polarization.

## CHAPTER 4

### RESULTS AND DISCUSSION

#### 4.1 Introduction

This chapter presents the results for the weldability of AZ31/AZ91 alloys, microstructure analysis, and corrosion performance. Macro and microstructure characterization was performed at the weldment cross-section using optical microscopy (OM) and scanning electron microscopy (SEM). The corrosion behavior of AZ31 and AZ91 alloys was evaluated using hydrogen ( $H_2$ ) evolution test and electrochemical measurement by potentiodynamic polarization.

#### 4.2 Microstructure Development of FSW AZ31/AZ91 Alloys

Weldability is the joining of different materials without crack of AZ31 and AZ91 magnesium (Mg) alloys, and the completed process is shown in Figure 4.1. Defect-free sound joints were obtained for all the samples, which also did not contain any visible defect in the form of wormhole or lack of bonding defect. However, there was a small amount of flash and peeling on the welded surface. The formation of peeling is caused by overheating due to the friction between the pin shoulder and the surface (Sunil et al., 2015). For metallographic examination, the samples were sectioned perpendicular to the welding direction. The samples were mechanically ground with silicon carbide (SiC) papers and polished with diamond paste and oxide particle suspension (OPS). Etching was performed using acetic-picral solution, which was then rinsed with ethanol and dried. The general microstructure observation was conducted using an Olympus optical microscope and Zeiss SEM microscope, whereas the compositional analysis of particle distribution was performed using energy dispersive X-ray spectroscopy (EDX).





Figure 4.1 Weld surface morphology.

The optical micrographs of AZ31 and AZ91 microstructure are displayed in Figure 4.2. Figure 4.2(a) reveals recrystallized grains and intermetallic particles for the grain structure of AZ31 base metal (BM). The coarse grains have the mean grain size of 35  $\mu\text{m}$  as measured by the linear intercept method. Figure 4.2(b) indicates the occurrence of coarse grains, heavy twinning, and sub-grain nucleation due to dynamic recrystallization. The formation of coarse grains and twins in a BM is commonly caused by the heavy deformation by rolling to produce a 3-mm thick sheet and also incomplete dynamic recrystallization (Yao et al., 2020).

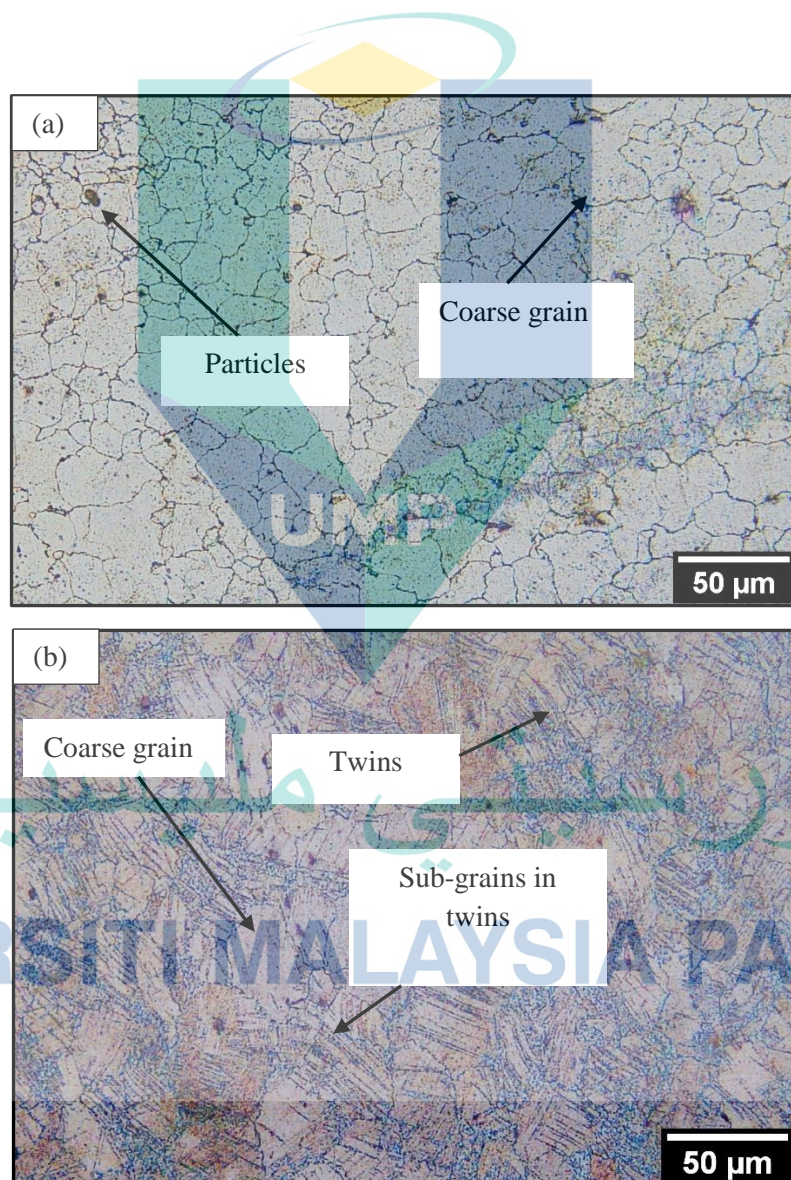


Figure 4.2 Microstructure of (BM); (a) AZ31, (b) AZ91 taken by optical microscopy.

## 4.2.1 Microstructure of FSW Sample Using Variation Rotational Speed

### 4.2.1.1 Rotational Speed of 1,200 rpm

Figure 4.3 shows the optical macrograph of the welded joint viewed at the cross-section of the weldment. The macrostructure of the weldment clearly revealed a demarcation line at the stir zone (SZ) as displayed in all welded samples of AZ31 and AZ91 alloys. The existence of the demarcation line comprised a series of alternating layers of AZ31 and AZ91 alloys in the interface is due to the discontinuity in material flow (Verma et al., 2017) and the absence of inter-diffusion of dissimilar Mg alloys (Savguira et al., 2018). There was a clear defined boundary between the AZ31 alloys placed at the retreating side (RS), which exhibited unclear structure compared to the AZ91 alloy at the advancing side (AS) after etching. The unclear grain structure obtained is due to the galvanic reaction between these alloys during etching.



Figure 4.3 Macrographs of FSW AZ31/AZ91 joint viewed at the cross section of sample 1,200 rotational speed.

The general microstructure of the alloys taken at the welded area was characterized using OM after etching with acetic-picral etchant. The joint consists of the stir zone (SZ), the thermomechanical heat-affected zone (TMAZ), and the heat-affected zone (HAZ). The welded sample revealed a mixture of homogeneous and inhomogeneous grain structure across the zone from the HAZ of AZ31 alloy towards the HAZ of AZ91 alloy when observed at higher magnification.

Figure 4.4(a) shows the optical micrograph of the HAZ of AZ31 alloy for the sample under welding parameters of rotational speed of 1,200 rpm and feed rate of 80 mm/min. This sample exhibited unclear grain structure on the RS of the AZ31 alloy.

Meanwhile, the AS shown in Figure 4.4(b) revealed bimodal grain structure with a mean grain size of 20  $\mu\text{m}$  (i.e., coarse grains) whereas the small grain structure has a mean grain size of 5  $\mu\text{m}$ . In general, the HAZ is located far away from the stirring tool and is expected to have the characteristic of a slightly coarser grain as no plastic deformation occurs but only heating exposure, which could induce grain growth.

Figure 4.4(c) displays the microstructure image at the SZ region, which showed a unique lamellae morphology and intermixing of unclear grains, as well as bimodal recrystallized grain structure (i.e., small and coarse grains) caused by the material being merged into the tool pin during the rotation of the pin and the shoulder. The SZ underwent an extreme level of plastic deformation and thermal exposure due to the direct contact with the pin during tool rotation. The recrystallization leads to grain refinement and simultaneously eliminates the  $\beta$ -phase by dissolving it into the Mg matrix (Jaiganesh et al., 2017). The measured mean grain size of the small grains at the SZ was approximately 10  $\mu\text{m}$  as measured by the ImageJ software.

Figure 4.4(d) shows the bimodal distribution of equiaxed small grain structure with the mean size of 10  $\mu\text{m}$  and coarse grain structure with the mean size of 20  $\mu\text{m}$  structure, which is likely expected from the recrystallization of the sample. Figure 4.4(e) shows that the TMAZ of AZ31 alloy at the RS revealed unclear grain after etching due to the galvanic effect between two dissimilar alloys. The bimodal distribution of equiaxed grain structure is likely expected due to the two opposite forces that act on the material, as this material is transferred forward and backward of the tool shoulder as the tool moves along the samples during FSW.

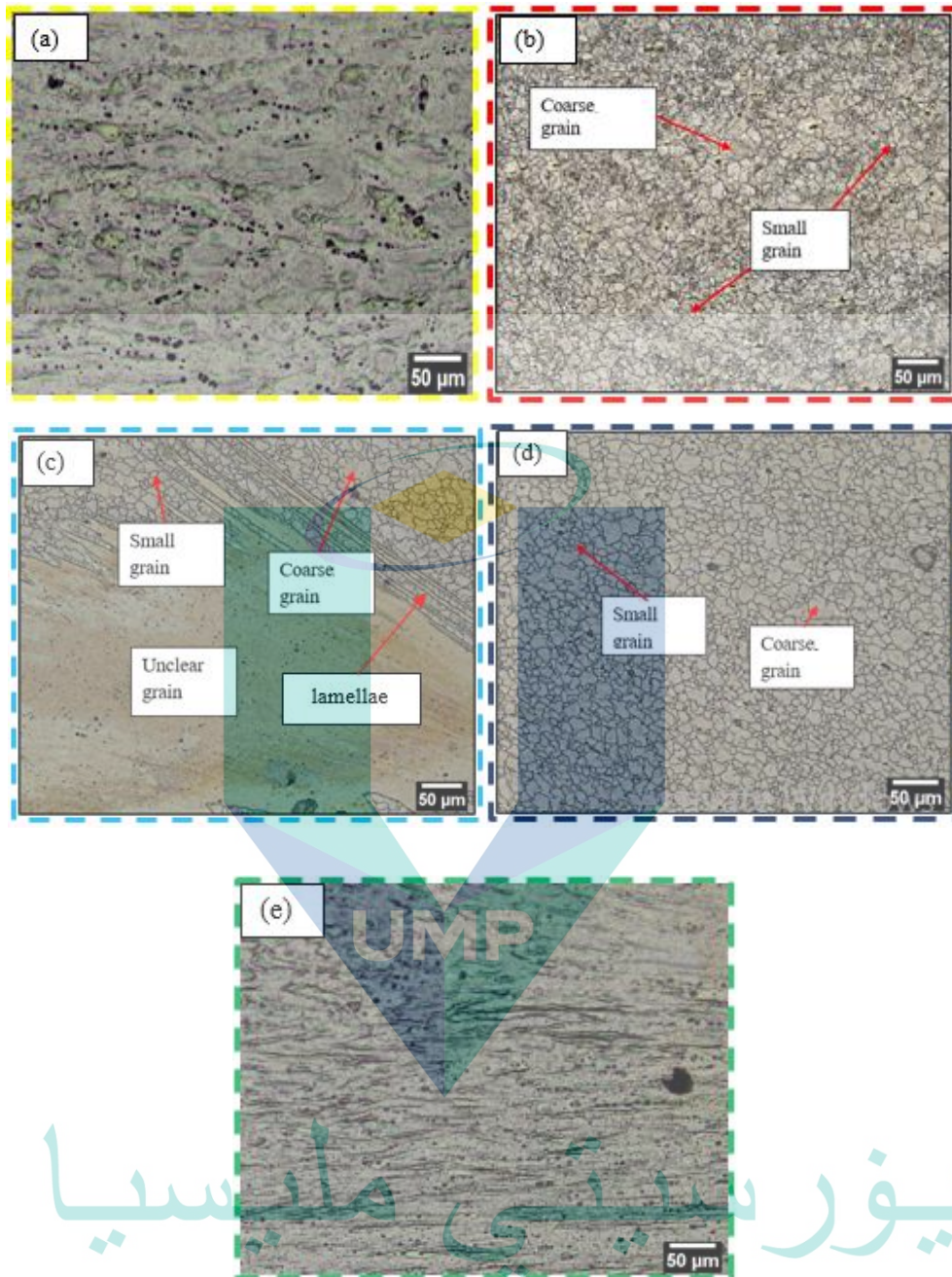


Figure 4.4 Micrographs of FSW AZ31/AZ91 joint viewed at the cross section of sample 1,200 rpm x 80 mm/min. (a) HAZ of RS, (b) HAZ of AS, (c) SZ, (d) TMAZ of AS, (e) TMAZ of RS.

#### 4.2.1.2 Rotational Speed of 1,000 rpm

Figure 4.5 reveals the macrograph of FSW joint viewed at the cross-section for the sample under the rotational speed of 1,000 rpm and feed rate of 60 mm/min. A similar microstructure was evidenced between the sample with the rotational speed of 1,200 rpm and 1,000 rpm. After etching, the microstructure of the welded joint exhibited unclear

grain structure at the RS due to the etching effect. The AZ91 welded samples have small, equiaxed, and homogenous grain structure across the zone. The captured image also revealed the demarcation line at the SZ region. The existence of the demarcation line is due to the discontinuity of the material flow during welding (Liu et al., 2018).

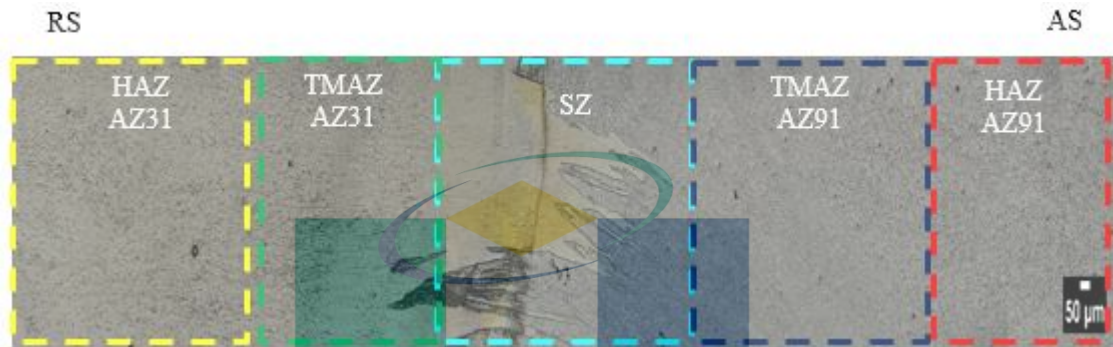


Figure 4.5 Macrograph of FSW AZ31/AZ91 joint viewed at the cross section at 1,000 rpm rotational speed.

Figure 4.6(a) presents a captured image of unclear grain structure of the AZ31 alloy at the HAZ. The unclear image of grain formed is due to the galvanic effect of both alloys during etching. The AS of AZ91 alloy in Figure 4.6(b) is characterized by bimodal grains with coarse grain size of approximately 40 μm and small grains with the mean size of 10 μm, very less twinning, and also unclear.

Similarly, the microstructure at the SZ also revealed lamellar morphology and bimodal grain structure (i.e., small and coarse grains). Figure 4.6(c) shows the SZ of the welded sample with coarse grain structure for the AZ91 alloy, and also unclear and small grain structure of the AZ31 alloy. The statistical analysis on the measured grains revealed a mean coarse grain size of approximately 20 μm whereas the small grains have a mean grain size of about 5 μm. The micrograph clearly revealed that large grains and the twinning present in the BM have transformed into grains smaller than the BM after welding due to the full dynamic recrystallization. Full dynamic recrystallization causes grain refinement and eliminates intermetallic compounds by dissolving the compounds into the magnesium matrix ( $\alpha$ ) (Verma et al., 2017).

Figure 4.6(d) shows the bimodal structure of fine (mean size = 3 μm) and coarse grains (mean size = 20 μm) at the TMAZ of the AS. Grain refining at this region mainly occurs due to the stirring action of the tool shoulder. Thus, there are fully recrystallized

refined grains and partially recrystallized coarse grains along the direction of stirring and following the grain size gradient. Insufficient heating temperature or strain dynamic recrystallization during welding causes an extraordinary microstructure in this region (Li et al., 2017). Figure 4.6(e) shows unclear grain structure at the RS resulting from the galvanic reaction during etching.

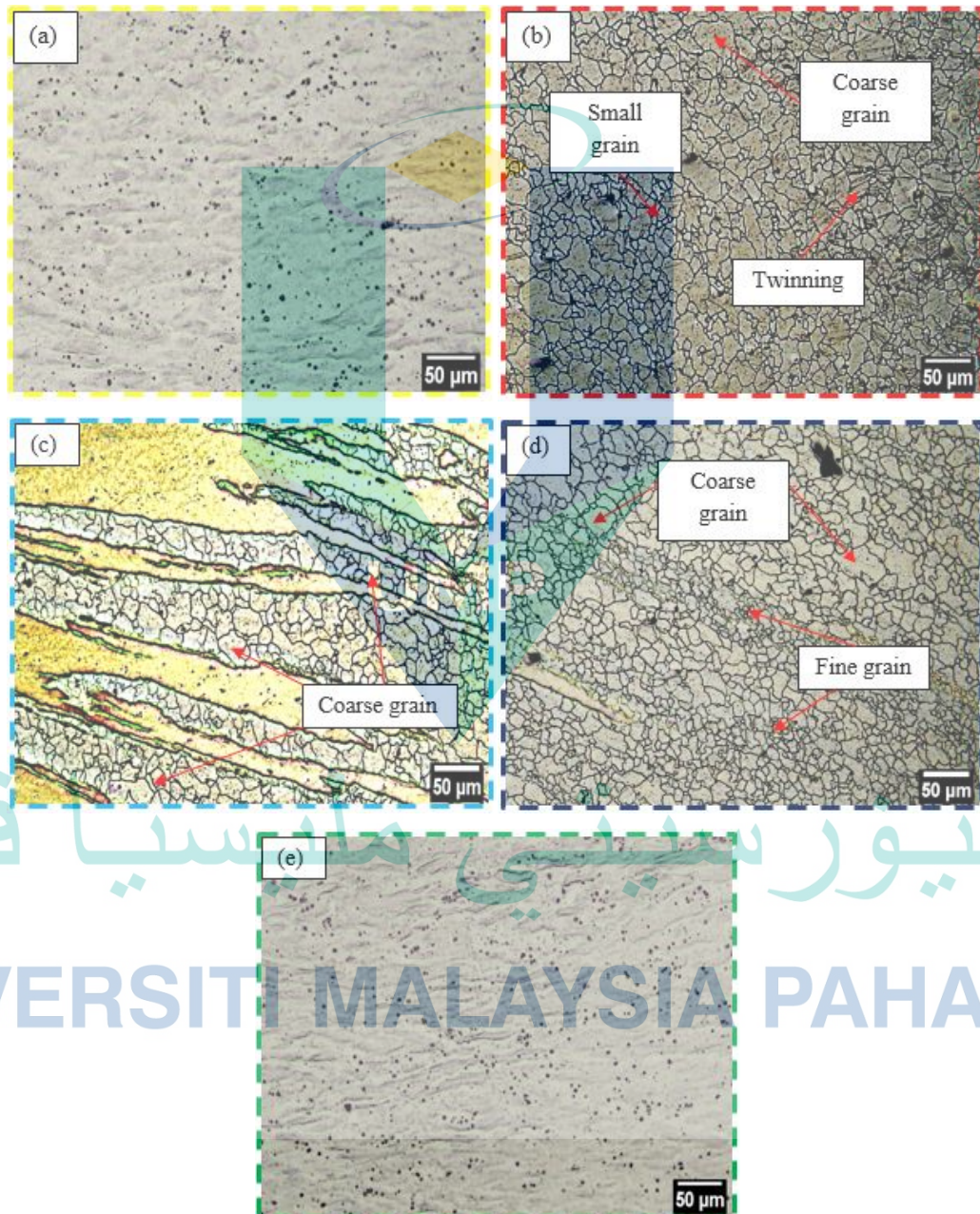


Figure 4.6 Micrographs of FSW AZ31/AZ91 joint viewed at the cross section of sample 1,000 rpm x 80 mm/min. (a) HAZ of RS, (b) HAZ of AS, (c) SZ, (d) TMAZ of AS, (e) TMAZ of RS

#### 4.2.1.3 Rotational Speed of 800 rpm

The typical microstructure of the etched sample under welding conditions of 800 rpm and 60 mm/min is shown in the optical micrograph image in Figure 4.7. The macrostructure of the sample indicates a mixture of unclear grains at the RS of AZ31 alloy and visible clear small grains at the AS. The grain intermixing at the SZ in lamellae morphology indicated the stirring action of the pin and the shoulder of the tool and the absence of inter-diffusion of dissimilar Mg alloys.

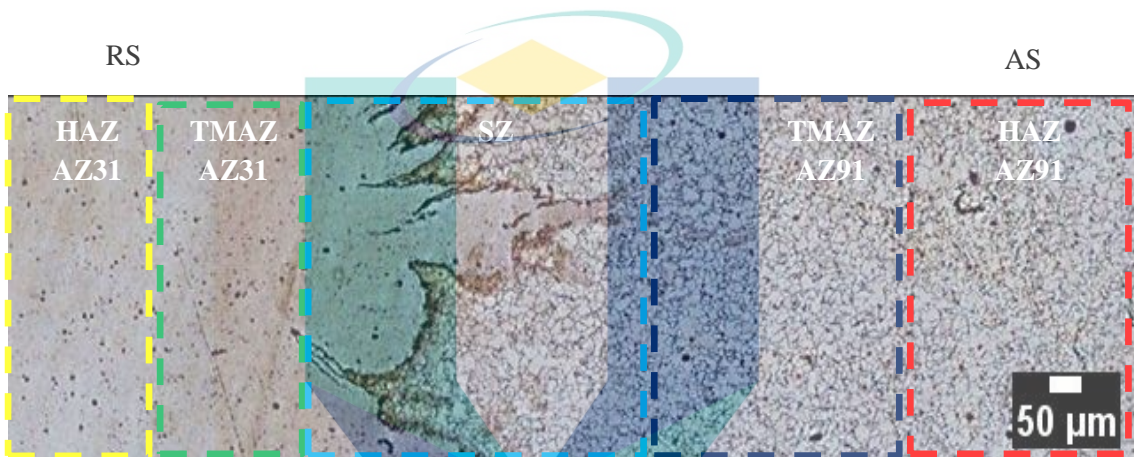


Figure 4.7 Macrograph of FSW AZ31/AZ91 joint viewed at the cross section at 800 rpm rotational speed.

The magnified image of the microstructure after etching under welding conditions of 800 rpm and 60 mm/min is presented in Figure 4.8. The bimodal grain structure at the SZ region in lamellae morphology indicated the stirring action of the pin and the shoulder of the tool.

Figure 4.8(a) reveals unclear microstructure of the HAZ at the RS with a distance far from the stirring of the pin. Figure 4.8(b) presents the bimodal grain structure of coarse grains (mean size = 40 μm) and small grains (mean size = 10 μm) at the AS. The unclear microstructure at the RS formed due to the galvanic effect of both alloys during etching.

Figure 4.8(c) indicates the SZ of the welded sample with the bimodal grain structure of coarse grains (mean size = 20 μm) and small grains (mean size = 5 μm), as well as full dynamic recrystallization due to the direct thermal exposure during stirring of the pin and the shoulder.



Figure 4.8(d) shows the TMAZ with unclear grain structure at the RS. Figure 4.8(e) indicates the bimodal grain structure at the AS of the TMAZ. There is a slight transition of grains from coarser to much smaller grain size with a clear image of grain boundaries. The grain micrograph did not reveal any twinning at this region. The mean coarse grain size at the AS is about 35  $\mu\text{m}$  whereas the mean size for small grains is 5  $\mu\text{m}$ . The TMAZ experienced plastic deformation due to sufficient heating and softening from the tool shoulder (Verma et al., 2017).

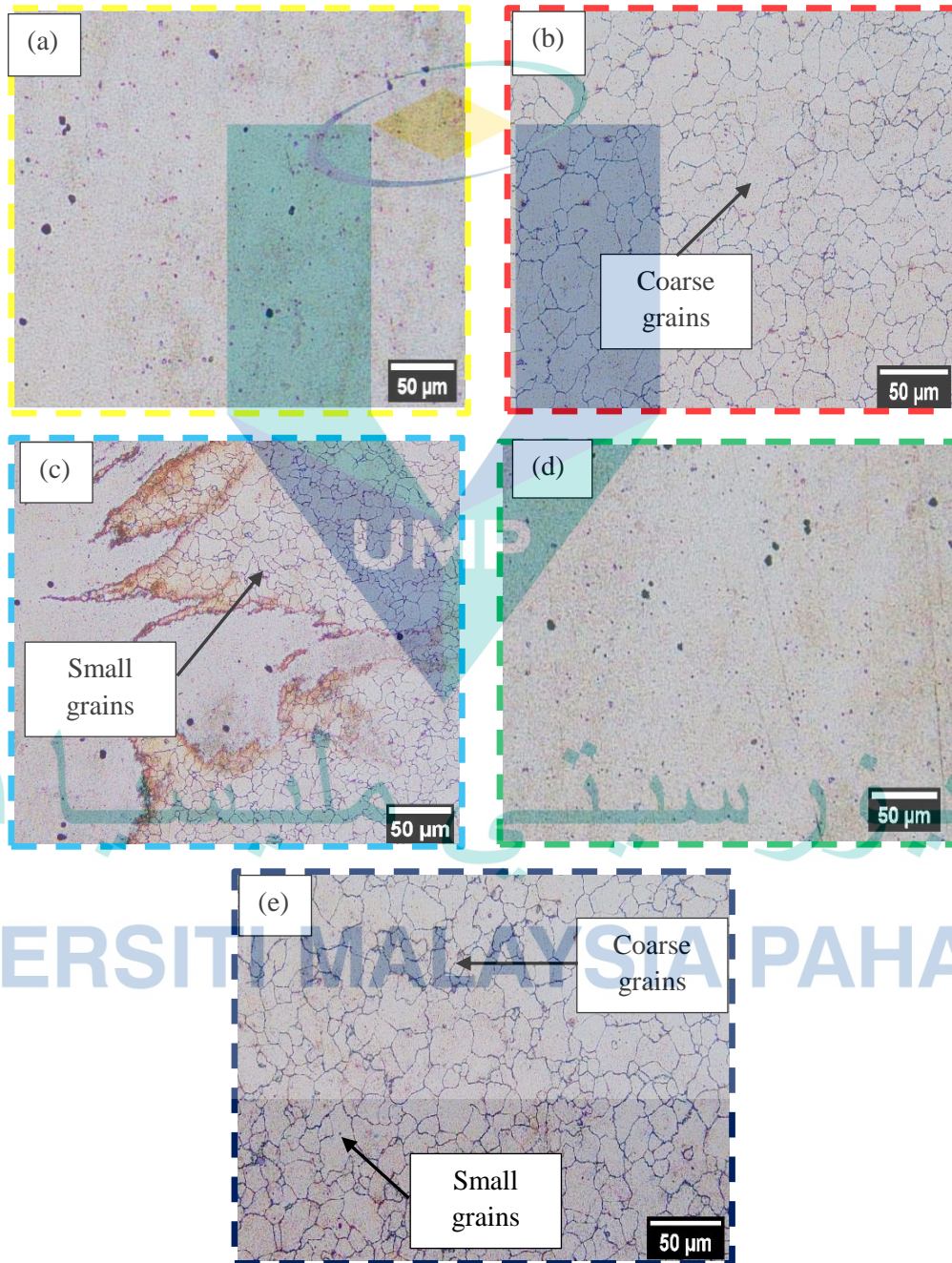


Figure 4.8 Micrographs of FSW AZ31/AZ91 joint viewed at the cross section of sample 800 rpm x 60 mm/min. (a) HAZ of RS, (b) HAZ of AS, (c) SZ, (d) TMAZ of RS, (e) TMAZ of AS.

#### 4.2.2 Intermetallic Particles Distribution

The intermetallic particles of the friction stir welded samples from the HAZ, TMAZ, and SZ were identified by the particles' brightness in SEM micrographs. EDX analysis reveals the composition of elements, such as aluminum (Al), zinc (Zn), manganese (Mn), and oxygen (O<sub>2</sub>). Particle distribution is particularly important as the parameter can be a factor contributing to the corrosion of alloys. The sample subjected to 1,000 rpm of rotational speed and 60 mm/min of feed rate was selected for intermetallic particle identification using SEM and EDX.

Figure 4.9 shows the SEM micrograph and mapping analysis of particle morphology observed at the SZ of the welded sample and from the analysis, it is believed that Al<sub>8</sub>Mn<sub>5</sub> particles are present in the alloys. The particles are randomly distributed on the matrix in polygonal shapes with 8.80 wt. % of Mn present and Al composition of 13.10 wt. % as analyzed using EDX (Figure 4.10). The size of the particle is about 4 μm based on Feret diameter.

Figure 4.11 reveals the SEM micrograph and mapping of the particle distribution at the HAZ of the welded alloys. The captured image in this region also proved the distribution of Al<sub>8</sub>Mn<sub>5</sub> particles. The EDX analysis in Figure 4.12 shows the evidence of element composition, thus conforming the existence of the particles. The presence of Al (15.41 wt. %) and Mn (2.41 wt. %) formed Al<sub>8</sub>Mn<sub>5</sub> at this region.

Figure 4.13 indicates the SEM micrograph and mapping analysis of the TMAZ region. The intermetallic particles formed on the matrix was Al<sub>8</sub>Mn<sub>5</sub>. The EDX point scanning on the particles shown in Figure 4.14 also confirms the presence of Al and Mn and suggested the presence of Al<sub>8</sub>Mn<sub>5</sub> at this region. The percentage of Al (25.23 wt. %) and Mn (14.73 wt. %) formed Al<sub>8</sub>Mn<sub>5</sub>. In conclusion, the distribution of Al-Mn particles decreased from the TMAZ towards the SZ, which is attributed to the pinning effect during FSW.

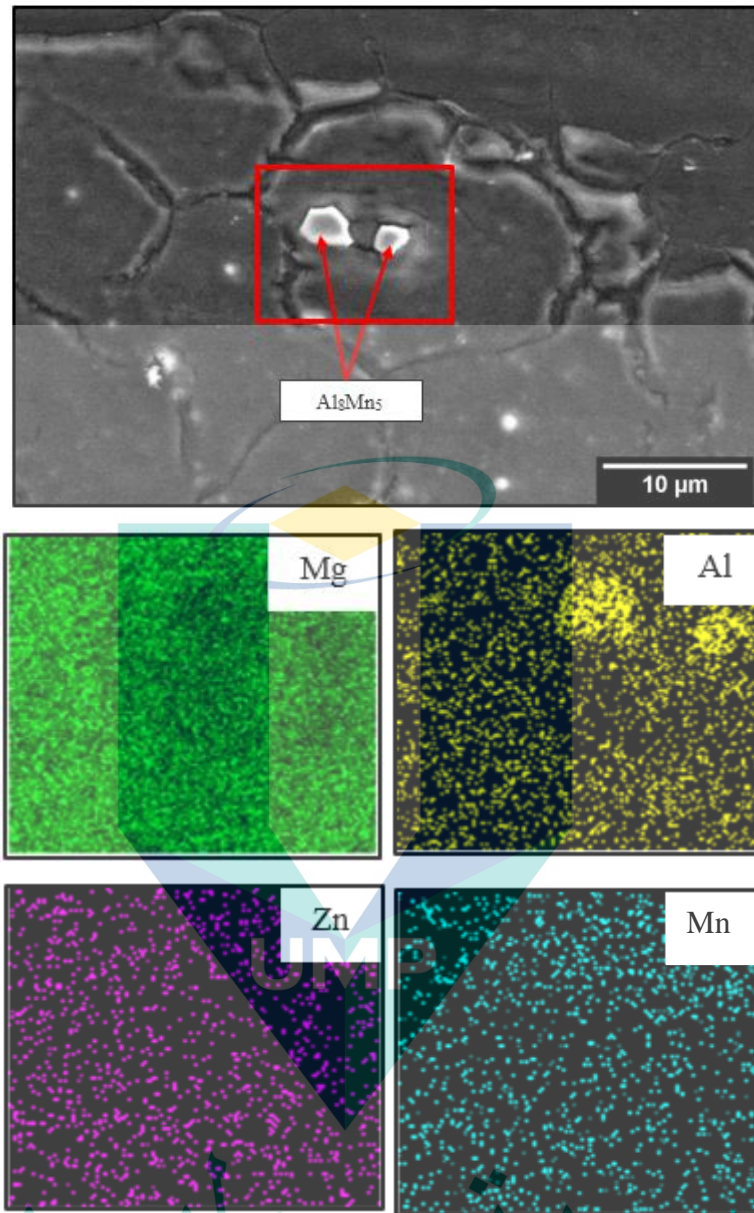


Figure 4.9 SEM micrograph of SZ region with EDX mapping analysis on the  $\alpha$ -Mg matrix and the particles.

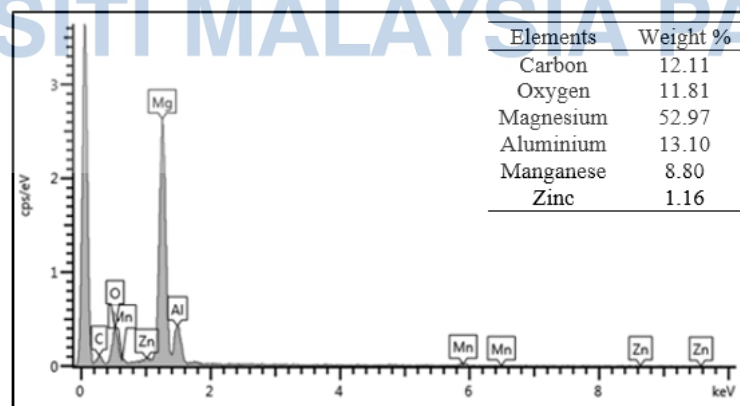


Figure 4.10 EDX spectrum of SZ mapping.

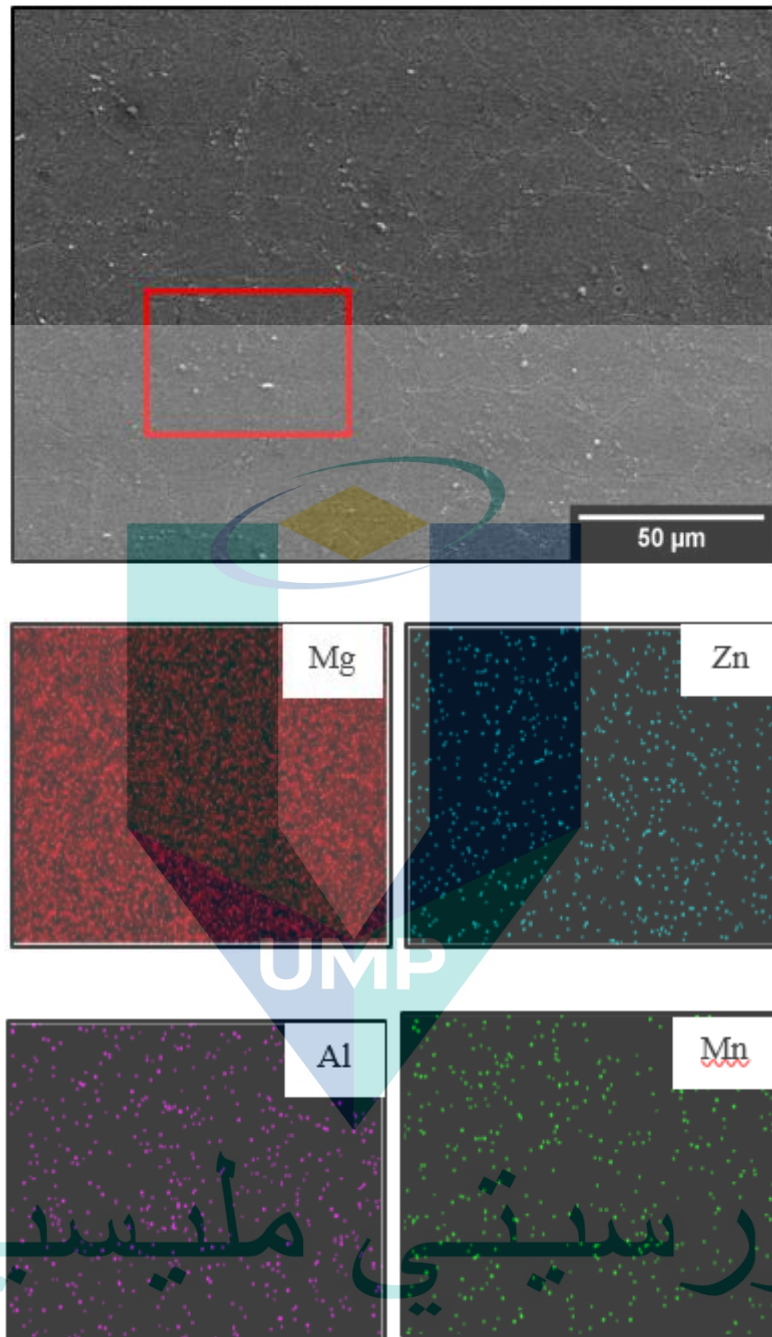


Figure 4.11 SEM micrograph of HAZ region with EDX mapping analysis

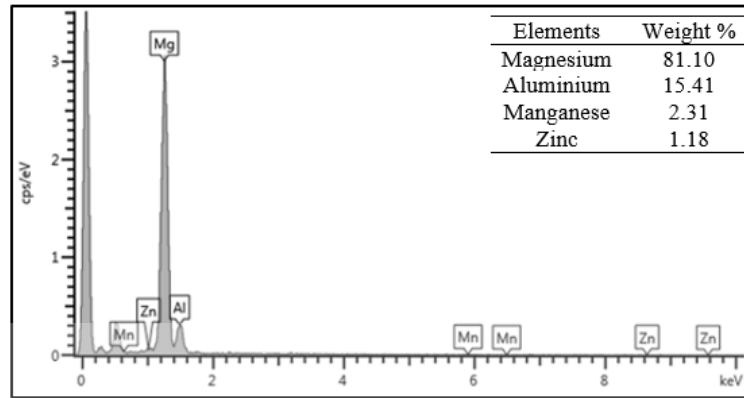


Figure 4.12 EDX spectrum of HAZ mapping.

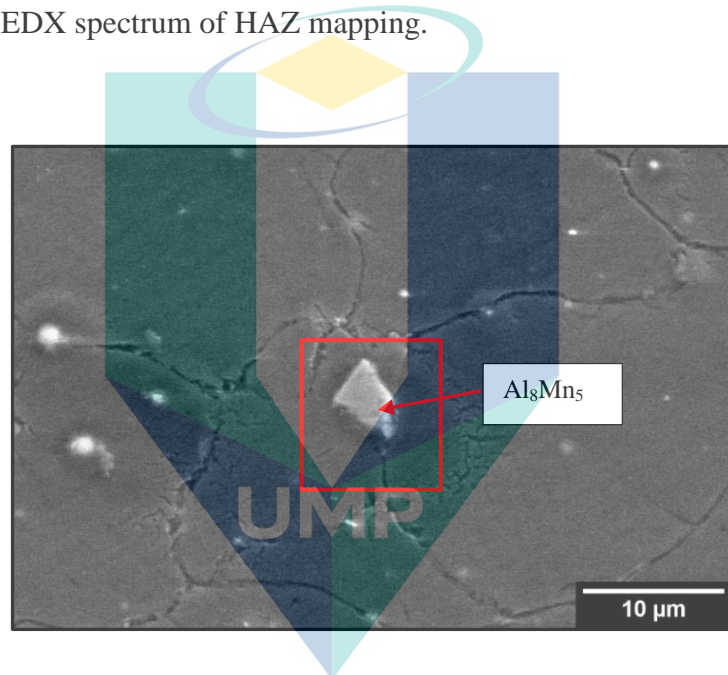


Figure 4.13 SEM micrograph of TMAZ region with EDX point analysis on the particles.

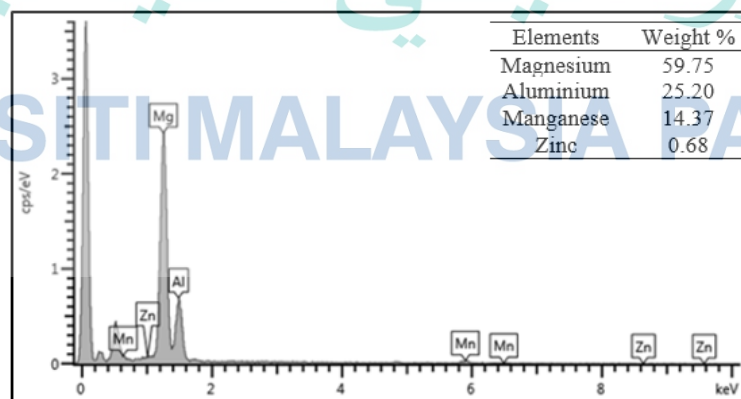


Figure 4.14 EDX point spectrum of the particle found at TMAZ.

### 4.2.3 Microhardness

Vickers hardness distribution across the joint center is measured across the welding direction. Figure 4.15 shows the micro-hardness profile obtained by measuring from the AZ31 to AZ91 BM of the joint welded at the feed rates of 60, 80, and 100, and rotational speeds of 800, 1,000, and 1,200 rpm. Within the welded sample as shown in Figures 4.15(a)–(c), the hardness increased from the AZ31 BM across the SZ to the AZ91 BM. The range of hardness value of the AZ31 BM was 50 to 70 Hv for all samples whereas the range of hardness value of the AZ91 BM was 80 to 100 Hv. The range of hardness value at the HAZ of the RS was 55 to 70 Hv. The hardness value started to increase at the TMAZ of the RS from 60 to 90 Hv. The hardness of the welded area is significantly related to the changes of microstructure due to frictional heat during welding.

All samples showed relatively similar trends by increasing the hardness value from the AZ31 BM to the AZ91 BM across the welding zone. This trend corresponds to the difference in grain size by the variation of rotational speed and feed rate. The HAZ region with lower micro-hardness value was observed close to the HAZ/AZ31 BM boundaries. The micro-hardness value increased gradually towards the SZ region. This is consistent with the dynamic recrystallization of the grain structure affected by the thermal cycle during FSW. As the distance from the SZ region increased, the heat input decreased and insufficient to induce the occurrence of recrystallization, thus the micro-hardness value was close to the BM.

The micro-hardness for the TMAZ for both alloys also depends on the plastic deformation and heat flow during FSW. The local plastic deformation induced the recrystallization of grain structure and improved micro-hardness due to the increase in dislocation density and thermal diffusion at the TMAZ, which led to dislocation motion and material softening (Yao et al., 2020).

The SZ region exhibited higher micro-hardness value of 70 HV to 100 HV relative to the AZ31 BM because the material underwent an extreme level of plastic deformation and thermal exposure due to the direct contact with the pin during tool rotation that induced dynamic recrystallization produced by FSW. The highest micro-hardness occurred at this region due to the direct stirring and compressive deformation to form recrystallized slightly smaller grains than other regions. The Hall-Petch relationship

stated that the hardness of a material is directly proportional to the grain size (Pan et al., 2016). The Hall-Petch relationship can be written as  $Hv = 40 + 72d^{-1/2}$ , where  $d$  indicates the grain size. A small-grained material has a greater total grain boundary area to inhibit the dislocation motion (Chen et al., 2012).

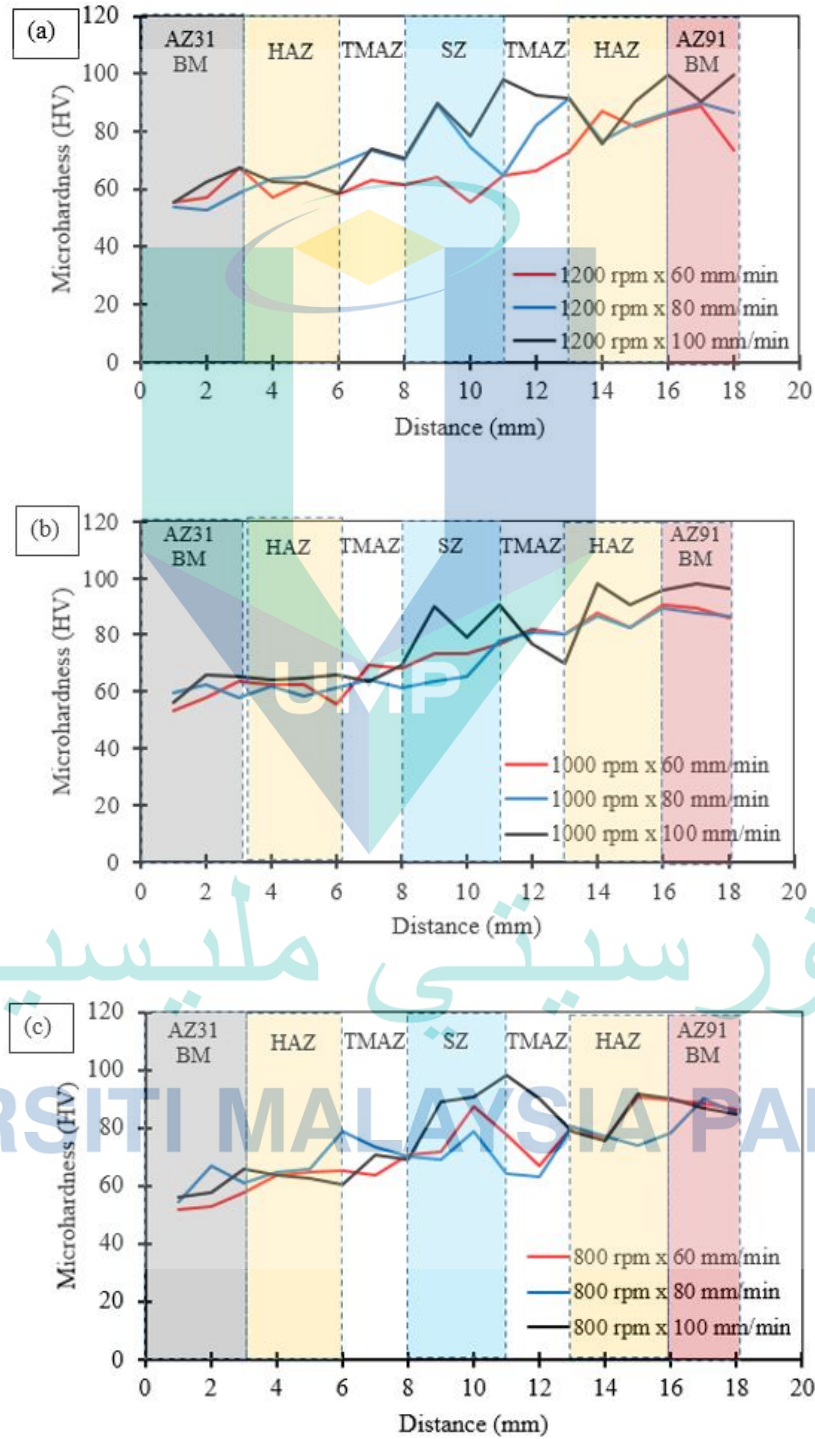


Figure 4.15 Hardness distribution of welded Mg alloy using rotational speed of: (a) 1,200 rpm, (b) 1,000 rpm, and (c) 800 rpm.

### 4.3 Corrosion Performance of Welded AZ31/AZ91 Alloys

#### 4.3.1 Corrosion Behaviour During Hydrogen Evolution Measurement

Hydrogen evolution experiment is one of the methods used to determine the corrosion rate of Mg alloys (Bender et al., 2007). The change of H<sub>2</sub> gas volume is equal to the H<sub>2</sub> evolution rate. A burette was used to record the reduction of solution volume that corresponds to the H<sub>2</sub> gas evolution rate of the samples immersed in 3.5 wt. % of sodium chloride (NaCl) solution for 6 days. Equation 4.1 and Equation 4.2 display the corrosion mechanism involved during H<sub>2</sub> evolution test (Bender et al., 2007). The anodic reaction explains Mg dissolution and the cathodic reaction shows the evidence of H<sub>2</sub> gas evolution.

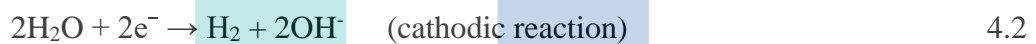
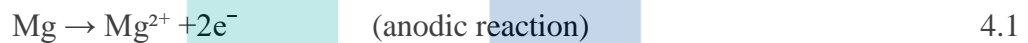


Figure 4.16 reveals the H<sub>2</sub> evolution curve for 1,200 rpm of rotational speed. From the curve, the H<sub>2</sub> evolution rate of 80 mm/min was 34 ml/cm<sup>2</sup>, which is an approximately similar trend with the sample welded at 100 mm/min of feed rate. The sample with 60 mm/min of feed rate showed a very high H<sub>2</sub> evolution rate (i.e., about 52 ml/cm<sup>2</sup>) since day 1 to over 6 days of immersion.

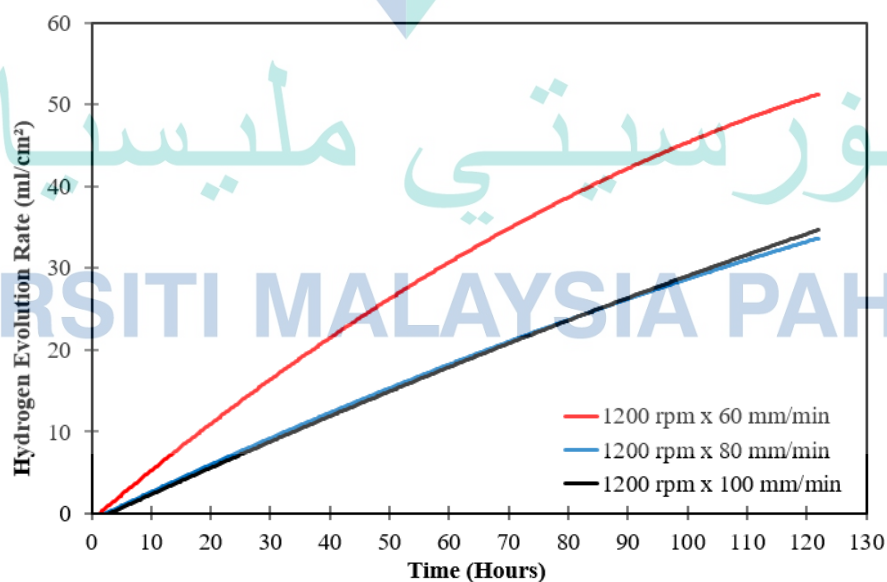


Figure 4.16 Hydrogen evolution rate of welded Mg alloy over 6 days immersion at 1,200 rpm rotational speed.



Figure 4.17 shows the H<sub>2</sub> evolution curves for rotational speed of 1,000 rpm. From the curve of the sample for the rotational speed of 1,000 rpm and feed rate of 60 mm/min, a high H<sub>2</sub> evolution rate of 52 ml/cm<sup>2</sup> was recorded compared to the H<sub>2</sub> evolution rates of the samples subjected to feed rate of 80 mm/min (i.e., 43 ml/cm<sup>2</sup>) and 100 mm/min (i.e., 41 ml/cm<sup>2</sup>). The least H<sub>2</sub> evolution rate from the feed rate of 100 mm/min indicated the lowest corrosion rate among them.

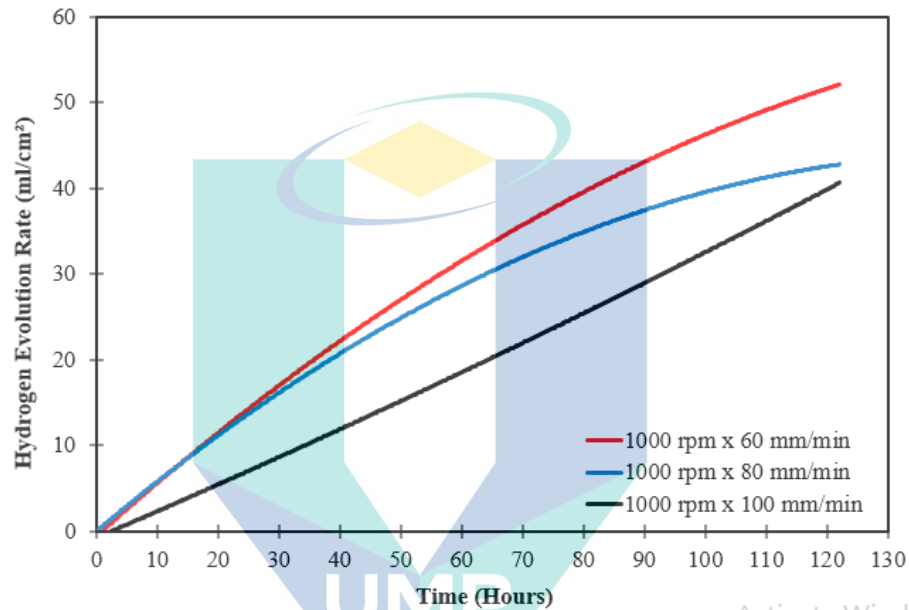


Figure 4.17 Hydrogen evolution rate of welded Mg alloy over 6 days immersion at 1,000 rpm rotational speed.

Figure 4.18 shows the H<sub>2</sub> evolution curves of the welded Mg alloys immersed in 3.5 wt. % of NaCl solution for 6 days. From the curves, the three samples welded at the rotational speed of 800 rpm, the sample subjected to 80 mm/min of feed rate has a high H<sub>2</sub> evolution rate over 6 days, followed by the samples subjected to the feed rates of 60 and 100 mm/min. The H<sub>2</sub> evolution rates of the samples welded at the feed rates of 60, 80, and 100 mm/min were 35, 41, and 34 ml/cm<sup>2</sup>, respectively. The H<sub>2</sub> evolution rate is directly proportional to the corrosion rate. The feed rate of 100 mm/min indicates good corrosion resistance since day 1 to the following 6 days of immersion compared to other samples. In conclusion, the sample welded with the rotational speed of 800 rpm indicates less H<sub>2</sub> evolution rate than other samples welded at rotational speeds of 1,000 and 1,200 rpm.

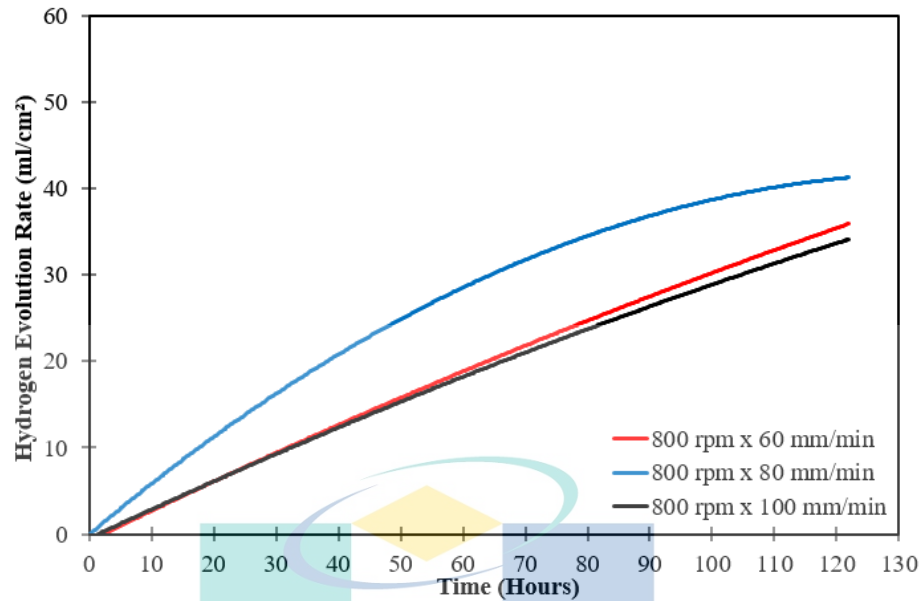


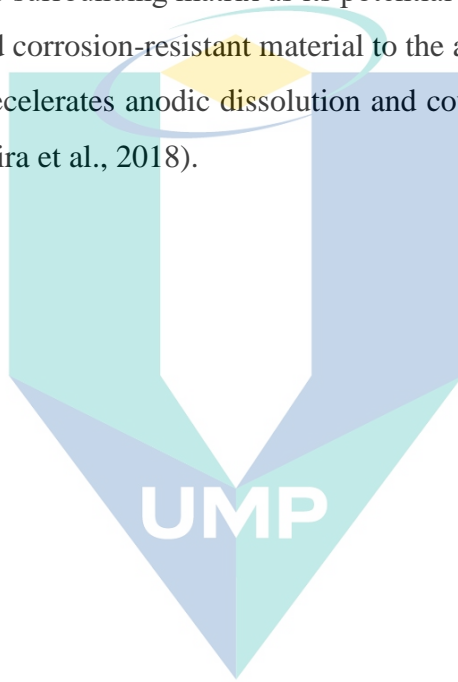
Figure 4.18 Hydrogen evolution rate of welded Mg alloy over 6 days immersion at 800 rpm rotational speed.

A series of in-situ images captured at various times during the exposure period for the welded samples are provided in Figure 4.19. The corrosion behavior of the welded Mg samples indicated two main stages of corrosion attack: filiform-like corrosion and the growth of thick corrosion product. The  $H_2$  evolve rate initially at the BM was observed at day 1, and accompanied by the appearance of black spots. It is also evidenced by the presence of small  $H_2$  bubbles. There was not much difference for the sample appearance on the first day.

On day 2 of immersion, the number of  $H_2$  bubbles on the samples increased. At this time, the filiform-like corrosion with black in color characterized by the thread-like characteristic started to form at the SZ region. The bubbles were still present on the welded samples and appeared at several spots near to the AZ91 BM and at the AZ31 side. After 4 days of immersion, the filiform corrosion continued to spread on the AZ31 side and covered most of the area. Only a few  $H_2$  bubbles remained on the AZ31 MB, near to the filiform sites and at the welded surface. The welded surface of AZ31/AZ91 alloys also exhibited the filiform corrosion with  $H_2$  bubbles present near the corroding sites. On the AZ91 BM, the filiform corrosion spread less with the corrosion on the AZ31 alloy propagated vertically whereas the corrosion for the AZ91 alloy propagated horizontally. A whitish corrosion product formed on the alloys, which acts to partially protect the

samples' surface. Some of the corrosion product was also found on the funnel and the surrounding area, and consequently caused the solution to become cloudy.

After 6 days of immersion, no H<sub>2</sub> bubbles were virtually observed on the AZ31 alloy and its surface; however, H<sub>2</sub> gas continued to evolve. The effect of dissimilar coupling was clearly visible where the weldment region did not have much dissolution compared to the BM. The presence of Al<sub>8</sub>Mn<sub>5</sub> particles can reduce the corrosion of the welded alloys during immersion in chloride ion solution. These particles are found to be more cathodic than the surrounding matrix as its potential is higher than the matrix or  $\alpha$ -Mg. Mn acts as a good corrosion-resistant material to the alloy. The presence of Al<sub>8</sub>Mn<sub>5</sub> as discussed earlier decelerates anodic dissolution and could reduce the corrosion rates of the samples (Savguira et al., 2018).



اونيورسيتي ملايسيا قهغ

UNIVERSITI MALAYSIA PAHANG

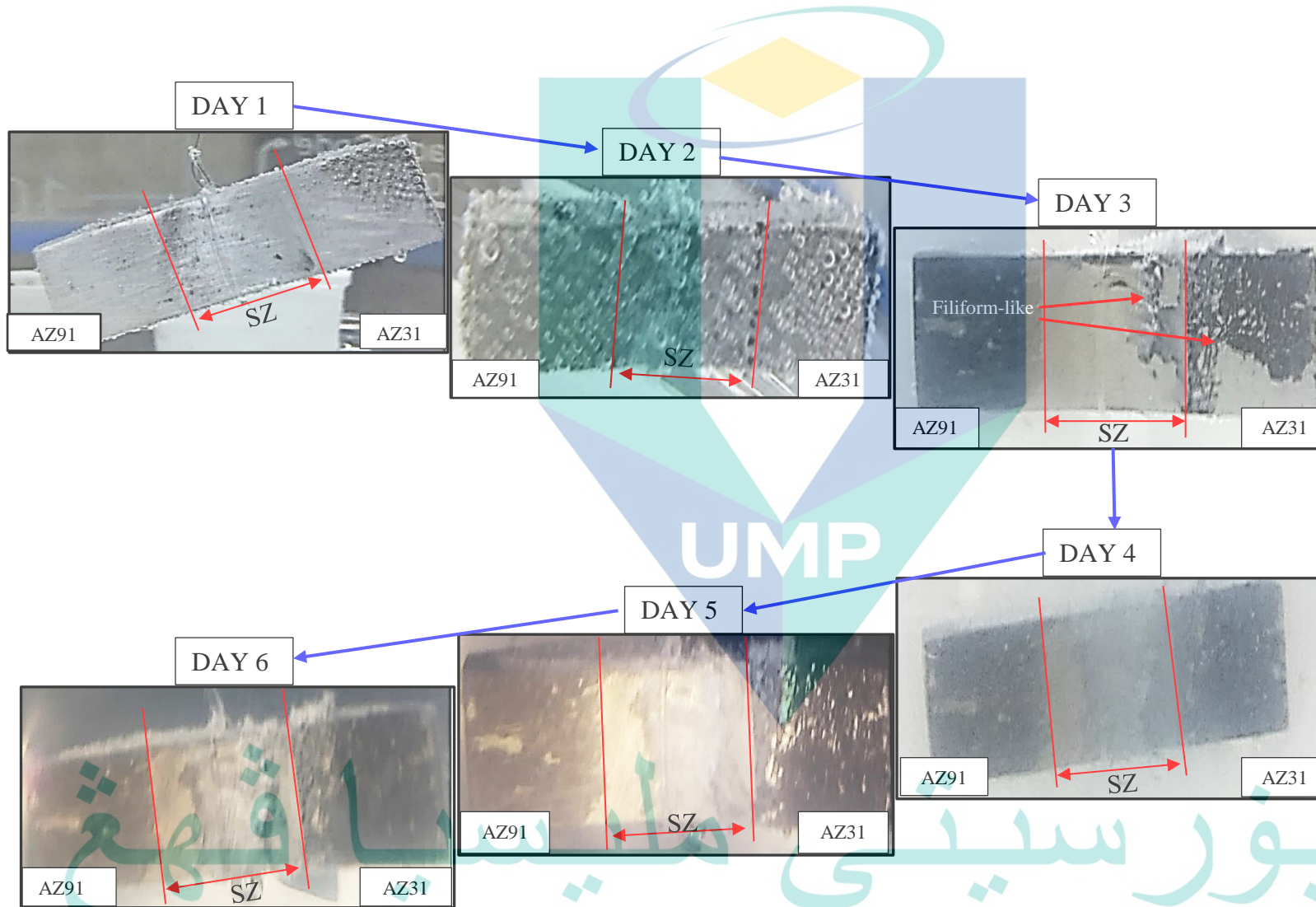


Figure 4.19 In-situ images of welded samples immersed in 3.5 wt.% NaCl during hydrogen evolution test for over 6 days.

The corrosion rate determined from weight loss measurement is displayed in Table 4.1. The corrosion rate based on weight loss calculation fits with the H<sub>2</sub> evolution rate. From the measurement, the welding condition of 1,000 rpm of rotational speed demonstrated the highest corrosion rate of 9.61 mm/y with the feed rate of 60 mm/min, followed by the feed rates of 80 mm/min (corrosion rate = 6.11 mm/y) and 100 mm/min (corrosion rate = 5.98 mm/y). The corrosion rate was lower at higher rotational speed of 1,200 rpm and feed rate of 100 mm/min, with the corrosion rate of 3.46 mm/y, followed by the feed rate of 80 mm/min ( corrosion rate = 3.84 mm/y). The corrosion rate for the sample with rotational speed of 800 rpm and feed rates of 100 mm/min and 60 mm/min was slightly higher than the sample welded at 1,200 rpm.

Based on the H<sub>2</sub> evolution test, the most corroded alloy was observed for the sample with the welding condition of 1,000 rpm, followed by 800 rpm, and the lowest corrosion rate occurred at 1,200 rpm. In relation to the microstructure of the sample, the variation of grain size and grain structure are expected to influence the corrosion rate. The presence of  $\beta$ -phase can possibly act as the corrosion wall and caused higher corrosion resistance (Cao et al., 2016). Thus, the absence of the  $\beta$ -phase can cause high Mg dissolution due to the non-existence of a corrosion barrier.

Table 4.1 Corrosion rate values of welded Mg alloys immersed in 3.5 wt.% NaCl for 6 days.

Rotational speed x feed rate ( rpm x mm/min )	Corrosion rate from weight loss (mm/y)
1,200 x 60	6.45
1,200 x 80	3.84
1,200 x 100	3.46
1,000 x 60	9.61
1,000 x 80	6.11
1,000 x 100	5.98
800 x 60	4.48
800 x 80	6.11
800 x 100	4.06

### 4.3.2 Corrosion Morphology After Corrosion Product Removal

There are two stages of corrosion attack on the welded Mg alloys during immersion test, namely filiform-like corrosion and the accumulation of corrosion product. The accumulation of thick corrosion product formed on the samples' surface is displayed in Figure 4.20. The hydroxide layer formed in the chloride solution containing impurities caused the dissolution of noble elements on the surface of the alloys (Zeng et al., 2009). These impurities are suggested to be the cause for the accelerated dissolution of Mg and its alloys (Savguira et al., 2018). In AZ31 alloy, the oxide formed on the  $\alpha$ -phase offers poor corrosion resistance, allowing the anodic reaction to take place vigorously.

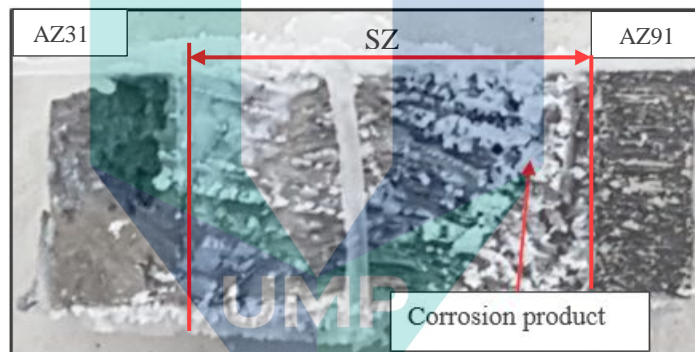


Figure 4.20 Optical image of corroded sample during hydrogen evolution test.

The SEM images of corrosion morphology of the AZ31 BM are shown in Figure 4.21. The removal of the corrosion product clearly revealed filamental appearance on the surface. Intense filiform corrosion attack was observed on the surface of the AZ31 BM compared to the AZ91 BM (Figure 4.22). However, the AZ31 BM indicated corrosion attack with undermined grain pits propagated to become filiform-like tunneling on the alloy and penetrated the surface. The corrosion morphology of the welded samples after the removal of corrosion product is displayed in Figures 4.23. Figure 4.24 reveals cracks propagates through the welded zone.

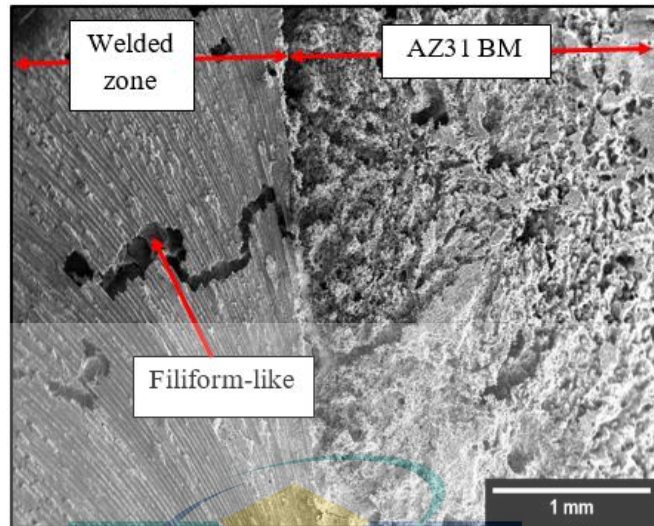


Figure 4.21 SEM micrograph of corroded samples after corrosion product cleaning on of AZ31.

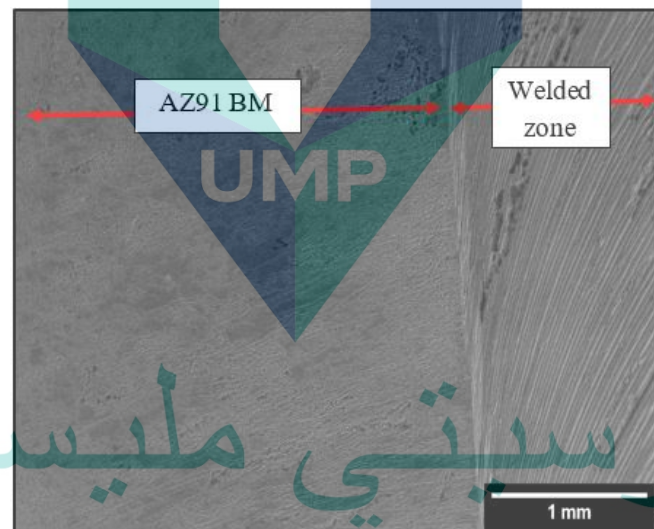


Figure 4.22 SEM micrograph of corroded samples after corrosion product cleaning on of AZ91.

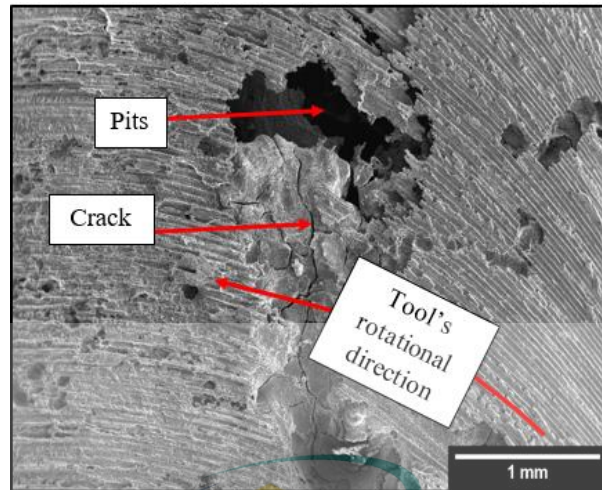


Figure 4.23 SEM micrograph of corroded samples after corrosion product cleaning at welded zone.

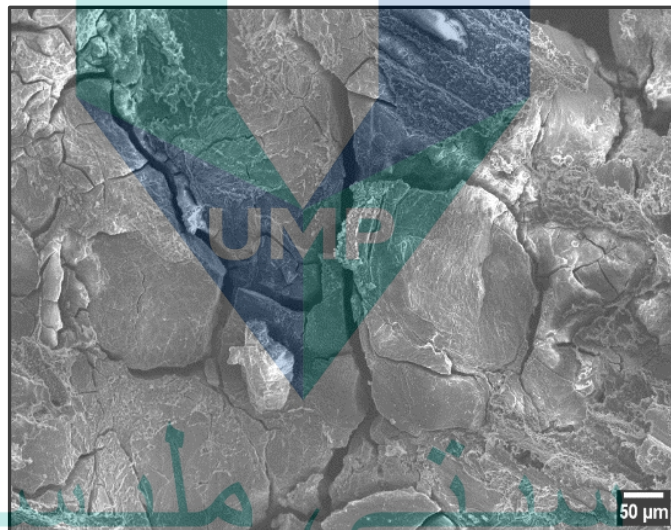


Figure 4.24 SEM micrograph of sample showing crack after corrosion product cleaned immersed for hydrogen evolution experiment.

# UNIVERSITI MALAYSIA PAHANG

## 4.4 Electrochemical Characteristic of Welded AZ31/AZ91 Alloys

In this section, the results from the investigation on corrosion behavior and performance of welded Mg alloys of AZ31 and AZ91 are presented to explain the corrosion initiation, propagation, and corrosion product formation. The measurement of open circuit potential (OCP), cathodic, and anodic polarization behavior is supported with the optical images taken.



#### 4.4.1 Open Circuit Potential (OCP)

The OCP measurement of the welded samples was conducted in 3.5 wt. % of NaCl solution for the duration of 5 min. The samples were prepared by mechanically ground with a 2,500 grit abrasive paper and coated with lacquer with the exposure area of 3 cm<sup>2</sup>. A saturated calomel electrode was used as the reference electrode and a camera was used to capture images throughout the measurement. Figure 4.25 presents the OCP-time plot of the welded samples for the rotational speed of 800 rpm and feed rates of 60, 80, and 100 mm/min. The welded sample under the feed rate of 60 mm/min revealed a stable, high corrosion potential at around -1.58 V and was more electropositive than the samples at 80 and 100 mm/min.

The welded sample produced with the feed rate of 100 mm/min indicated a change to more electronegative potential from -1.586 to -1.590 V, while the sample produced at 80 mm/min exhibited a change to more positive values (i.e., approximately 20 mV) from -1.624 to -1.608 V after 180 s of immersion. All the samples corroded during the OCP measurement and the sample at the feed rate of 60 mm/min displayed more electropositive potential than other samples. The corrosion propagation state causes the stability and potential shift during the OCP measurement due to the propagation of the filament in different directions and contributed to more corrosion attack or filament penetration (Savguira et al., 2018; Yao et al., 2020).

The changes of OCP observed is related to the microstructure in different regions, which implies different driving forces of corrosion (Yao et al., 2020). The difference in the phase constituent between the two alloys is attributed to the greater Al content in the AZ91 than AZ31 alloys. The presence of Al<sub>8</sub>Mn<sub>5</sub> particles in the welded alloys reduced the corrosion of the alloys in the chloride solution, causing the alloys to be much more stable during the immersion (Song et al., 2014). The captured images of the sample produced at the feed rate of 60 mm/min during the OCP measurement are displayed in Figure 4.26, which indicated corrosion initiation (i.e., 1 min) due to the presence of small H<sub>2</sub> bubbles on the surface. The corrosion grew and propagated with visible black spots indicating corrosion attack and H<sub>2</sub> gas evolved at the corroding black spots after 5 min of immersion time.

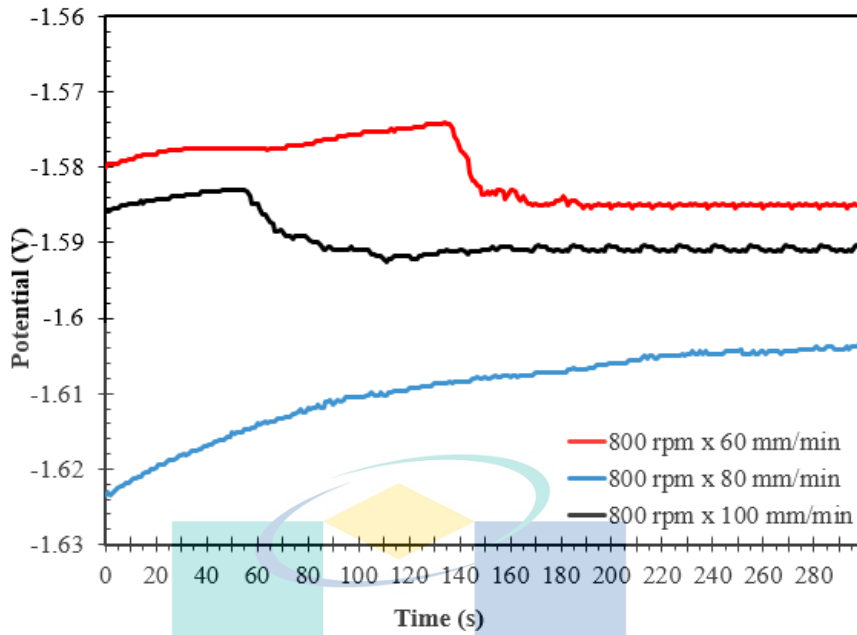


Figure 4.25 Open circuit potential (OCP) vs time curves for 800 rpm rotational speed.

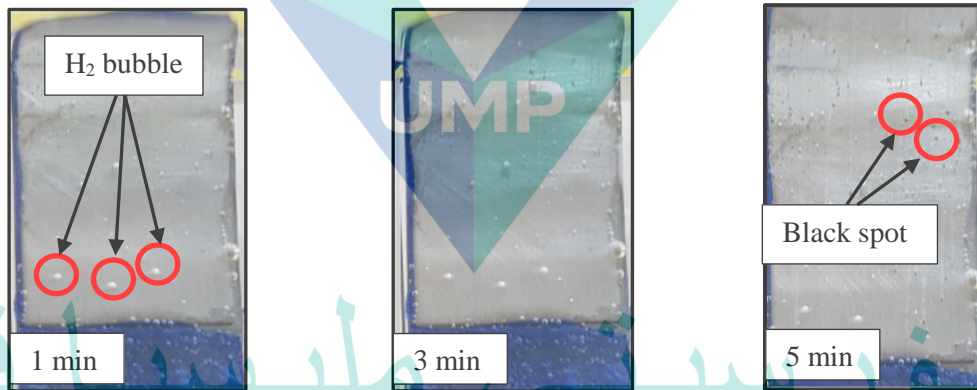


Figure 4.26 Optical image of welded alloy during OCP for 5 minute.

The OCP-time curves of the welded samples under welding parameters of rotational speed of 1,000 rpm and feed rates of 60, 80, and 100 mm/min are displayed in Figure 4.27. From the curves, the overall potentials of the welded samples are found in the range of -1.62 to -1.58 V. The welded samples at the feed rates of 60 and 80 mm/min indicated a stable potential of -1.60 V after 115 s of immersion where for the feed rate of 100 mm/min, the sample took 200 s to shift from -1.592 to -1.58 V and stabilized after 200 s of immersion.

All the samples corroded during the OCP measurement, indicating a stable potential that is more electropositive than the standard potential of Mg alloys (i.e., -1.67 V). The stability and more positive potential can be attributed by the formation of protective and temporary MgO passive layer over the surface. The instability of the potential shift during the OCP measurement is expected due to the breakage of the protective film and development of pitting corrosion, thus produced black spots on the samples (Singh et al., 2015). It is suggested that the variation of grain structure in different welding zones and the presence of second-phase particles of  $Al_8Mn_5$  as mentioned previously are expected to influence the stability of OCP measurement. The corrosion initiated with the formation of small black spots composed of Mg hydroxide ( $Mg(OH)_2$ ). The  $H_2$  gas evolved at the black spots accomplished the cathodic reaction and Mg dissolution occurred simultaneously as the anodic reaction.

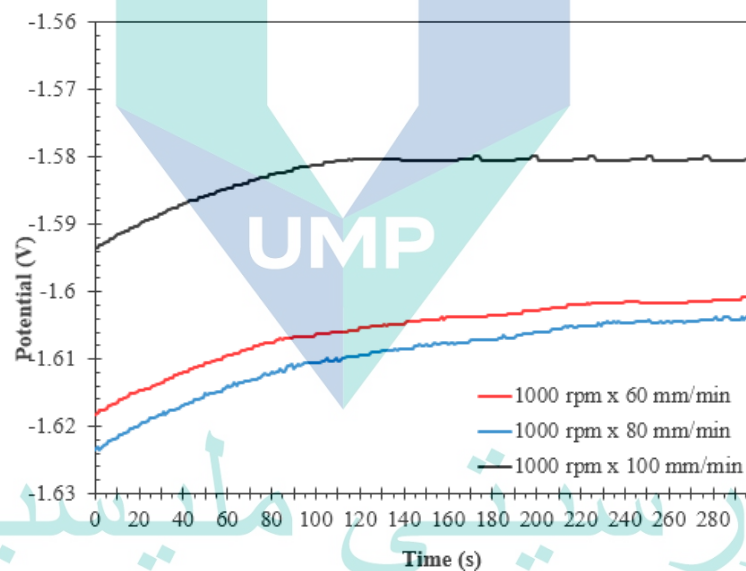


Figure 4.27 Open circuit potential (OCP) vs time curves for 1,000 rpm rotational speed.

Figure 4.28 shows the OCP-time curve of welded Mg alloys under the rotational speed of 1,200 rpm and feed rates of 60, 80, and 100 mm/min immersed in 3.5 wt. % of NaCl solution for 5 min. From the OCP-time curve, the overall potential of the welded samples are found in the range from -1.618 to -1.58 V. The feed rate of 60 mm/min revealed a stable potential at -1.596 V after 80 s of immersion, whereas a stable potential of -1.58 V was observed for the feed rate of 100 mm/min and a stable potential of -1.59

V at the feed rate of 80 mm/min, which subsequently decreased to more electronegative values in relation with the increase of corrosion area and the occurrence of corrosion.

The potential instability of the samples is caused by the variation of grain structure and the presence of  $Al_8Mn_5$ . The distribution and size of  $Al_8Mn_5$  cause a change in the driving force of the corrosion due to the strong local cathode in promoting  $H_2$  evolution and local corrosion. It is evidenced that the bimodal grain structure is expected to have many grain boundaries that could extend the susceptibility of filiform-like propagation to the exposed area (Yao et al., 2020). The heterogeneity of the microstructure across the welded zone could have influenced the scatter of the OCP values obtained from potentiodynamic polarization measurement.

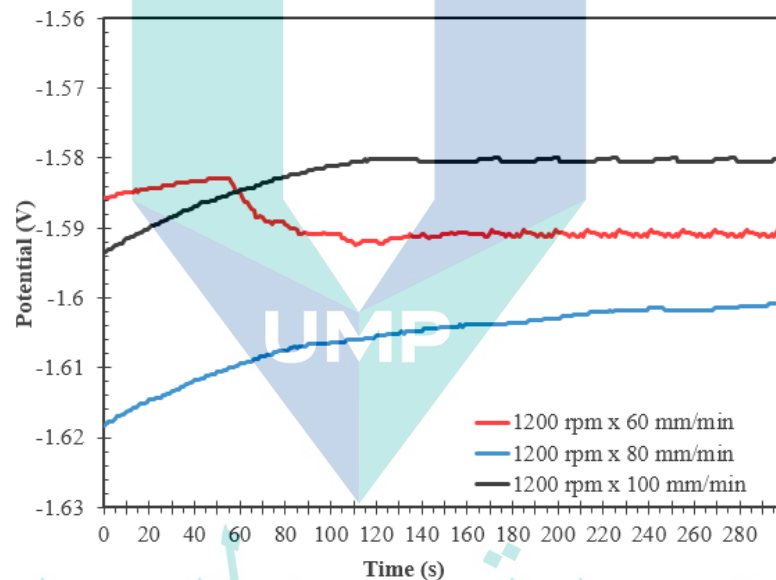


Figure 4.28 Open circuit potential (OCP) vs time curves for 1,200 rpm rotational speed.

#### 4.4.2 Potentiodynamic Polarization

In this experiment, a saturated calomel electrode was used as the reference electrode and a graphite rod was utilized as the counter electrode. The scan rate of 5 mV/s was used for the measurement, with the starting potential at -1.8 V more electronegative than the OCP value.

Figure 4.29 shows the potentiodynamic polarization plot for the rotational speed of 1,200 rpm for welded Mg alloys. All samples indicated no passivity occurrence. Based on the anodic curve of the sample produced at 80 mm/min of feed rate, the anodic

potential started at -1.55 V compared to the feed rates of 100 and 60 mm/min. The sample using the feed rate of 60 mm/min showed that the anodic potential started at a more negative (i.e., active) value at about -1.70 V. From the plot, point (A) shows the balance reaction of cathodic and anodic polarization where free corrosion potential occurs. The visible H<sub>2</sub> gas evolved during potentiodynamic polarization from the corroded electrode surface indicated the initiation of localized corrosion (point B). As the current density and potential increased, the black spots of corrosion product (point B and C) also increased in population and enlarged in size, corresponding to the thick corrosion product formation (point D).

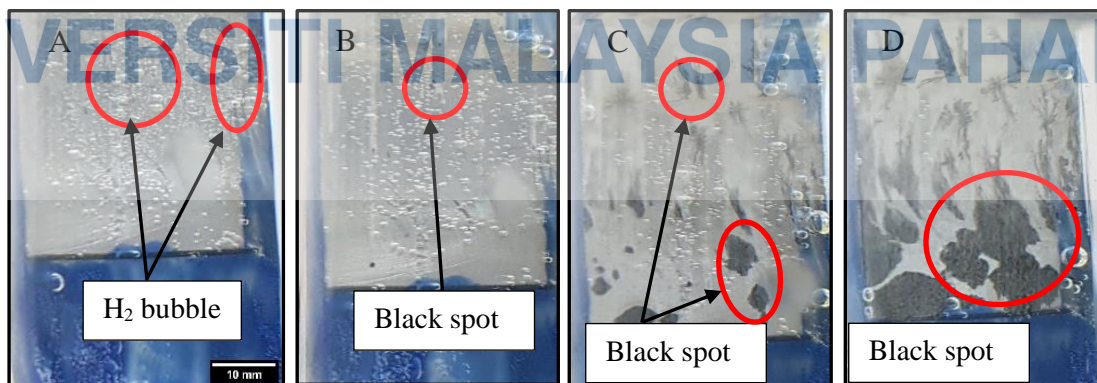
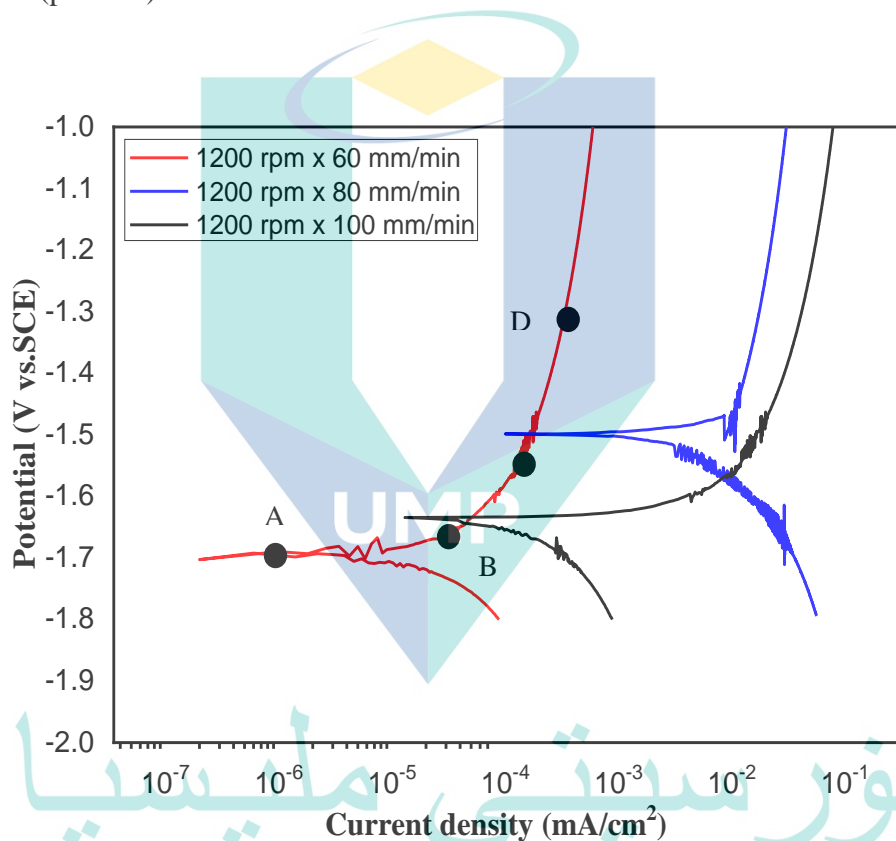


Figure 4.29 Potentiodynamic polarization curve of the welded alloys using 1,200 rotational speed with the surface appearance during anodic polarization.

The sample with the rotational speed of 1,200 rpm and feed rate of 80 mm/min has much higher corrosion potential ( $E_{\text{corr}}$ ) and current density ( $i_{\text{corr}}$ ) compared to the samples produced at the feed rates of 100 and 60 mm/min. Both cathodic and anodic branches shifted to a more electropositive value, about 0.2 V than the sample produced at 60 mm/min and 0.15 V for the sample produced at 100 mm/min.

Figure 4.30 reveals the potentiodynamic polarization for the rotational speed of 1,000 rpm and feed rates of 60, 80, and 100 mm/min. From the curve, all samples indicated no passivity occurrence. The cathodic branch of the sample produced at 1,000 rpm and 100 mm/min shifted to a more electropositive potential about 500 mV compared to the samples produced at the feed rates of 80 and 60 mm/min. The sample using the feed rate of 80 mm/min has less current density than the samples produced at 100 and 60 mm/min, which corresponds to a low corrosion rate. All the data for corrosion potential and current density are listed in Table 4.2.

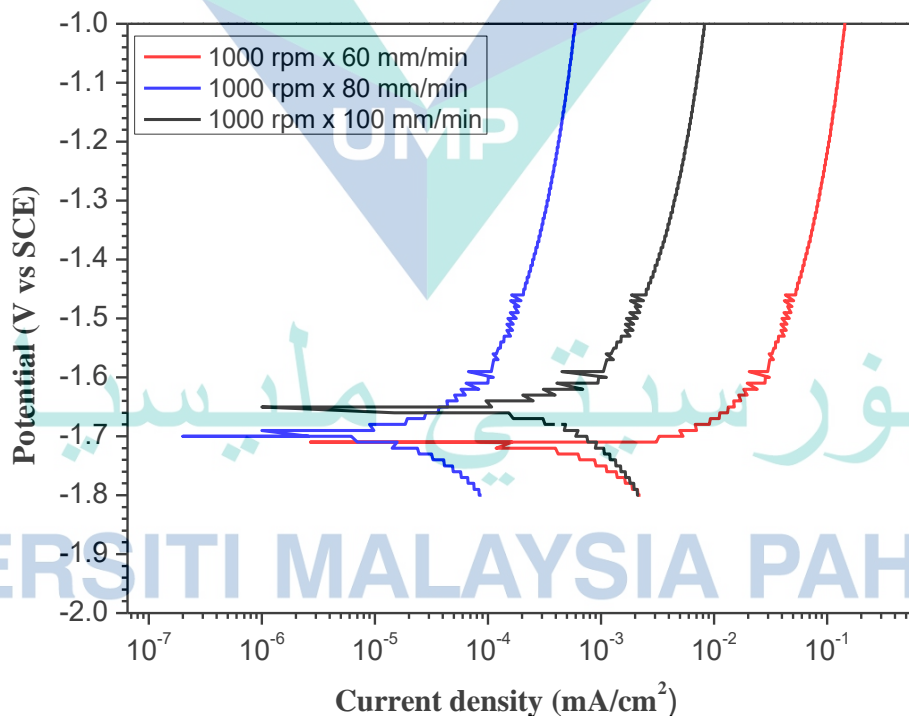


Figure 4.30 Potentiodynamic polarization curve of the welded alloys under 1,000 rpm.

Figure 4.31 shows the potentiodynamic polarization at the rotational speed of 800 rpm and feed rates of 60, 80, and 100 mm/min during the FSW of Mg alloys. From the plot, the sample with the feed rate of 80 mm/min showed a more electropositive corrosion potential of about 0.1 V compared to the samples welded at 100 and 60 mm/min. From the curve, the sample welded at the rotational speed of 800 rpm of and feed rates of 100 and 60 mm/min obtained almost similar value of corrosion potential (i.e., -1.76 V). However, it is observed that the sample produced at 80 mm/min has high current density, which is associated to low corrosion resistance of the sample than both alloys welded at the feed rates of 100 and 60 mm/min.

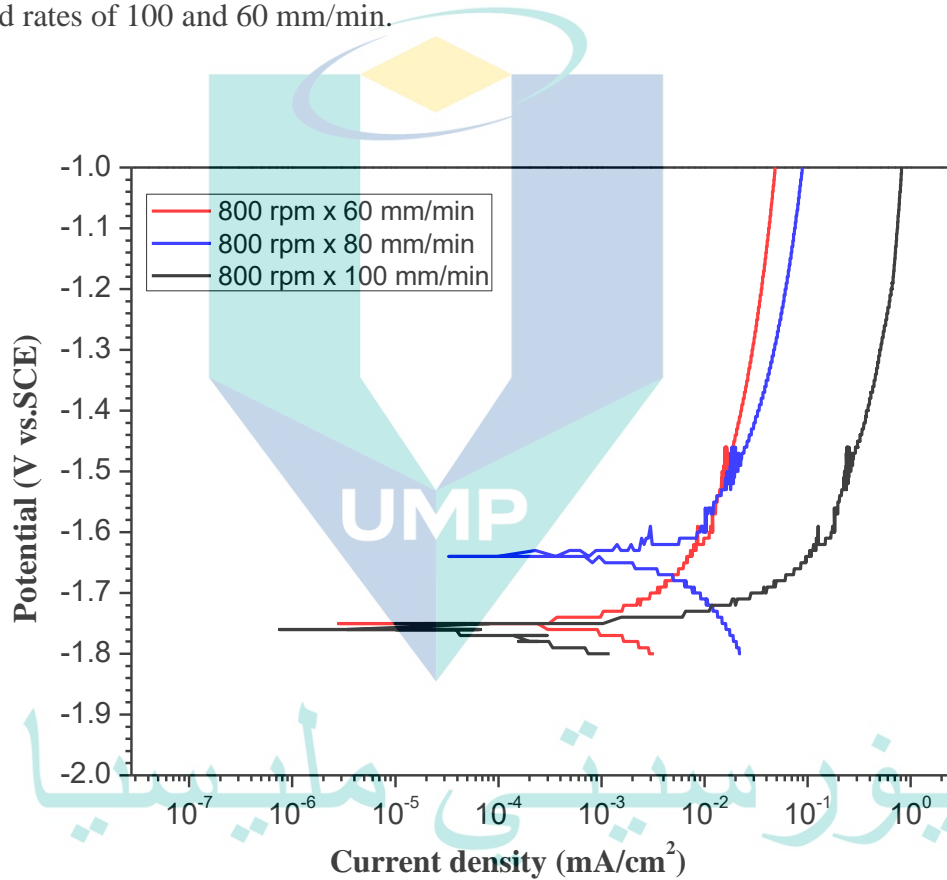


Figure 4.31 Potentiodynamic polarization curve of the welded alloys using rotational speed 800 rpm.

Table 4.2 shows the free corrosion potential ( $E_{\text{corr}}$ ) and current density ( $i_{\text{corr}}$ ) of all welded samples. From the data, it can be seen that the sample subjected to the rotational speed of 1,200 rpm and feed rate of 80 mm/min revealed higher corrosion tendency. The feed rate of 60 mm/min produced a sample with much higher corrosion resistance. The highest corrosion tendency for the feed rate of 80 mm/min can be influenced by the

increase in grain size of the sample. It is suggested that the recrystallization of grain structure improves the corrosion resistance of the samples.

It is also revealed that the rotational speed of 1,000 rpm and feed rate of 80 mm/min produced a sample with the highest corrosion tendency compared to the feed rates of 100 and 60 mm/min. The feed rate of 60 mm/min demonstrated the highest corrosion resistance, which is influenced by the grain structure that recrystallized during welding. From the data, it can be seen that the sample produced at the rotational speed of 800 rpm and feed rate of 100 mm/min has good corrosion resistance. The lowest corrosion potential is produced at the feed rate of 80 mm/min, suggesting the influence of small grains produced by the pinning effect.

Table 4.2 Electrochemical data of welded Mg alloys obtained from potentiodynamic polarization studies in 3.5 wt.% NaCl solution.

Welding condition	Corrosion potential, $E_{corr}$ (V vs. SCE)	Corrosion current density, $I_{corr}$ , mA/cm <sup>2</sup>
1,200 rpm x 100 mm/min	-1.66	$1.63 \times 10^{-4}$
1,200 rpm x 80 mm/min	-1.50	$3.60 \times 10^{-3}$
1,200 rpm x 60 mm/min	-1.70	$1.42 \times 10^{-5}$
1,000 rpm x 100 mm/min	-1.65	$3.21 \times 10^{-4}$
1,000 rpm x 80 mm/min	-1.76	$1.42 \times 10^{-5}$
1,000 rpm x 60 mm/min	-1.78	$9.73 \times 10^{-4}$
800 rpm x 100 mm/min	-1.78	$2.46 \times 10^{-4}$
800 rpm x 80 mm/min	-1.64	$2.26 \times 10^{-3}$
800 rpm x 60 mm/min	-1.75	$1.03 \times 10^{-3}$



## 4.5 Summary

This chapter reveals the result of welded magnesium alloys, microstructure development and corrosion performance. The joining of AZ31/AZ91 was successful under rotational speed of 800, 1,000 and 1,200 rpm and welding speed of 60, 80 and 100 mm/min without any visible defect such as worm hole and lack of bonding defect. The joint consist of the stir zone (SZ), thermomechanical heat affected zone (TMAZ) and heat affected zone (HAZ). Basically all welded sample revealed bimodal recrystallized grains structure of coarse and small grain across the zone from HAZ of AZ31 alloys towards HAZ of AZ91. Dynamic recrystallization take place leads to the grains refinement and simultaneously eliminates  $\beta$ -phase by dissolving it into Mg-matrix. The intermetallic particles found was  $Al_8Mn_5$  conformed by elemental composition analysis. The microhardness obtained by measuring from AZ31 BM to AZ91 BM across the welding zone reveal the hardness value increased. The hardness of the welded area is significantly related to the change of microstructure. Hydrogen evolution test is one of the methods used to determine the corrosion rate of welded Mg alloys. Hydrogen evolution rate revealed that the rotational speed of 1,000 rpm is the most corroded samples followed by 1,200 and 800 rpm. The corrosion rate determine from the weight loss measurement fit with the hydrogen evolution rate. The variation of grain structure are expected to influence the corrosion rate. There are two stages of corrosion attack during hydrogen evolution test known as filiform-like corrosion and accumulation of corrosion product. The welded Mg alloys exhibited open circuit potential (OCP) values in the range of -1.624 to -1.58 V. The potentiodynamic polarization measurement indicated the increase of corrosion rate with the decrease of welding speed from 1,200 to 800 rpm.

## CHAPTER 5

### CONCLUSION AND RECOMMENDATION

#### 5.1 Introduction

This chapter presents the conclusion and recommendation based on the result collected and analyzed throughout the experiment. The corrosion performance of welded Mg alloy has been investigated by correlating the corrosion mechanism with the microstructure development after welding processes. This chapter summarizes the significant outcomes from the research work.

#### 5.2 Microstructure Development of FSW Mg Alloys

The microstructure of AZ31 consisted of coarse grains, intermetallic particles and AZ91 base metal consisted of coarse grains, heavily twins and sub-grains attributed by high amount of deformation and annealing process. Based on the result, the friction stir welding process formed fully recrystallized grains under rotational speed of 1,000 rpm and absence of twin in SZ with mean grain size of 10  $\mu\text{m}$ . TMAZ formed recrystallized grain structure with mean grain size of 20  $\mu\text{m}$  on the AS, while RS formed unclear grains after etching process. The HAZ region reveal grain growth with mean grain size of 40  $\mu\text{m}$ . The increasing of tool rotational speed from 800 to 1,000 and 1,200 rpm, indicated no significant changes on grains size.

The rolled AZ31 and AZ91 Mg alloy also consisted  $\text{Al}_8\text{Mn}_5$  particles as dominant intermetallic particles and absence of  $\beta\text{-Mg}_{17}\text{Al}_{12}$ . The friction stir welding process had little impact on the population density of  $\text{Al}_8\text{Mn}_5$  particles. The friction stir welded alloys reveal bimodal and recrystallized grain structure at the stir zone and thermo-mechanically heat affected zone, whereas the heat affected zone showed grain growth. All samples showed relatively similar trends increasing hardness value from AZ31 BM to AZ91 BM across the welding zone. This trend indicated different grain size due to the different rotational speed and feed rate.

### 5.3 Corrosion Performance of Welded Mg Alloy

The corrosion of welded Mg alloy in chloride solution involves Mg dissolution with the production of  $Mg(OH)_2$  and hydrogen gas evolution. The corrosion started at the anodic point as a pitting corrosion, influenced by the surface condition of the imperfection of surface finish. The corrosion propagated on the surface and formed filiform-like corrosion. A filiform-like corrosion formed in all welded samples following the welding direction with the filament propagation resembling the grain. The whitish and thick corrosion product formed partially protected the alloy by showing reduction of hydrogen gas after longer immersion time.

The presence of intermetallic particles of  $Al_8Mn_5$  reduce the corrosion driven causing the welded alloy exhibited higher corrosion resistance. The less micro galvanic influence due to the relatively low or absence of  $\beta$ - $Mg_{17}Al_{12}$  reduces the corrosion driven in this alloy. The bimodal grain structure of the alloy led to filiform-like corrosion propagated following the pin rotational direction.

### 5.4 Electrochemical Characteristic of Welded Mg Alloy

The Mg alloys welded under rotational speed of 1,000 rpm exhibited the most stable potential of -1.61 V to -1.58 V throughout the OCP measurement compared to the 1,200 rpm and 800 rpm. The presence of  $Al_8Mn_5$  second phase particles in the welded alloys reduced the corrosion driven for intense corrosion attack leading to a stable corrosion potential.

The polarization measurement of welded Mg alloys was correlated to the corrosion development by growth of thick corrosion product or black spot appearance. The increase in anodic potential led to the growth of corrosion product and hydrogen gas evolved at the surrounding of the black spot. The potential and current density were increased during the anodic polarization with the increasing population densities of corrosion product in the form of black spot. The increasing potential during polarization indicated the growth or enlargement of the black spot corresponding to the hydrogen gas evolved at the black dot. The potentiodynamic polarization curve indicated the increase of corrosion rate with the decrease of welding speed from 1,200 to 800 rpm, evidenced by the current density,  $i_{corr}$  value.

## 5.5 Recommendation for Future Work

In order to obtain more accurate results for this study, a better understanding on the welding process and corrosion testing method is required. Preparation for experimental works is important as it can affect the results obtained at the end of the research. Each procedure should be done carefully in order to each more effective research study.

- i. The study on temperature distribution at the SZ, HAZ and TMAZ during welding process can be study in order to correlate with the microstructure changes when rapid cooling take place.
- ii. Mg is the main samples in this research, preparation of the samples should be carried out in consistent way. It is suggested to study surface treatment such as coating on the Mg substrate for better corrosion performance.
- iii. Dynamic recrystallization (DRX) is commonly observed during elevated temperature deformation of Mg and its alloys. It is suggested to study texture characterization using EBSD in order to investigate texture observation caused by DRX.
- iv. To use TEM to observe/study the role of twinning and second phase particle on the corrosion behavior.
- v. To study on different welding parameter effect on the microstructure and corrosion performance

اوپنیورسیتی ملیسیا قهغ

UNIVERSITI MALAYSIA PAHANG

## REFERENCES

- Adamowski, J., & Szkodo, M. (2007). Friction Stir Welds (FSW) of aluminium alloy AW6082-T6. *Journal of Achievements in Materials and Manufacturing Engineering*, 20(1–2), 403–406.
- Afrin, Chen, Cao, & Jahazi, M. (2007). Strain hardening behavior of a friction stir welded magnesium alloy. *Scripta Materialia*, 57(11), 1004–1007. <https://doi.org/10.1016/j.scriptamat.2007.08.001>
- ASTM B90/B90M-13. (2013). *Standard Specification for Magnesium-Alloy Sheet and Plate*.
- ASTM G1-90. (2003). ASTM G1 Standard Practice for Preparing, Cleaning, and Evaluation Corrosion Test Specimens. *Astm*, 8. <https://doi.org/10.1520/G0001-03>
- Atrens, Song, Cao, Shi, Z., & Bowen, P. K. (2013). Advances in Mg corrosion and research suggestions. *Journal of Magnesium and Alloys*, 1(3), 177–200. <https://doi.org/10.1016/j.jma.2013.09.003>
- Bailey, S. J., & Baldini, N. C. (2008a). *Annual Book Of ASTM Standard 2008* (Section 3). ASTM International.
- Bailey, S. J., & Baldini, N. C. (Eds.). (2008b). *ASTM G31-72: Standard Guide for Laboratory Immersion Corrosion Testing of Metals*.
- Bender, S., Goellner, J., Heyn, A., & Boese, E. (2007). Corrosion and corrosion testing of magnesium alloys. *Materials and Corrosion*, 58(12), 977–982. <https://doi.org/10.1002/maco.200704091>
- Blawert, C., Hort, N., & Kainer, K. U. (2004). Automotive applications of magnesium and its alloys. *Trans. Indian Inst. Met*, 57(4), 397-408.
- Cao, Song, & Atrens. (2016). Corrosion and passivation of magnesium alloys. *Corrosion Science*, 111, 835–845. <https://doi.org/10.1016/j.corsci.2016.05.041>
- Cao, X., Jahazi, M., Immarigeon, J. P., & Wallace, W. (2006). A review of laser welding techniques for magnesium alloys. *Journal of Materials Processing Technology*, 171(2), 188–204. <https://doi.org/10.1016/j.jmatprotec.2005.06.068>
- Chen, Fujii, Sun, Morisada, Y., Kondoh, K., & Hashimoto, K. (2012). Effect of grain size on the microstructure and mechanical properties of friction stir welded non-combustive magnesium alloys. *Materials Science and Engineering A*, 549, 176–184. <https://doi.org/10.1016/j.msea.2012.04.030>
- Cottam, Robson, Lorimer, & Davis. (2008). Dynamic recrystallization of Mg and Mg-Y alloys: Crystallographic texture development. *Materials Science and Engineering A*, 485(1–2), 375–382. <https://doi.org/10.1016/j.msea.2007.08.016>

- Cui, Liu, Hu, Shao, J., Li, X., Du, C., & Jiang, B. (2018). The corrosion behavior of AZ91D magnesium alloy in simulated haze aqueous solution. *Materials*, *11*(6), 1–18. <https://doi.org/10.3390/ma11060970>
- Cui, Z. Y., Li, X. G., Xiao, K., Dong, C. F., Liu, Z. Y., & Wang, L. W. (2014). *Pitting corrosion behaviour of AZ31 magnesium in tropical marine atmosphere*. 2782. <https://doi.org/10.1179/1743278213Y.0000000147>
- Dejia, Renlong, Longzhi, Yong, & Jian. (2017). Evaluation of corrosion and wear resistance of friction stir welded ZK60 alloy. *Science and Technology of Welding and Joining*, *22*(7), 601–609. <https://doi.org/10.1080/13621718.2017.1286443>
- Dhanapal, A., Rajendra Boopathy, S., & Balasubramanian, V. (2012). Corrosion behaviour of friction stir welded AZ61A magnesium alloy welds immersed in NaCl solutions. *Transactions of Nonferrous Metals Society of China (English Edition)*, *22*(4), 793–802. [https://doi.org/10.1016/S1003-6326\(11\)61247-8](https://doi.org/10.1016/S1003-6326(11)61247-8)
- Esmaily, M., Mortazavi, N., Osikowicz, W., Hindsefelt, H., Svensson, J. E., Halvarsson, M., Thompson, G. E., & Johansson, L. G. (2016). Corrosion behaviour of friction stir-welded AA6005-T6 using a bobbin tool. *Corrosion Science*, *111*, 98–109. <https://doi.org/10.1016/j.corsci.2016.04.046>
- Gandel, Birbilis, Easton, & Gibson. (2011). The influence of Mn on the corrosion of Al-free Mg-alloys. *18th International Corrosion Congress 2011*, *2*, 1009–1017.
- Gao, J., Cui, X., Liu, C., & Shen, Y. (2017). Application and exploration of friction stir welding/processing in plastics industry. *Materials Science and Technology (United Kingdom)*, *33*(10), 1145–1158. <https://doi.org/10.1080/02670836.2016.1276251>
- Ghali, E., Dietzel, W., & Kainer, K. U. (2013). General and localized corrosion of magnesium alloys: A critical review. *Journal of Materials Engineering and Performance*, *22*(10), 2875–2891. <https://doi.org/10.1007/s11665-013-0730-9>
- Gharavi, F., Matori, K. A., Yunus, R., Othman, N. K., & Fadaeifard, F. (2015). Corrosion behavior of Al6061 alloy weldment produced by friction stir welding process. *Journal of Materials Research and Technology*, *4*(3), 314–322. <https://doi.org/10.1016/j.jmrt.2015.01.007>
- Gui, Li, & Chen. (2019). Effect of heat treatment on corrosion behaviors of Mg-5Y-2Nd-3Sm-0.5Zr alloys. *International Journal of Electrochemical Science*, *14*(2), 1342–1357. <https://doi.org/10.20964/2019.02.25>
- Hazell, P. J., Appleby-Thomas, G. J., Wielewski, E., & Escobedo, J. P. (2014). The shock and spall response of three industrially important hexagonal close-packed metals: magnesium, titanium and zirconium. *Philosophical Transactions of the Royal Society A: Mathematical, Physical and Engineering Sciences*, *372*(2023), 20130204.
- Hu, H., Nie, X., & Ma, Y. (2014). Corrosion and surface treatment of magnesium alloys. *Magnesium Alloys-Properties in Solid and Liquid States; Czerwinski, F., Ed*, 67-108.

- Huang, Wang, Wang, Yuan, Qiao, Yang, Peng, & Li. (2018). Effects of grain size and texture on stress corrosion cracking of friction stir processed AZ80 magnesium alloy. *Engineering Failure Analysis*, 92(June), 392–404. <https://doi.org/10.1016/j.engfailanal.2018.06.012>
- Jaiganesh, Vignesh, & Vignesh. (2017). Investigation on Micro structural and Mechanical Properties of Friction Stir Welded AZ91E Mg Alloy. *Materials Today: Proceedings*, 4(6), 6704–6711. <https://doi.org/10.1016/j.matpr.2017.06.445>
- James, A., North, T. H., & Thorpe, S. J. (2012). Localized corrosion of friction stir spot welds in magnesium AZ31 alloy. *ECS Transactions*, 41(25), 193.
- Jayaraj, Malarvizhi, & Balasubramanian. (2017). Electrochemical corrosion behaviour of stir zone of friction stir welded dissimilar joints of AA6061 aluminium–AZ31B magnesium alloys. *Transactions of Nonferrous Metals Society of China (English Edition)*, 27(10), 2181–2192. [https://doi.org/10.1016/S1003-6326\(17\)60244-9](https://doi.org/10.1016/S1003-6326(17)60244-9)
- Kumar, D. S., Sasanka, C. T., Ravindra, K., & Suman, K. N. S. (2015). Magnesium and its alloys in automotive applications—a review. *Am. J. Mater. Sci. Technol*, 4(1), 12–30.
- Lehner, C., Reinhart, G., & Schaller, L. (1999). Welding of die-casted magnesium alloys for production. *Journal of Laser Applications*, 11(5), 206. <https://doi.org/10.2351/1.521865>
- Li, Qin, Liu, & Wu, Z. (2017). A review: Effect of friction stir welding on microstructure and mechanical properties of magnesium alloys. *Metals*, 7(12), 524–538.
- Liu, G., Ma, Z., Wei, G., Xu, T., Zhang, X., Yang, Y., Xie, W., & Peng, X. (2019). Microstructure, tensile properties and corrosion behavior of friction stir processed Mg-9Li-1Zn alloy. *Journal of Materials Processing Technology*, 267(November 2018), 393–402. <https://doi.org/10.1016/j.jmatprotec.2018.12.026>
- Liu, Ren, & Liu. (2014). A review of dissimilar welding techniques for magnesium alloys to aluminum alloys. *Materials*, 7(5), 3735–3757. <https://doi.org/10.3390/ma7053735>
- Liu, D., Tang, Y., Shen, M., Hu, Y., & Zhao, L. (2018). Analysis of Weak Zones in Friction Stir Welded Magnesium Alloys from the Viewpoint of Local Texture: A Short Review. *Metals*, 8(11), 970.
- Luna, Arenas, Pereira, & Ávila, J. A. (2018). Mechanical and fatigue strength assessment of friction stir welded plates of magnesium alloy AZ31B. *Soldagem e Inspecao*, 23(1), 52–59. <https://doi.org/10.1590/0104-9224/SI2301.06>
- Luo, A. A., & Sachdev, A. K. (2016). Mechanical Properties and Microstructure of AZ31 Magnesium Alloy Tubes. In *Essential Readings in Magnesium Technology* (pp. 381–387). Springer International Publishing. [https://doi.org/10.1007/978-3-319-48099-2\\_61](https://doi.org/10.1007/978-3-319-48099-2_61)

- Magnesium Alloys Market Size, Share & Trends Analysis Report By Application (Automotive & Transportation, Aerospace & Defense, Electronics), By Region (MEA, North America, APAC), And Segment Forecasts, 2020 - 2027.* (2020). Grand View Research. <https://www.grandviewresearch.com/industry-analysis/magnesium-alloys-market>
- Mansoor, & Ghosh. (2012). Microstructure and tensile behavior of a friction stir processed magnesium alloy. *Acta Materialia*, 60(13–14), 5079–5088. <https://doi.org/10.1016/j.actamat.2012.06.029>
- Mezbahul-Islam, M., Mostafa, A., & Medraj, M. (2014). Essential magnesium alloys binary phase diagrams and their thermochemical data. *Journal of Materials*, 2014.
- Mishra, R. S., & Ma, Z. Y. (2005). Friction stir welding and processing. *Materials Science and Engineering R: Reports*, 50(1–2), 1–78. <https://doi.org/10.1016/j.mser.2005.07.001>
- Mohammadi, J., Behnamian, Y., Mostafaei, A., & Gerlich, A. P. (2015). Tool geometry, rotation and travel speeds effects on the properties of dissimilar magnesium / aluminum friction stir welded lap joints. *Journal Of Materials&Design*, 75, 95–112. <https://doi.org/10.1016/j.matdes.2015.03.017>
- Myśliwiec, & Sliwa. (2018). Friction stir welding of thin sheets of magnesium alloy az31b. *Archives of Metallurgy and Materials*, 63(1), 45–54. <https://doi.org/10.24425/118907>
- Pagar, K. R., & Wable, P. A. D. (2016). *Review Paper : Friction Stir Welding (FSW)*. 6(5), 123–129.
- Pan, Xu, Deng, Ye, J., Jiang, X., Tang, A., & Ran, Y. (2016). Effects of friction stir welding on microstructure and mechanical properties of magnesium alloy Mg-5Al-3Sn. *Materials and Design*, 110, 266–274. <https://doi.org/10.1016/j.matdes.2016.07.146>
- Prasad, Saritha, & Narender. (2016). Mechanical Behaviour of Friction Stir Welding of Magnesium AZ-91 Alloy. *International journal of science, engineering and technology research*, 5(12), 3288–3290.
- Qu, Qing, Gao, Xiong, Shuai, Luan, Gong, & Qing. (2018). Enhanced corrosion resistance of AZ91 magnesium alloy through refinement and homogenization of surface microstructure by friction stir processing. *Corrosion Science*, 138(November 2017), 284–296. <https://doi.org/10.1016/j.corsci.2018.04.028>
- Rai, R., De, A., Bhadeshia, H. K. D. H., & DebRoy, T. (2011). Review: friction stir welding tools. *Science and Technology of Welding and Joining*, 16(4), 325–342. <https://doi.org/10.1179/1362171811Y.0000000023>
- Rouhi, S., Mostafapour, A., & Ashjari, M. (2016). Effects of welding environment on microstructure and mechanical properties of friction stir welded AZ91C magnesium alloy joints. *Science and Technology of Welding and Joining*, 21(1), 25-31.



- Salih, O. S., Neate, N., Ou, H., & Sun, W. (2020). Influence of process parameters on the microstructural evolution and mechanical characterisations of friction stir welded Al-Mg-Si alloy. *Journal of Materials Processing Technology*, 275, 116366.. <https://doi.org/10.1016/j.jmatprotec.2019.116366>
- Savguira, Y., North, T. H., & Thorpe, S. J. (2018). Corrosion mechanisms in dissimilar AZ31/AZ80 friction stir welds. *Journal of the Electrochemical Society*, 165(2), C1–C10. <https://doi.org/10.1149/2.0671802jes>
- Schmutz, P., Guillaumin, V., Lillard, R. S., Lillard, J. A., & Frankel, G. S. (2003). Influence of dichromate ions on corrosion processes on pure magnesium. *Journal of The Electrochemical Society*, 150(4), B99.
- Shahnam, A., Karimzadeh, F., Golozar, M. A., & Hosseini, S. N. (2019). Microstructure Evolution of Ultra-Fine-Grained AZ31 B Magnesium Alloy Produced by Submerged Friction Stir Processing. *Journal of Materials Engineering and Performance*, 28(8), 4593–4601. <https://doi.org/10.1007/s11665-019-04198-6>
- Sharma, R., & Singh, O. P. (2013). *Effect of FSW Process Parameters on Mechanical Properties of Polypropylene : An Experimental Study*. 2(12), 7792–7798.
- Singh, G., Singh, H., & Singh, K. (2016). Friction stir welding of magnesium alloys: A review. *Asian Rev. Mech. Eng*, 5, 5-8.
- Singh, Singh, M., & Das, S. (2015). A comparative corrosion behavior of Mg, AZ31 and AZ91 alloys in 3.5% NaCl solution. *Journal of Magnesium and Alloys*, 3(2), 142–148. <https://doi.org/10.1016/j.jma.2015.02.004>
- Singh, Singh, & Singh. (2018). Review on friction stir welding of magnesium alloys. *Journal of Magnesium and Alloys*, 6(4), 399–416. <https://doi.org/10.1016/j.jma.2018.06.001>
- Song, G., Atrons, A., & Suohn, D. (2014). An Hydrogen Evolution Method for the Estimation of the Corrosion Rate of Magnesium Alloys. *Essential Readings in Magnesium Technology*, 9781118858(January), 565–572. <https://doi.org/10.1002/9781118859803.ch90>
- Song, Shan, & Han. (2017). Pitting corrosion of a Rare Earth Mg alloy GW93. *Journal of Materials Science and Technology*, 33(9), 954–960. <https://doi.org/10.1016/j.jmst.2017.01.014>
- Song, & Xu. (2013). The Surface , Microstructure and Corrosion of Magnesium Alloy AZ31 Sheet. *Electrochimica Acta*, 55(13), 4148–4161. <https://doi.org/10.1016/j.electacta.2010.02.068>
- Standard, A. (2004a). ASTM E112-96: Standard Test Method for Determining Average Grain Size. *Standard Test Methods for Determining Average Grain Size*.
- Standard, A. (2004b). ASTM E3-11: Standard Guide For Preparation of Metallographic Specimens. *Standard Test Methods for Sample Grounding and Polishing*.

- Sunil, B. R., Kumar, G. P., Mounika, A. S. N., Sree, P. N., Pinneswari, P. R., Ambica, I., Babu, R. A., & Amarnadh, P. (2015). Joining of AZ31 and AZ91 Mg alloys by friction stir welding. *Journal of Magnesium and Alloys*, 3(4), 330–334. <https://doi.org/10.1016/j.jma.2015.10.002>
- Taltavull, Torres, Lopez, Rodrigo, P., Otero, E., Atrens, A., & Rams, J. (2014). Corrosion behaviour of laser surface melted magnesium alloy AZ91D. *Materials and Design*, 57, 40–50. <https://doi.org/10.1016/j.matdes.2013.12.069>
- Thomas, Medhekar, Frankel, & Birbilis. (2015). Corrosion mechanism and hydrogen evolution on Mg. *Current Opinion in Solid State and Materials Science*, 19(2), 85–94. <https://doi.org/10.1016/j.cossms.2014.09.005>
- Thomas, W. M., Threadgill, P. L., & Nicholas, E. D. (1999). Feasibility of friction stir welding steel. *Science and Technology of Welding and Joining*, 4(6), 365–372.
- Tuz, L., Kołodziejczak, P., & Kolasa, A. (2013). Friction stir welding of AZ-91 and AM-Lite magnesium alloys. *Welding International*, 27(4), 265–267.
- Verma, Taiwade, Sapate, Patil, & Dhoble. (2017). Evaluation of Microstructure, Mechanical Properties and Corrosion Resistance of Friction Stir-Welded Aluminum and Magnesium Dissimilar Alloys. *Journal of Materials Engineering and Performance*, 26(10), 4738–4747. <https://doi.org/10.1007/s11665-017-2877-2>
- Wang, Deng, Mao, Tong, Y., & Ran, Y. (2017). Influence of tool rotation rates on temperature profiles and mechanical properties of friction stir welded AZ31 magnesium alloy. *International Journal of Advanced Manufacturing Technology*, 88(5–8), 2191–2200. <https://doi.org/10.1007/s00170-016-8918-4>
- Wang, H., Wu, P. D., & Gharghour, M. A. (2010). Effects of basal texture on mechanical behaviour of magnesium alloy AZ31B sheet. *Materials Science and Engineering A*, 527(15), 3588–3594. <https://doi.org/10.1016/j.msea.2010.02.050>
- Wang, Y., Huang, Z., Yan, Q., Liu, C., Liu, P., Zhang, Y., Guo, C., Jiang, G., & Shen, D. (2016). Corrosion behaviors and effects of corrosion products of plasma electrolytic oxidation coated AZ31 magnesium alloy under the salt spray corrosion test. *Applied Surface Science*, 378, 435–442. <https://doi.org/10.1016/j.apsusc.2016.04.011>
- Woo, Choo, Brown, Liaw, P. K., & Feng, Z. (2006). Texture variation and its influence on the tensile behavior of a friction-stir processed magnesium alloy. *Scripta Materialia*, 54(11), 1859–1864. <https://doi.org/10.1016/j.scriptamat.2006.02.019>
- Woo, Choo, Prime, Feng, Z., & Clausen, B. (2008). Microstructure, texture and residual stress in a friction-stir-processed AZ31B magnesium alloy. *Acta Materialia*, 56(8), 1701–1711. <https://doi.org/10.1016/j.actamat.2007.12.020>
- Xie, Ma, & Geng. (2008). Effect of microstructural evolution on mechanical properties of friction stir welded ZK60 alloy. *Materials Science and Engineering A*, 486(1–2), 49–55. <https://doi.org/10.1016/j.msea.2007.08.043>

- Yao, Y., Tang, J., Chen, T., Wang, Z., Yu, H., & Zhou, C. (2020). *Microstructure and Corrosion behavior of Friction Stir-Welded AZ31 alloy*. *15*, 1058–1071. <https://doi.org/10.20964/2020.02.18>
- Yuan, Panigrahi, Su, & Mishra. (2011). Influence of grain size and texture on Hall-Petch relationship for a magnesium alloy. *Scripta Materialia*, *65*(11), 994–997. <https://doi.org/10.1016/j.scriptamat.2011.08.028>
- Zeng, R. C., Chen, J., Dietzel, W., Zettler, R., dos Santos, J. F., Lucia Nascimento, M., & Kainer, K. U. (2009). Corrosion of friction stir welded magnesium alloy AM50. *Corrosion Science*, *51*(8), 1738–1746. <https://doi.org/10.1016/j.corsci.2009.04.031>
- Zeng, Zhang, Huang, Dietzel, Kainer, Blawert, & Ke. (2006). Review of studies on corrosion of magnesium alloys. *Transactions of Nonferrous Metals Society of China (English Edition)*, *16*, 763–771. [https://doi.org/10.1016/S1003-6326\(06\)60297-5](https://doi.org/10.1016/S1003-6326(06)60297-5)
- Zhang, H. (2010). Friction stir welding of magnesium alloys. In *Welding and Joining of Magnesium Alloys* (pp. 274–305). Woodhead Publishing.
- Zhang, Rauch, & Véron. (2013). Twinning analyses in a magnesium alloy with tilting series scanning method using a TEM based orientation mapping system. *Materials Letters*, *111*, 192–196. <https://doi.org/10.1016/j.matlet.2013.08.072>
- Zhao, Zhao, Xu, Liu, Tao, Gao, Shuai, & Atrons. (2019). Formation and characteristic corrosion behavior of alternately lamellar arranged  $\alpha$  and  $\beta$  in as-cast AZ91 Mg alloy. *Journal of Alloys and Compounds*, *770*, 549–558. <https://doi.org/10.1016/j.jallcom.2018.08.103>

اونيورسيٲي ملايسيا قهغ

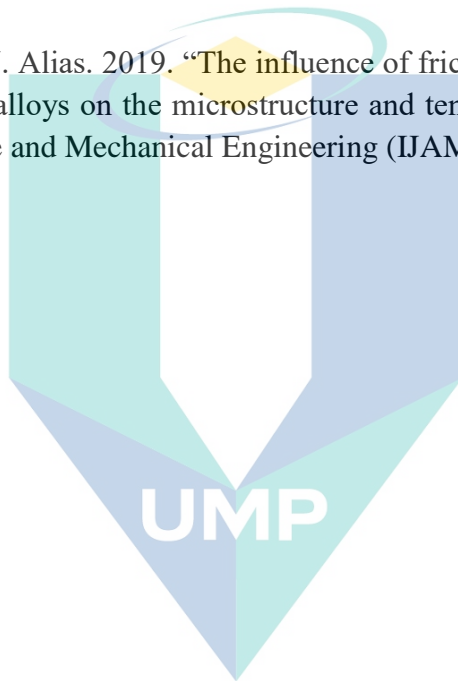
UNIVERSITI MALAYSIA PAHANG

## APPENDIX A PUBLICATIONS

**N. S. Mohamed** and J. Alias. 2017. "A Review on the Effect of Welding on the Corrosion of Mg Alloys." IOP Conference Series: Materials Science and Engineering.

J. Alias and **N. S. Mohamed** and M., Ishak and Zhou, Xiorong and Thompson, George E. 2018. "The influence of hot forming on the microstructure and corrosion behaviour of AZ31B Mg alloys." Indonesian Journal of Science & Technology, 3 (2). pp. 150-157.

**N. S. Mohamed** and J. Alias. 2019. "The influence of friction stir welding of dissimilar AZ31 and AZ91 Mg alloys on the microstructure and tensile properties." International Journal of Automotive and Mechanical Engineering (IJAME), 16 (2). pp. 6675-6683



اونيورسيتي ملايسيا قهغ

UNIVERSITI MALAYSIA PAHANG

## APPENDIX B CORROSION RATE

### Weight loss measurement:

Welding condition ( rpm x mm/min)	Average weight prior experiment (g)	Average weight after cleaning (g)	Average weight loss (g)
1,200 x 60	0.540	0.389	0.151
1,200 x 80	0.532	0.451	0.081
1,200 x 100	0.530	0.44	0.090
1,000 x 60	0.535	0.310	0.225
1,000 x 80	0.500	0.357	0.143
1,000 x 100	0.495	0.355	0.140
800 x 60	0.459	0.354	0.105
800 x 80	0.513	0.370	0.143
800 x 100	0.520	0.425	0.095

### Corrosion rate calculation:

$$\text{Corrosion Rate (CR)} = \frac{K \times W}{A \times T \times D}$$

Where,

$$W = 1.5 \text{ cm}$$

$$L = 2 \text{ cm}$$

$$H = 0.3 \text{ cm}$$

$$A = [2(W \times L) + 2(W \times H) + 2(L \times H)]$$

$$A = [2(1.5 \times 2) + 2(1.5 \times 0.3) + 2(2 \times 0.3)]$$

$$A = 8.1 \text{ cm}^2$$

$$K = 8.76 \times 10^4 \text{ (Constant value)}$$

$$T = 144 \text{ hour}$$

$$D = 1.75 \text{ g/cm}^3$$

Sample 1:

$$\begin{aligned} \text{Corrosion Rate (CR)} &= \frac{K \times W}{A \times T \times D} \\ &= \frac{(8.76 \times 10^4) \times 0.151 \text{g}}{8.1 \text{ cm}^2 \times 144 \text{ hour} \times 1.75 \text{ g/cm}^3} \\ &= 6.45 \text{ mm/yr} \end{aligned}$$